Design, Fabrication, and Spectroscopy of Strain-Tunable Quantum Dots in Nanowire Antennas

Peter Edmund Kremer

A dissertation for the degree of Doctor of Philosophy

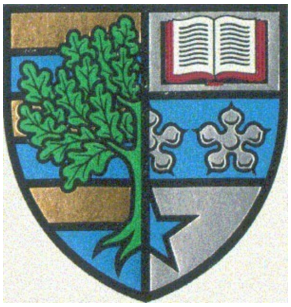

Heriot-Watt University, Edinburgh, United Kingdom
Institute of Photonics and Quantum Sciences, SUPA

July 2015

Abstract

Single-photon sources with high brightness, resolution-limited linewidths, and wavelength tunability are promising for future quantum technologies. This thesis investigates elastically tunable quantum dots (QDs) inside nanowire antennas which are fabricated and studied using photoluminescence spectroscopy and time correlated single photon counting at cryogenic temperature. For the nanofabrication, a new electron beam lithography system and a reactive ion etch chamber have been calibrated and maintained. GaAs nanowires with diameters as low as 120 nm and aspect ratios as high at 1:18 were successfully fabricated. These nanowires were structurally characterized by single electron microscopy. A sample with nanowires containing QDs was vertically bonded to a piezoelectric crystal. To carry out experiments at low temperature, two commercial and one home-built pulsed-tube cryostats were assembled. A miniature confocal microscope, which can be used inside the home built cryostat, was assembled and characterised. A confocal microscope to carry out spectroscopy at telecom wavelength, to be used with the commercial cryostats, was assembled and used in experiments by other group members. A third microscope for near infrared spectroscopy was assembled, to carry out spectroscopic characterization of the strain tunable device. And reveals that the nanowire geometry influences the extraction efficiency (η). For the brightest nanowire, we estimated $\eta \approx 57$ %. We find that non-resonant excitation leads to static (fluctuating) charges, likely at the nanowire surface, causing DC Stark shifts (inhomogeneous broadening); for low excitation powers, the effects are not observed, and resolution-limited linewidths are obtained. Despite significant strain-field relaxation in the high-aspect-ratio nanowires, we achieve up to 1.2 meV tuning of a dot's transition energy.

Table of contents

List of figures

List of tables

List of Publications

1. P.E. Kremer, A.C. Dada, P. Kumar, Y. Ma, S. Kumar, E. Clarke, and B. D. Gerardot. Strain-tunable quantum dot embedded in a nanowire antenna. Phys. Rev. B, 90:201408, Nov 2014.

2. L. Sapienza, R.N.E. Malein, C.E. Kuklewicz, P.E. Kremer, K. Srinivasan, A. Griffiths, E. Clarke, M. Gong, R.J. Warburton, and Brian D Gerardot. Exciton fine-structure splitting of telecom-wavelength single quantum dots: Statistics and external strain tuning. Physical Review B, 88(15):155330, 2013.

3. Y. Ma, P.E. Kremer, and B.D. Gerardot. Efficient photon extraction from a quantum dot in a broad-band planar cavity antenna. Journal of Applied Physics, 115(2):023106, 2014.

4. D. Wen, F. Yue, S. Kumar, Y. Ma, M. Chen, X. Ren, P. E. Kremer, B. D. Gerardot, M. R. Taghizadeh, G.S. Buller, and X. Chen. Metasurface for characterization of the polarization state of light. Optics Express, 23(8):10272, 2015.

5. P.E. Kremer. Top-Down Fabrication of GaAs Nanowire Antennas with Embedded Quantum Dots. Presentation at 2014 MRS Spring Meeting.

6. P.E. Kremer. Top-Down Fabricarion and Spectroscopy of GaAs Nanowires embedded with Quantum Dots . UK Semiconductors 2012 Conference, Poster. 2012.

Chapter 1

Introduction

In the past century, the invention of the semiconductor transistor has lead to the development of computers that have hugely increased the quality of life and are essential in developing new technologies. Their miniaturization is reaching a limit. On the small scale these computers have reached the limit of classical physics and the rules of quantum physics have to be applied to engineer smaller, faster, more cost and energy efficient devices. Some calculations performed on classical computers, even though scaled up to large clusters would not be able to be "finished in the lifetime of the Universe" [1].

A solution would be to use quantum computing, where the states 0 and 1 can exist at the same time [2]. This would make some calculations exponentially faster with increasing memory. Examples are Shor's algorithm [3] which can factor large numbers faster than standard computers and would allow quantum computers to decrypt information encrypted using factorization. While Lov Grover worked out an algorithm that can search large databases faster [4].

These algorithms can be used in linear optical quantum computing where single photons are used as information carriers. Single photons as information carriers are also essential for quantum repeaters and distributed quantum networks [5, 6], where fiber optics or free space is used to transmit information over large distances. The latter requires a reliable source of on demand indistinguishable single photons. Other technologies where single photons are required are in metrology.

The generation of single photons was first achieved using an attenuated laser, but these can never be on-demand single photon sources due to Poisson statistics of coherent states. A more sophisticated source would be a single atom that due to the Pauli exclusion principle can only emit one photon at a time. This principle is exploited using ion traps. Molecules and nitrogen vacancies in diamond have also been shown to emit single photons.

A more promising source is to use artificial atoms, especially self-assembled III-V semiconductor quantum dots (QDs). QDs can be incorporated into existing semiconductor manufacturing processes, and have promising properties such as narrow transform limited linewidth and single photon emission [7–9].

1.1 Thesis outline

Chapter 1 section 1.2 introduces the properties of QDs and the quantum confinement of excitons and the QD's atomlike energy levels as well as their growth. Furthermore, the effect of strain and electric fields on the QD's energy levels and their corresponding change in optical emission properties are discussed. Section 1.2.4 discusses the requirements of a indistinguishable single photon source used for QIP applications and metrology which are; (i) efficient collection of the spontaneous emission into a single optical mode, (ii) minimal inhomogeneous broadening to enable transform limited linewidths and (iii) spectral tunability so that each dot can be made indistinguishable [10, 11]. Section (1.3) outlines different light matter enhancement strategies and shows why a strain-tunable photonic nanowire is most suitable for the efficient collection of photons from a QD embedded in a device designed for spectral tunability .

Chapter 2 outlines the fabrication schematics of a strain tunable photonic nanowire with an embedded QD and gives an insight into the nanofabrication techniques used. The techniques used are: electron beam writing, electron beam metal deposition, thermocompression bonding and wet and dry etching of GaAs and related alloys.

Chapter 3 explains the methods used for low temperature optical spectroscopy of the fabricated device which include: assembly of pulsed tube cryostats, assembly and alignment of confocal microscopes and characteristics of a optical spectrometer and a Hanburry Brown-Twiss interferometer used for time correlated single photon counting.

Chapter 4 summarizes the results of the optical characterization of the QD embedded in nanowires. The extraction efficiency of individual nanowires is related to the nanowire geometry determined by scanning electron microscopy. The experimental extraction efficiency results are supported by computer simulations. The influence of inhomogeneous linewidth broadening of the QD emission, due to charges on the nanowire surface, and Stark shift as a function of excitation power are measured and discussed as well. Lifetime measurements of the QD are carried out and the single photon nature of the device is investigated. Finally the effect of strain on the nanowire and the resulting QD spectral tunability are simulated, experimentally measured and discussed.

Chapter 5 comprises of concluding remarks, instructions for improvement of the fabricated device and suggestions for future work in an outlook section.

1.2 Quantum dots

The name quantum dot generally refers to semiconductor quantum dots. QDs are portions of semiconductor material that are constructed of a low band gap semiconductor material enclosed by a higher band-gap material in a size range which is comparable to the de-Broglie wavelength of the electron [12]. This leads to carrier confinement in all spatial directions. The confined electron and hole states are quantized, similar to electrons in an atom. Quantum dots are therefore referred to as artificial atoms. Semiconductor quantum

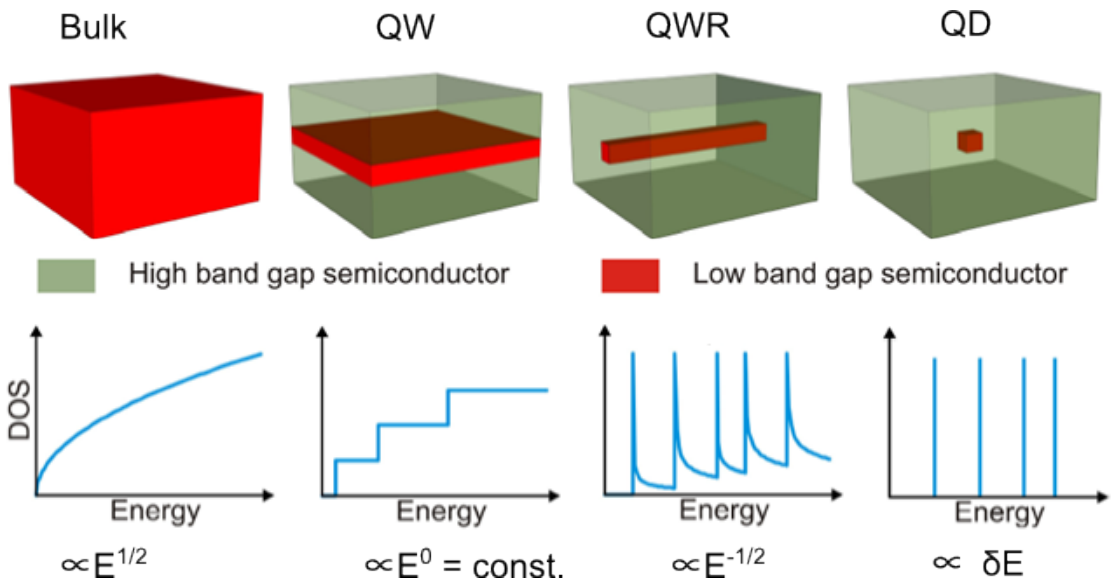

Fig. 1.1 Sketches of bulk material, Quantum well, Quantum wire and quantum dot with their respective qualitative plots of the density of states [13]. By confining the particles further in 1D (quantum wire) and 0D (quantum dot), the zero dimensional confinement leads to a density of states (DOS) comprising of discrete Lorentzian peaks as observed in atoms.

dots can be further embedded in heterostructures and devices with additional control of the QD charge state or energy.

QDs are used to study quantum physics by providing a system to trap and manipulate quantum states such as spins, excitons and photons. Due to their high quantum efficiencies, large dipole moments and a variety of quantum states that can be optically controlled, InAs quantum dots are well suited for quantum photonic applications [12].

1.2.1 Quantum confinement and exciton states

Single atoms have discrete energy levels, whereas bulk semiconductors have energy bands as a result of the interaction and atom overlap in the semiconductor matrix. The density of states (DOS), g(E), is the number of energy states within a small energy scale. In bulk semiconductors the DOS is proportional to the square root of the energy $\sqrt{E}$ and the effective mass of the carriers m_{eff} (see Fig.1.1).

$$g_{3D}(E) = m_{eff}\sqrt{(2m_{eff}E)/\pi^2\hbar^3} \tag{1.1}$$

A heterostructure comprising a low bandgap material embedded in a high bandgap material, is a two dimensional (2D) semiconductor heterostructure and is referred to as a quantum well (QW) (see Fig.1.1 QW). In this case a quantum mechanical particle can be confined in the region of the low bandgap material. If the low band gap material has a similar physical size as the particle's de Broglie wavelength $\lambda_{Broglie} = h/p$ (where p is the momentum of the particle and h Planck's constant), in at least one dimension, the confinement leads to a quantization in this direction. This is the situation for a QW, where

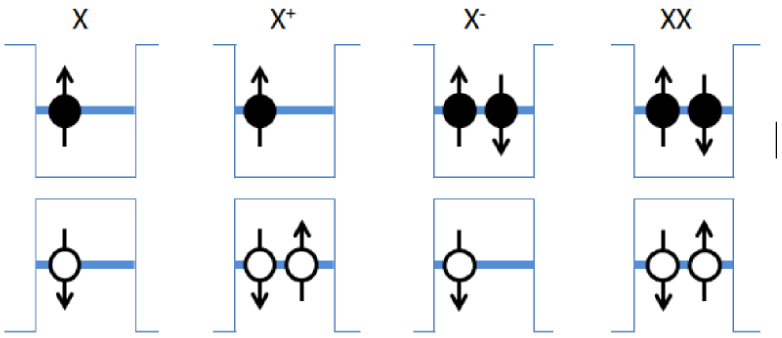

Fig. 1.2 Sketch of different exciton charge states, neutral exciton X^0 electron hole pair, positive charged exciton X^+ two holes one electron, negative charged exciton X^- two electron one hole, biexciton XX two electron hole pairs.

the other directions are not quantized and the particles can move freely as in the bulk material. The DOS is described by step functions

$$g_{2D}(E) = N * m_{eff}/\pi\hbar^2 \tag{1.2}$$

with N the number of the QW subband. Similarly particles can be confined in one dimensional (1D) structure called a quantum wire (QWR)(see Fig.1.1 QWR), Where the DOS is proportional to $E^{-1/2}$.

$$g_{1D}(E) = 2\sqrt{m_{eff}/E} \tag{1.3}$$

Zero dimensional (0D) confinement is achieved in a quantum dot (QD). The zero dimensional confinement leads to a DOS comprising of discrete Lorentzian peaks as observed in atoms (see Fig.1.1 QD). Here the DOS is simply defined by a delta function where the factor of 2 represtents the number of electrons that can occupy the states.

$$g_{0D}(E) = 2\delta E \tag{1.4}$$

QDs are typically made of tens of thousands of atoms and their Lorentzian peaks have been shown to have a FWHM of ~ 0.33 μeV and are transform limited at 4 K.

In a semiconductor typically a Wannier-Mott exciton X^0 is formed when an electron from the conduction band (CB) and a hole from the valence band (VB) are bound together. This is due to the large dielectric constant which results in a screening effect and a reduced Coulomb interaction between the electron and the hole [14].

The exciton is a neutral quasi-particle. Due to the confinement of the carriers in all directions, various exciton complexes such as the biexciton XX and positive and negative charged excitons (denoted by X^{1+} and X^{1-} respectively) can be formed (see Fig.1.2).

Due to the zero dimensional confinement of electrons in a QD there are quantized energy levels similar to a particle in a box. M.Bayer *et al.* observed that the electrons and holes occupy the confined electronic shells in characteristic numbers according to the Pauli exclusion principle [15]. Therefore, atomic physics nomenclature is used to describe

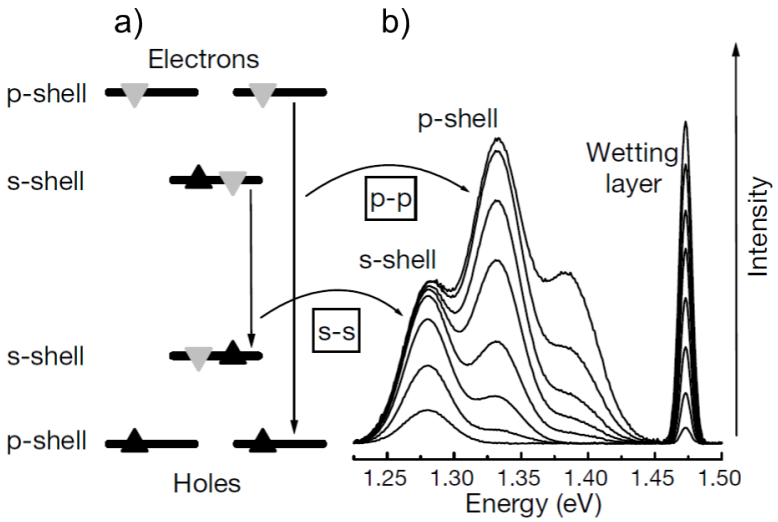

Fig. 1.3 *a*) Filled shells with spin up/down electrons and holes. *b*) A corresponding spectra of the QD emission taken with different excitation powers. Data taken from [15].

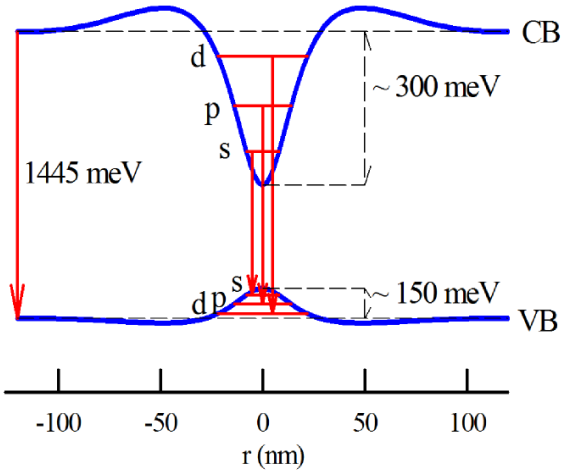

Fig. 1.4 Parabolic confinement potential with conduction band (CB) and valence band (VB). Shown are s, p and d shells.

the ground and exited states. The ground state is referred to as the s-state and the excited state is p like.

As can be seen in the spectrum of the ensemble emission of QDs (see Fig.1.3), when the QD are optically excited, first the s shell saturates then the p shell. The s shell is two-fold spin-degenerate and can only be occupied by up to two excitons. Due to the disc shaped geometry of the dots the p-state is four fold degenerate and not sixfold as in conventional atoms. Experiments with charge tunable dots have been carried out to demonstrate this [16].

For the InGaAs QDs studied in this thesis the shape of the confinement potential can be approximated by a two-dimensional harmonic oscillator and a parabolic shape (see Fig.1.4).

The exchange interaction is a quantum mechanical energy (in addition to the Coloumb energy) between identical particles [17]. In a single semiconductor quantum dot the exchange interaction results in the exciton eigenstates XX and X being linearly polarized

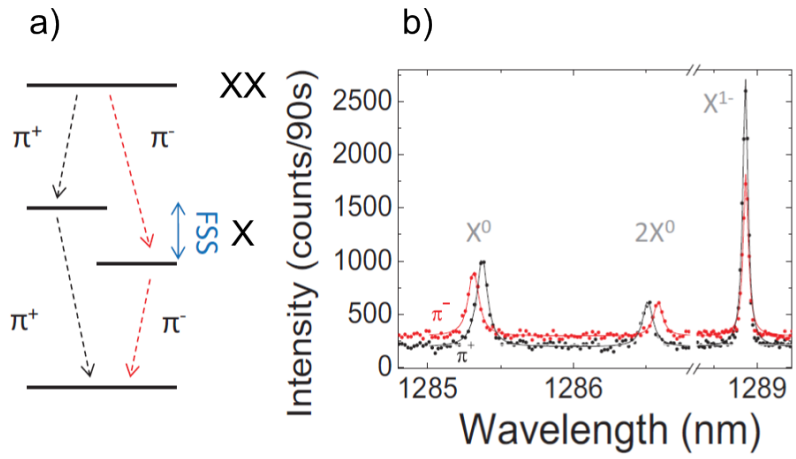

Fig. 1.5 *a*) Schematic of the biexciton XX to exciton X^0 to vacuum state transitions and their respective polarizations (π^+ or π^-). *b*) Example of PL spectra at orthogonal polarizations, showing the X^0, XX, and singly charged exciton (X^{-1}) emission lines (full symbols) and a Lorenzian fit to the data (solid lines). Data taken from [20].

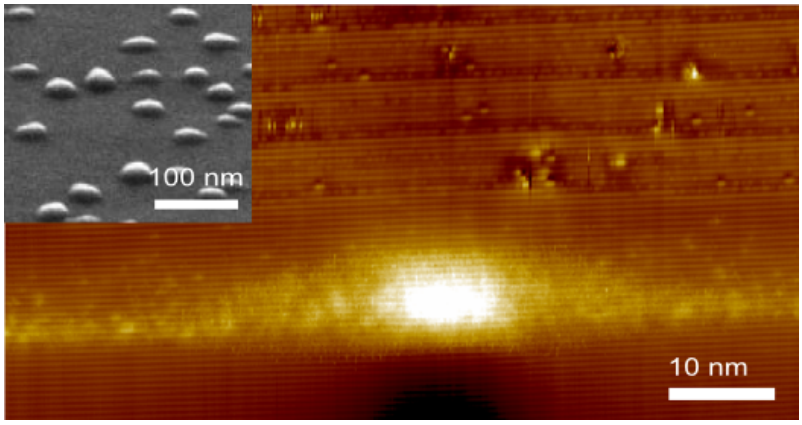

Fig. 1.6 X-TEM cross section of a QD with a diameter of 20 nm and height 5 nm over grown by GaAs (by P. Koenraad). Bright lens- shape atoms are InAs on top of a wetting layer stretching from the left to the right of the image. Inset: SEM image of QD ensemble (un-capped) on a growth substrate(C.Schneider [12]).

with an energy difference represented by the fine structure splitting (FSS) [18, 19]. The magnitude of the FSS is influenced by the structural asymmetry (shape) in the QD and strain. The FSS can be influenced as well by the dot size and composition. Due to the FSS the two photons in the biexciton cascade that are orthogonally polarized are distinguishable by their energy (see Fig.1.5).

When the FSS is smaller than the linewidth, the biexciton-exciton-cascade can lead to the emission of polarisation-entangled photon-pairs [19, 21, 22]. The opposite polarization of the photons is due to the nature of opposite spins of the electrons in the biexciton state.

1.2.2 Quantum dot growth

There are two main ways to manufacture self-assembled semiconductor QDs: colloidal quantum dots that are manufactured in solution using wet chemistry, and self-assembly using the Stranski-Krastanov (SK) method. The QDs used in this thesis were InGaAs QDs grown by the SK method. QDs are typically 10 - 20 nm in diameter and 3 - 5 nm in height (see Fig.1.6). In the SK method InAs is grown epitaxial on GaAs.

Due to a lattice mismatch of about 7% the InAs layer reduces its strain by forming islands after 1-2 monolayers (0.4 nm) [23–25]. Prior to the island formation a thin layer of material forms across the growth substrate called the wetting layer which acts like a disordered quantum well with a broad DOS [26].

The QDs are capped with a layer of GaAs 80-110 nm (minimum) to prevent carrier ionization and electric fields caused by trapped charges on the surface. Capped dots also do not show photoblinking or photo-bleaching.

InAs/GaAs dots are 100% quantum efficient optical emitters at $\approx 1.13\ \mu$m. At this wavelength a Si charge-coupled-device (CCD) has a low quantum efficiency.

A subsequent annealing step converts the QD shape to truncated pyramids or flattened lenses [12]. During annealing, thermal intermixing of the QD and GaAs matrix result in a shorter emission wavelength, which shifts from 1200 nm to 950 nm [27, 28]. At this wavelength the Si CCD, used for optical characterization of the QD, has a better quantum efficiency.

The material quantity and composition determines the QD density which is around 10^{10} dots/cm^2 for the InAs QDs used in this thesis. The size of the islands fluctuates by 10% within a sample [25] and gives rise to a variation in confinement energies. The SK method using InGaAs produces dots of high quality compared to other materials such as InP.

1.2.3 Tuning exciton emission energies using strain and quantum confined Stark effect

For applications in quantum information processing, sources of indistinguishable photons are required. Due to the unique nature of each quantum dot this represents a huge obstacle [29]. Therefore spectral tunability to create indistinguishable photons from QDs is highly desirable. Another promising application of QD's is to exploit the biexciton-exciton-ground state cascade to create entangled photons by reducing the natural occurring FFS [20, 30, 31]. Other than changing the growth conditions there are reversible and irreversible tuning techniques to tune the QD emission properties. An irreversible technique is rapid thermal annealing (RTA) [32]. Reversible techniques are the application of magnetic fields [33], electric fields [10, 34–37], temperature changes [38] and strain [30, 31].

Temperature change and magnetic fields provide changes to the QD emission energy. The red-shift in magnetic fields occurs due to the diamagnetic-shift [13], but applying

magnetic fields requires a very bulky set-up. A red shift in emission occurs due to the decrease in band gap of the QD as the temperature increases. The disadvantage of this method is that at higher temperatures the linewidth of the emission becomes broader and the emission intensity reduces [39].

A less bulky setup is needed for emission tuning using an electric field. A dipole in an electric field displays a Stark shift with quadratic field dependence: $E = E_0 - pF + \beta F^2$ where E is the energy, F the electric field, p the permanent dipole moment, and β the polarizability. Fig.1.7 a) shows the shift in emission wavelenght as a function of applied electric field from Kowalik *et al.* [40]. Gerardot *et al.* estimated that an electric field $F = 15kV/cm$ is needed for a 1 meV Stark shift using β = -4 μeV [36]. Applying electric fields in the growth direction shown by Bennett *et al.* resulted in tuning of > 25 meV [19]. The FSS of the QD's was reduced as low as 1.5 μeV. Which is below the threshold required to create entangled photon pairs through the XX cascade, however the electric field also increases the nonradiative carrier tunneling probability and decreases the oscillator strength [36] which is observed as a reduced exciton emission intensity [36]. Furthermore, electric field fluctuations increase the linewidth [36].

The emission of QD's can also be tuned using strain. For the case of crystalline materials, the strain can be defined as the fractional change in lattice constant. If a_0 and a_ε are the substrate lattice constant and the strained layer lattice constant respectively, then the lattice mismatch in-plane strain is denoted as ε and can be given by

$$\varepsilon = \frac{a_\varepsilon - a_0}{a_0} \tag{1.5}$$

Strain affects the bandgap E_g and bandshape [41]. The bandgap is reduced for biaxial tensile strain and is increased for biaxial compressive strain in zinc-blende-type crystals [13, 42]. Uniaxial strain applied using a lead-zirconate-titanate (PZT) piezoelectric actuator glued to a GaAs membrane with embeded QD's has been used by Seidl *et al.* to tune the QD emission wavelength by up to 0.5 meV and decreased the FSS by 6.9 μeV [30]. This is caused by tuning the symmetry of the QD confining potential. Reducing the FSS by up to 50% from 46.4 μeV to 22.5 μeV and energy detuning ΔE = 0.99 meV using uniaxial strain has been shown for telecom wavelength quantum dots by L.Sapienza *et al.*[20].

Using a PMN-PT ($[Pb(Mg_{1/3}Nb_{2/3})]0.72[PbTiO_3]_{0.28}$) instead of PZT higher strain and therefore a higher tunability can be achieved. F. Ding *et al.* was able to tune the emission wavelength of a QD using biaxial strain by up to 11 meV [43], but the bi-axial strain did not alter the FSS. A color coincidence of the X and XX emission line was achieved at maximum strain applied to a QD (see Fig.1.7 b). R.Trotta *et al.*, using a PMN-PT and a thinner GaAs membrane achieved tuning ranges of up to 10 meV and simultaneous use of electric fields showed that it is always possible to drive the excitons confined in an arbitrary QD towards universal level crossing. The observation of the behavior of all the quantum dots measured suggests the existence of a universal behavior

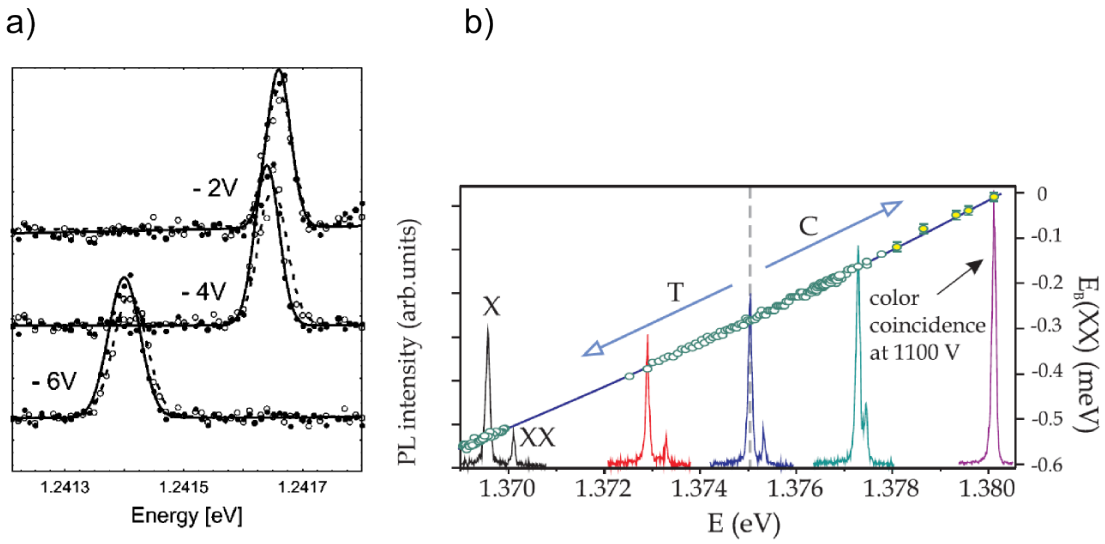

Fig. 1.7 *a*) Stark shift in emission due to applied electric field data taken from [40]. *b*)Blue and red shift in peak emission due to applied tensile and compressive strain respectively, showing the decrease between X and XX as a function of X, data taken from [43].

of the FSS under the influence of strain and electric fields [29].

1.2.4 Quantum dots as single photon sources

For QIP applications and metrology, fast and efficient single-photon sources are required. The fastest triggered single photon sources to date have been demonstrated using epitaxial grown semiconductor QDs [44]. The first report about an epitaxially grown QD used as a single photon source was published in 2000 by P. Michler *et al.* [45]. QDs in nanowires have also shown to emit single photons with GHz rates at room temperature [46]. For a QD to emit photons it has to be optically or electrically excited. In the case of optical excitation, a laser pulse containing many photons is converted into a stream of single photons.

A QD can be modeled as a two level system |g> and |e>. If the system is in the excited state spontaneous emission of a photon from |e> to |g> occurs. After decay, the system cannot emit another photon until it is excited again. This capability to emit only one time separated single photon is called antibunching.

A single photon source must emit a nonclassical number state, referred to as a Fock state, where the photon number is well defined and in this case only 1. A coherent source of light such as a laser follows a Poisson distribution with a mean photon number and will always have some probability with a photon number $\neq 1$. The quality of a single photon source can be measured by its (i) brightness (number of photons per unit time), (ii) efficiency and (iii) purity (antibunching).

(i) The brighness is determined by the QD's emission lifetime $\tau = 1/\Gamma_0$ where Γ_0 is

the spontaneous emission rate which is defined by eqn.1.6.

$$\Gamma_0 = \frac{4}{3n}\frac{\mu_{eg}^2}{4\pi\varepsilon_0\hbar}(\frac{\omega}{c})^3 \tag{1.6}$$

Where ω is the transition frequency, n the refractive index of the medium, μ_{eg} the dipole moment, ε_0 the vacuum permittivity and $\hbar$ the reduced Planck constant. Ideally the linewidth of the emitter is Fourier-transform limited. Incoherent pumping can lead to longer lifetimes and jitter in the emission time of a single photon pulse [44].

(ii) For all-optical quantum computing a source efficiency greater than 99% is desired [47]. Quantum computation is possible when the product of source and detector efficiency is $> 2/3$ [48]. In the case of Quantum Key Distribution a higher efficiency leads to a more secure connection. The efficiency of an emitter is discused in detail in section 1.3.

(iii) A figure of merit of the purity of the single photon source is a measure of its antibunched emission and can be expressed using $g^{(2)}(\tau)$, the value of the second order correlation measurement using a Hanbury-Brown Twiss interferometer (see section 3.3.2).

The first order coherence function is defined as

$$g^{(1)} = \frac{< E^*_{(t)} E_{(t+\tau)} >}{< E_{(t)} >^2} \tag{1.7}$$

and is insensitive to photon statistics and measures the phase correlations of a light field (E_t). The first order coherence is a measure of coherence time τ_{coh} and coherence length l_{coh} of the source. They give the time and length over which phase correlations are maintained.

The second order coherence function is defined as

$$g^{(2)} = \frac{< I_{(t)} I_{(t+\tau)} >}{< I_{(t)} >^2} \tag{1.8}$$

where $g^{(2)}$ only depends on the relative time delay τ between two photon detection events (I_τ) and is a conditional probability of detecting a photon at delay τ after detecting a trigger photon.

Using autocorrelation measurements one can distinguish 3 different sources of light: thermal, coherent and non classical light, by comparing $g^{(2)}(\tau = 0)$ to $g^{(2)}(\to \infty)$. The probability for simultaneous detection of two photons is increased for a thermal light source ($g^{(2)} = 2$). A $g^{(2)}(0) < 1$ demonstrates the quantum nature of the emission. For a coherent light source ($g^{(2)} = 1$) is unaltered. In case of a single quantum emitter($g^{(2)} < 1/2$) is decreased. Ideally, a single photon source has $g^{(2)}(0) = 0$, indicating the N = 1 Fock state.

Other applications of single photon sources than QIP are in metrology. Here, single photons can be used to measure small absorptions, which can not be measured with a laser source due to photon noise [49]. The shot noise $\sqrt{N}$ of a measurement where N is the mean photon number is eliminated in a single photon state measurement.

In addition, higher photon number states reduce the wavelength. The quantum mechanical wavelength is given by $\lambda_{qm} = 2\pi\hbar/p$, where p is the particle momentum. The wavelength of a single photon is given by $\lambda_{rad} = 2\pi c/\omega$ and the momentum is $p = E/c$, where $E = \hbar\omega$. Therefore the quantum mechanical wavelength λ_{qm} is equal to the radiation wavelength λ_{rad}. For a two-photon state, the momentum would be two times larger hence, $E = 2\hbar\omega$, and thus λ_{qm} would be half of that a single photon with the same wavelength and $\lambda_{qm} = \lambda_{rad}/2$. Using higher photon number states would reduce the wavelength further and reduce the diffraction limit, hence it is determined by λ_{qm} [44]. In the case of time of flight measurements, the time of arrival of each photon has a spread of $1/\Delta\omega$ where $\Delta\omega$ is the bandwidth. The error in arrival time is $1/\Delta\sqrt{N}$. For an entangled photon state the error would be N times smaller hence it has got N times higher frequency [50].

1.3 Light-matter interaction enhancement strategies

Light-matter interaction can be described as the interaction of photons with electrons and holes. The principle of light-matter interaction is used everywhere where photons are created or absorbed, for example in measurement processes. To increase the possibility of photons being absorbed or emitted, different strategies have been developed.

This chapter focuses on the ligh-matter interaction enhancement strategies with quantum dots. For practical implementation of quantum dots there is a huge challenge to be overcome: which is the efficient collection of all photons emitted by the dot. The extraction efficiency, which is the ratio of the number of photons emitted by the QD to the number of photons collected by the objective lens above the quantum dot, is $\eta = 0.9\%$ for a QD in Bulk GaAs. Due to the large refractive index missmatch of GaAs (n = 3.5) and air (n = 1), the emitted light from the dot is largely reflected back into the substrate due to the small angle of total internal reflection (see Fig.1.8). The angle of total internal reflection θ is given by Snell's law and can be calculated using eqn. 1.9

$$\theta = \arcsin(n_2/n_1) = 16.6^\circ \tag{1.9}$$

For practical applications where the light has to be coupled into optical fibers, the Gaussian HE_{11} mode is of special importance. The coupling efficiency into the optical fiber is determined by the overlap of the far-field emission of the photonic structure with the HE_{11} mode. In optical fibers, single-mode operation is preferred and the Gaussian approximation of the HE_{11} mode field distribution can be used to calculate mode propagation, dispersion, cross talk, and modulation in optical fibers and waveguide devices [51]. The main approaches to date to improve extraction efficiency by funneling the light into (ideally) the fundamental mode and directing the light into a desirable direction, where it can be collected, are optical resonant cavities and optical broadband antennas. State of the art examples of resonant cavities (see Fig.1.9 a)-c) are a pair of Bragg mir-

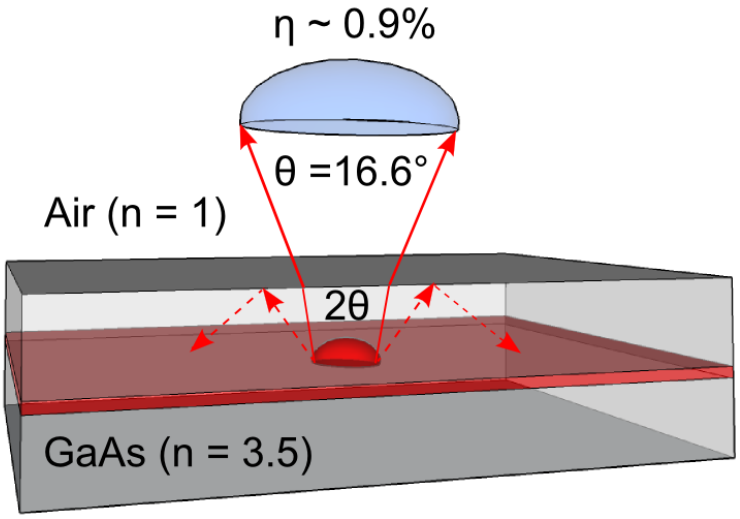

Fig. 1.8 Schematic diagram of a quantum dot embedded in GaAs. The extraction efficiency η of the light emitted by the quantum dot in bulk GaAs is only $\eta = 0.9\%$ due to the large refractive index (n) mismatch of GaAs (n = 3.5) and air (n = 1)

rors (section 1.3.1.1) [38], planar (2D) photonic crystals (section 1.3.1.2) that suppress unwanted modes using a photonic bandgap [52] and μ-discs which exploit WGM (whispering gallery modes) [45].

Examples of broadband antennas are nanowire antennas (section 1.3.2.2), planar dielectric antennas (section 1.3.2.1) and solid immersion lenses. Each of them will be introduced in the chapters below and a conclusion will summarize and discuss their advantages and disadvantages.

1.3.1 Resonant cavities

Optical cavities are used to enhance the light matter interaction. Emitters are coupled to a cavity and photons can be trapped and circulated several times before they leave the cavity. A cavity can be modelled as two mirrors with asymmetric reflectivities surrounding a two level atom (see Fig.1.9 d). As one mirror is slightly more transparent, the photons can be guided in a particular direction, leading to higher extraction efficiencies. If the emitter in the cavity or broadband antenna alignment is spatially correct and the emission frequency of the emitter matches the cavity, the emission enhancement can be described by the Purcell factor,

$$F = (\frac{3}{4\pi^2})(\frac{Q}{V})(\frac{\lambda}{n})^3 \tag{1.10}$$

where V is the cavity volume, Q the quality factor and λ the wavelength. The cavity volume is the volume occupied by a supported mode in a cavity. The cavity has ideally three dimensional photon confinement on a length scale of the photon wavelength [53]. The Q factor describes how damped the reabsorption process of the emitter and the cavity mode is.

A Purcell enhancement is usually described as an irreversible process with a decrease in lifetime and is a characteristic phenomenon of the weak coupling regime [38]. The weak coupling regime (Purcell regime) occurs when the cavity decay dominates over other rates and is defined by $g^2/\kappa_{cav}\Gamma > 1$, where g is the cavity-emitter coupling strength and κ_{cav} and Γ the cavity and emitter coherence decay rates respectively [47].

In the case where the emitter-photon interaction is greater than the quantum dot decay rate Γ combined with the cavity field decay rate κ_{cav}, one can reach the so-called strong coupling regime, where a single photon emitted by the atom can be reabsorbed. At this stage, the irreversible spontaneous emission process of the emitter is replaced by the coherent periodic energy exchange between the emitter and the photon in form of Rabi oscillations for timescales shorter than the inverse cavity decay rate [38].

In PL measurements, the strong coupling regime becomes visible as an anticrossing effect when the emitter and the cavity mode are tuned through resonance (see Fig.1.9 e). However, observing such cQED (cavity quantum electrodynamic) effects, and to reach the strong coupling regime, a large oscillator strength f, high-Q cavities and small mode volumes are required [53].

An important figure of merit to observe strong coupling is $Q\sqrt{f/V_m}$ [54]. A small mode Volume results in a high vacuum field $E_{vac} \propto \sqrt{1/V_m}$. The coupling strength $g = \mu E_{vac}$, where μ is the QD exciton dipole moment [53, 55], is enhanced when the emitter is placed inside a low mode volume microcavity.

Q can also be defined by the ratio of the emission energy of the respective cavity mode E_c and its linewidth γ_c(FWHM) ($Q=E_c/\gamma_c$). To achieve a high Q factor dissipative photon leakage out of the cavity, at a rate given by the inverse photon lifetime in the cavity mode $1/\tau_{ph} = E_c/(\hbar \cdot Q)$, represents the dominating source of decoherence in cQED experiments and has to be reduced. The following chapters will introduce two practical examples of high-Q cavities.

1.3.1.1 Micro-pillars

The concept of micro-pillars with embedded quantum dots as emitters was pioneered by Gerard *et al.* in 1996 [56]. Micro-pillar cavities are obtained by reactive ion etching (RIE) a planar cavity [57] to confine the light in three dimensions (Fig.1.10 a). They comprise of distributed Bragg reflectors (DBR) in two directions, around a 1-λ microcavity [58]. In the third dimension light is confined by the semiconductor-air interface at the pillar wall [53]. The micro-pillar far field distribution angle is highly directional and was reported to be only 10° [59]. Therefore it is well suited to be coupled into a fiber and losses can be neglected [60]. A directional outcoupling is achieved by reducing the number of layers in the upper DBR and therefore the reflectivity of the mirror.

The respective reflectivities $r_{l,u}$ of the upper and lower DBR also determine the Q-

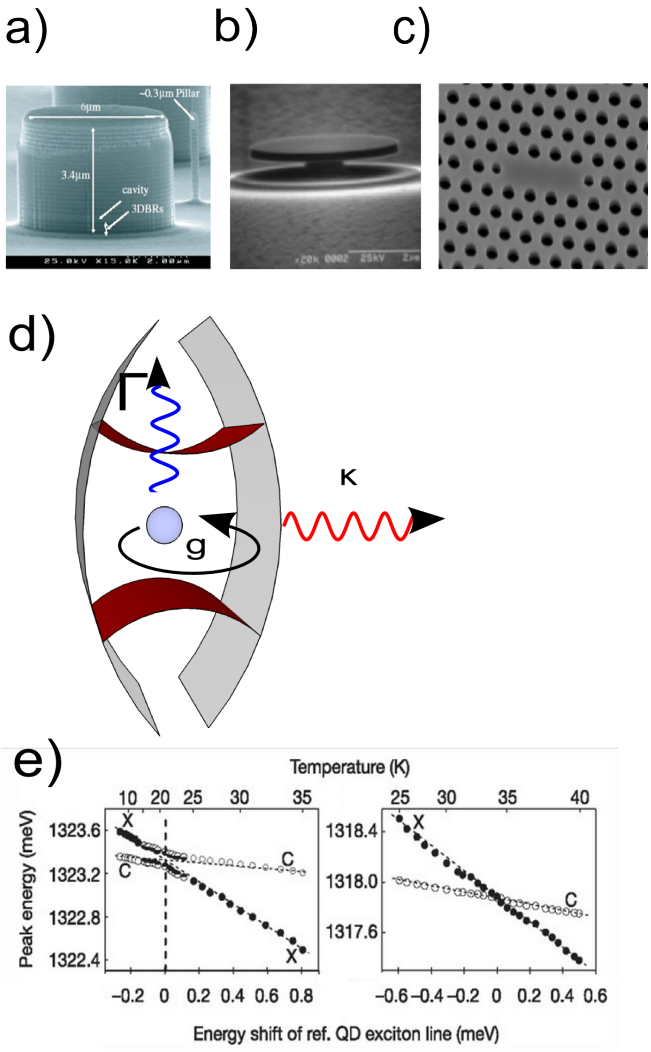

Fig. 1.9 a)-c) Examples of state of the art cavities, Bragg pillar [38], μ-disc with whispering gallery mode [45], and a photonic crystal [52]. d) Schematic diagram of a cavity shown as two concave mirrors with different reflectivities, to direct light into a particular direction. A two level atom is positioned at the electric field maximum of the cavity mode, which is determined by the cavity size. κ is the cavity field decay rate, Γ the atomic dipole decay rate and g the emitter-photon coupling parameter. If g is larger then κ and Γ combined, irreversible spontaneous emission is replaced by a coherent periodic energy exchange between the emitter and the cavity mode in form of Rabi oscillations for timescales shorter then the inverse cavity field decay rate. e) Left: PL spectra example of anticrossing as seen for strong coupling in a cavity as the emitter is tuned through resonance with the cavity mode. Right: PL spectra of weak coupling with no anticrossing when emitter is tuned through resonance with cavity mode. Data taken from [38]

factor of a micropillar and can be expressed using eqn. 1.11

$$Q = \frac{2L_{eff}}{\lambda}\frac{\pi}{1-r_l r_u} \tag{1.11}$$

where L_{eff} is the effective cavity length and λ the wavelength of light. With increasing pillar diamter more modes are supported [53], and even WGM have been reported [61]. The fraction of total emitted light and the light coupled to a guided HE_{11} mode is called the β-factor (mode coupling efficiency) and contributes to the extraction efficiency. The β-factor is defined by eqn. 1.12

$$\beta = P_M/(P_M+\gamma) \tag{1.12}$$

where P_M is the spontaneous emission into the guided mode and γ the emission into other modes [62]. The mode confinement increases when the pillar diameter is reduced, which yields large Purcell factors and improves β [57]. At the same time, small diameters open loss channels for radiative modes due to surface roughness. To reduce losses due to sidewall roughness, large diameters are preferred and lead to higher Q factors [53, 57, 63]. To reduce the mode volume V, and reach the strong coupling regime, the pillar diameter d can be reduced. To counteract the decrease in Q-factor that occurs due to leaky modes, an adiabatic pillar design has shown to partially inhibit Q-factor loss with reduced pillar diameter [57, 64].

A state of the art example was shown by O.Gazzano *et al.* [57]. The micro-pillar cavity consisted of a bottom mirror with 32 DBR pairs and a top mirror consisting of 16 DBR pairs (see Fig.1.10 a). Using this mirror configuration, light was directed towards a 0.4 NA objective lens. The cavity was fabricated around a preselected QD with high quantum efficiency (q_{QD}) using an *in situ* photolithography step [65] with 50 nm accuracy. This helps ensure that the emitter is centered in the pillar.

The QDs were selected from those with emission energies of pillar cavity modes in the diameter range of 2.5 to 3.5 μm, and from (Fig.1.10 b) it can be seen that this diameter range has the highest extraction efficiency. Smaller pillar diameters have a higher β but lower η and larger diameters have a higher η but lower β. The sample temperature was used to fine tune the spectral resonance between the cavity mode and the QD emission line. This procedure is frequently used, but is limited because at elevated temperatures linewidth broadening occur which reduces the Q factor of the cavity (see section 1.3.1). Fig. 1.10 b) shows a fit to the experimentally measured extraction efficiency $\eta = Q/Q_0$ (black dashed line where Q is the Q-factor of the pilar mode and Q_0 the Q-factor of the planar cavity). β was calculated using η and the known mode volume V as a function of diameter (see Fig.1.10 b) red dotted line). The maximum extraction efficiency is given by the product $\eta\beta$ and was claimed to be $\eta = 79 \pm 8\%$ (Fig.1.10 b). Lifetimes of τ = 265 ps $\pm$ 30 ps were measured corresponding to a Purcell factor of 3.9 ± 0.6. Second order autocorrelation measurements showed a $g^{(2)} < 0.15$ up to saturation for two pillar

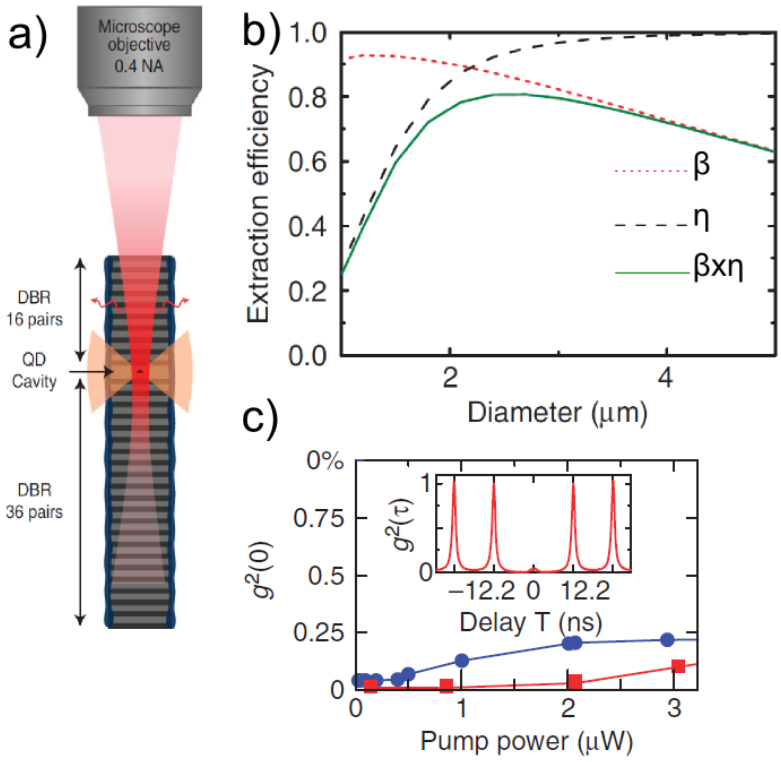

Fig. 1.10 *a*) Bragg micro-pillar schematic [57] showing DBR cavity with preselected QD ($q_{QD} > 0.9$ for neutral exciton emission) using *insitu* lithography [65]. Mirrors consist of 16 (32) DBR pairs for top (bottom) respectively, resulting in a three times higher transmission at the top for directional outcoupling, with F_P max of 3.9 ± 0.6 and lifetime of $270 \pm 30ps$. *b*) experimentally measured $\eta = Q/Q_0$ (black dashed line) calculated $\beta = F_P/(F_P + 1)$ (red dotted line calculated using η and mode volume V) and maximum extraction efficiency $\beta \times \eta$ (solid green line) vs pillar diameter. QDs were selected to match the mode energies for pillar diameters between $2.5 - 3.5\mu m$. *c*) second order autocorrelation function $g^{(2)} < 0.15$ up to saturation for two pillar cavities (red and blue).

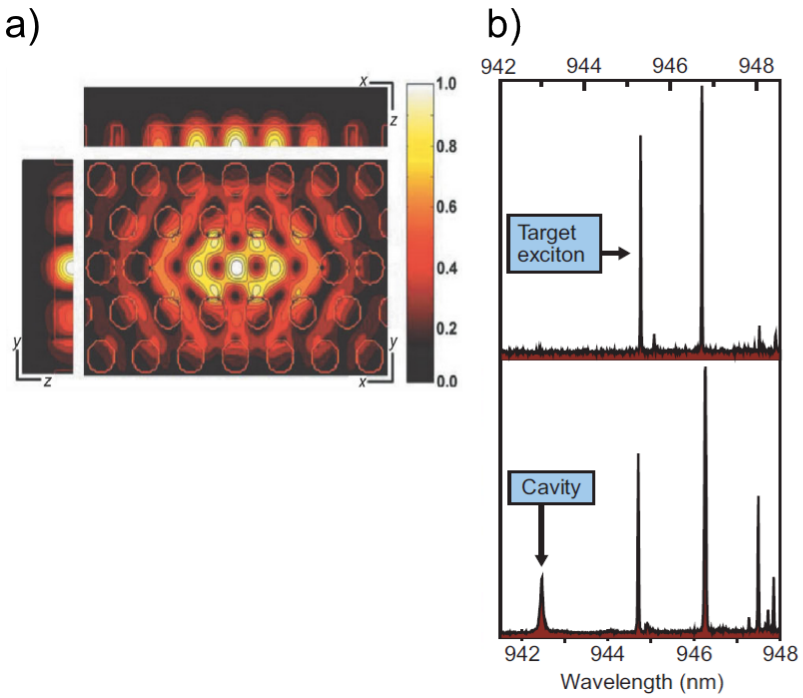

Fig. 1.11 a) Photonic crystal slab with hole spacing a = 300 nm, hole radius r = 0.27 a, shift of holes at cavity ends s = 0.20 a, slab thickness d = 0.90 a and emitter at electric field maximum [68]. b) PL spectra of QD before and after beeing coupled to a photonic crystal slab cavity. Data taken from [69].

cavities (see Fig.1.10c). This value of $g^{(2)}$ is lower for devices with a longer lifetime (see Table 1.1). Indistinguishability measurements were carried out under resonant excitation, to reduce dephasing by the electrostatic environment of carriers created in the wetting layer, and resulted in an indistinguishability of $82 \pm 10\%$ for a brightness of 0.65 ± 0.06 photon per pulse.

Strauf *et al.* demonstrated an electrically charge tunable device. The micro-pillar like structure is polarization selective by using different oxide apertures [59]. Compared to O.Gazzano *et al.*, the device has reported higher count rates into the first lens of 21 MHz corresponding to η = 26 % for X^0 and 31 MHz for corresponding to η = 38% for X^- under pulsed excitation.

It has been shown that Bragg pillars with QD as emitters can have high extraction efficiencies if the QDs are carefully preselected and the emitted light is directed in a particular direction to enhance the extraction efficiency [57]. Micro-pillars show strong Purcell enhancement of the spontaneous emission rate which is selectively enhanced into resonant cavity modes, for QDs in resonance with the cavity, whereas leaky modes are suppressed [60]. Parallel processing [12] and direct emission through optical and electrical [66, 67] pumping make micro-pillars promising candiates for single photon sources and low threshold lasers [12, 53].

1.3.1.2 Photonic crystals

Photonic crystals are man-made or natural occurring periodic changes of the refractive index in a transparent solid state material, which through diffraction and interference influence the movement of photons. Photonic crystals are better for on chip applications and enable devices that can switch light at the single photon level and consume minimal amounts of energy during operation [12]. Photonic crystals are not necessarilly crystalline, their name originates due to an analogy of x-rays being diffracted in crystalline materials in consequence of their lattice constant. Photonic crystals were independently proposed by Eli Yablonovich and Sajeev John in in the 1980's. The advantages of photonic crystals are that they can be fabricated in most semiconductors, making them integral and easily combined with current technologies.

Photonic crystals allow the guidance of light in the dimensions of the wavelength. Extreme narrow band optical filters, Bragg-reflectors and photonic crystal fibers have been realized and manufactured successfully. Photonic crystals are used in optical communication as one can create optical waveguides with smaller bending radii than optical fibers at lower losses. Entire photonic networks on a chip for efficient routing of light signals have been demonstrated [70].

The combination with quantum dots results in a variety of novel devices and effects. The photon blockade effect [71], where the presence of one photon blocks subsequent photons to enter the resonator, has been demonstrated by P.Hennessy *et al.* [69]. Purcell factors of 75 have been achieved [72].

Ideally, photonic crystals are 3 dimensional to confine light in all directions. They are made by arrangements of optical media with different refractive indices, which creates optical band gaps analogous to the electronic band gaps in semiconductors, but this manufacturing challenge in 3 dimensions is still to be overcome for near infrared wavelengths. A successful and common approach is the planar 2 dimensional photonic crystal slab. In this device, an optical band gap is created by periodic holes in a slab of semiconductor. A cavity is created by removing one or more holes in the triangular lattice (a waveguide is created by removing a row of holes) (see Fig. 1.11 a). In this way, light is confined horizontally by DBR (the photonic band gap) and vertically by total internal reflection. This method of confinement of light has shown high Q values, and small optical mode volumes V on the order of one cubic optical wavelength, ideal for strong confinement. Q is defined as

$$Q = \frac{\lambda}{\Delta\lambda} \tag{1.13}$$

where λ is the wavelenght in vacuum and $\Delta\lambda$ the cavity resonance linewidth. The cavity mode is a standing wave that oscillates from zero to a maximum at 1/4 and 3/4 λ . To couple a QD to the cavity the QD should be located at these antinodes of the electric field cavity mode. K.Hennesy *et al.* (and others) achieved this by deterministically placing a photonic crystal around a pre-selected buried QD located within 90% of the electric field

maximum. This method allowed for the study of the same QD before and after placement into a cavity. In particular, the observation of a cavity mode was made that arises in addition to the QD emission lines when the QD is placed in to a cavity (see Fig.1.11 b).

Noda *et al.* showed that a possibility to reduce the loss from the vertical confinement is to slightly move the holes at the end of the cavity [73]. The highest extraction efficiency to date has been achieved by K.H Madsen *et al.* with ($\eta = 44 \pm 2\%$) vertical out coupling over broad band due to the β-factor, which is a consequence of the photonic bandgap [74]. To achieve this high η the QD has been coupled to one particluar mode (with a lower Q = 300) of the cavity, which showed a higher out coupling efficiency compared to other modes and reduced the coupling to radiation modes strongly [75]. Simulations showed that the orientation of the dipole in the x-y plane is significant for Purcell enhancement and influences the outcoupling efficiency by a factor of 10 [74]. In addition, an air-GaAs interface 1530 nm below the photonic crystal, which reflects light and constructively interferes with the top emitted field, is suggested as the reason for a higher experimental extraction efficiency than the value determined by numerical simulations.

1.3.2 Broadband optical antennas

Broadband optical antennas do not rely on resonance effects. As a result, energy matching conditions between the emitter and the resonant cavity modes are not required. The high Q factor and high Purcell enhancement are sacrificed for broadband outcoupling of the light. This results in a high extraction efficiency over a $\Delta\lambda$ = 70-110 nm [76, 77]. The broadband outcoupling allows for the X^0 and XX exciton complexes to be simultaneously collected allowing for the realization of an efficient entangled photon pair source. State of the art examples are the dielectric broadband antenna [77, 78] (see section 1.3.2.1) and the photonic nanowire [76] (see section 1.3.2.2). The "bullseye structure", a circular dielectric grating [79], predicts efficiencies of $\eta > 80\%$ and a Purcell enhancement of 12.

1.3.2.1 Planar dielectric antenna

The planar dielectric antenna which was demonstrated by K.G Lee *et al.*, comprises of an oriented emitter placed at the interface between two media with large refractive index contrast [78]. More precisely, the emitter is placed in a medium with a low refractive index n_1 (polymer polyvinyl alcohol) in contact with a medium with a higher refractive index n_2 (saphire). Such a structure funnels the light into the high-index substrate. The distance between the emitter and the interface h determines the coupling to the output modes. The distance has to be chosen so that the light couples to output modes with small angles. To adopt the principle to QD in GaAs is challenging due to the high refactive index of GaAs. Therefore, mirrors and a solid immersion lens (see Fig. 1.12) have been added to the design principle by Yong Ma [77].

The optimized design case, for the planar dielectric antenna comprising a InGaAs

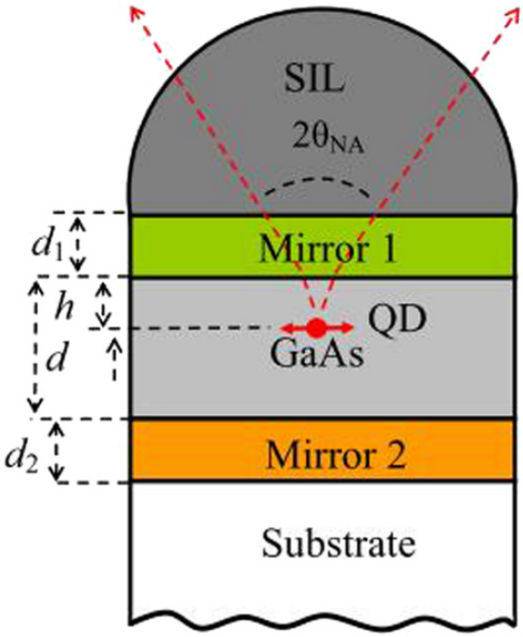

Fig. 1.12 *a*) schematic diagram of the optimized design case of the planar dielectric antenna with membrane thickness d, dipole position h, and mirror 1 and mirror 2 thickness d_1 and d_2 respectively. $2/\theta_{NA}$ is the angle of the light cone into which light is emitted from the QD [77].

QD emitting at λ = 950 nm embedded in a GaAs membrane, yields $\eta = 41\%$ and a Purcell enhancement $F_P = 1.25$ with a spectral bandwidth of 110 nm [77]. With an ideal membrane thickness of the d = 333 nm the emitter was located at the antinode of the electric field (h = 147 nm) (see Fig.1.12).

A highly reflective Au layer (mirror 2) is used to reflect all the light back towards the TiO_2/SiO_2 DBR layer (mirror 1). The Au layer functions as a Schottky contact as well as a mirror. An ohmic contact can be achieved by diffusion of Au/Ge to produce a highly doped layer grown above the quantum dot layer.

The planar dielectric antenna has the following advatages over high-Q cavities, photonic nanowires and the bullseye structure; (i) due to the 2D confinement the spatial (in-plane) positioning of the QD's can be arbitrary with respect to a cavity or waveguide mode. (ii) Electric contacts can be easily incorporated. (ii) The broad-band operataion enables efficient outcoupling to multi-chromatic transitions of the different excitonic states in the same or different QD's. (iii) Nearby free surface states which can cause dephasing are eliminated. Drawbacks of the design are a reduced extraction efficiency η and a reduced Purcell enhancement F_P compared to high-Q cavities and nanowire waveguides.

1.3.2.2 Nanowire antenna

The design criteria to optimize both the coupling of the QD emission into the fundamental mode of the nanowire waveguide and the directionality of the far field radiation is well established [62, 80, 81]. The funneling of the light is achieved over a broad spectral range $\Delta\lambda$ = 70 nm at λ_0 = 950 nm, making it highly suitable for non-monochromatic emitters

such as QD's.

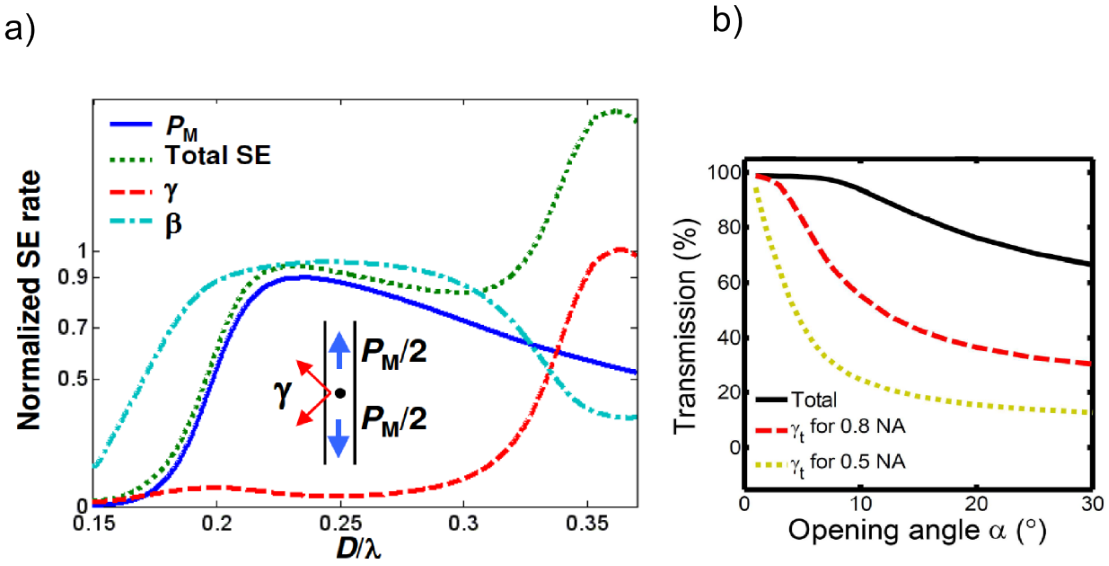

Fig. 1.13 a) Graph from [62] showing the normalized spontaneous emission rate P_M into the HE_{11} mode (blue curve). Emission into radiation modes γ is shown as a red dashed curve. Total emission $(P_M + \gamma)$ is shown as the green dotted curve. $(\beta = P_M/(P_M + \gamma))$ the mode coupling efficiency is shown by the light blue dashed-dotted curve and is the fraction of emitted light coupling to the HE_{11} mode. b) Graph showing the transmission at the taper end vs opening angle for different NA [82]

The a-FMM (aperiodic-Fourier-modal) method has been used to carry out numerical modeling of the nanowire geometry by Friedler *et al.* [62]. The results and emission properties of a emitter located on a wire axis with infinite length vs the normalized wire diamter (d/λ) can be seen in (Fig.1.13 a). A reduced nanowire diameter (d/λ) = 0.235 is found to support, and optimally funnel the QD emission, into only the fundamental guided mode in both directions along the GaAs nanowire. This is shown by the blue curve indicating the spontaneous emission (P_M) into the fundamental HE_{11} mode. The emission into other radiation modes γ is shown as a red dashed curve and is negligible, which shows the nearly perfect coupling into the single HE_{11} mode. The green dotted curve shows the total emission $(P_M + \gamma)$. The mode coupling efficiency β is shown by the light blue dashed-dotted curve and remains above 90% over a wide spectral range.

A mirror is introduced at the bottom end to reflect incident light from the spontaneous emission $P_M/2$ towards the outcoupling nanowire end (see Fig.1.14). Coupling of the light to the guided modes is optimized by placing the dot at the electric field's antinode caused by the standing wave pattern between the mirror and the emitter at distance d, which was determined to be 80 nm. A planar metallic mirror with a dielectric layer shows the highest reflectivity $R = 91\%$ over the broadest spectral range compared to Bragg and post mirrors [62, 83]. A SiO_2 dielectric layer,between the nanowire and the mirror, is used to reduce plasmonic effects and absorption losses.

At the outcoupling end, a conical taper with opening angle α is introduced to adiabatically expand the confined HE_{11} mode into a deconfined plane-wave in free space (see

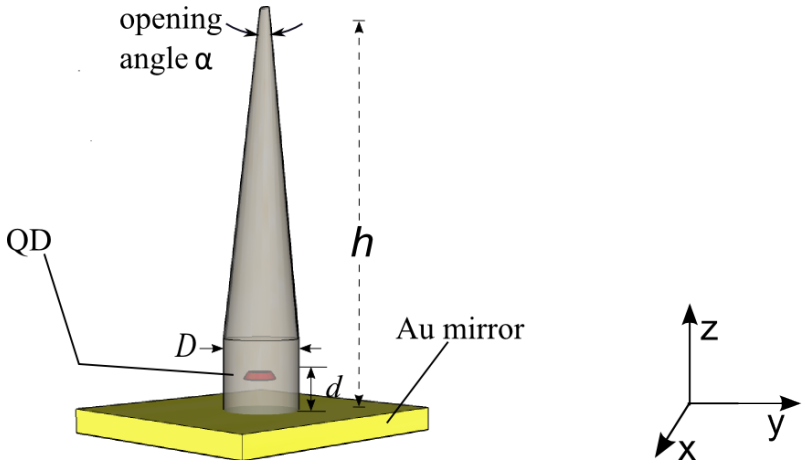

Fig. 1.14 Sketch of photonic nanowire with pillar diameter D, height h. Top taper angle α and QD to Au mirror distance d.

Fig.1.14). The angle of the conical tapering α determines the transmission of the guided mode at the divergence angle of the far-field radiation pattern (see Fig.1.13 b). For angles $\alpha \sim 5^\circ$ the transmission T can be $T > 90\%$. Reducing the top taper diameter below 120 nm does not show any improvement in T [82]. The theoretical extraction efficiency of the photonic nanowire is given by the Fabry-Perot model

$$\eta = \frac{1}{2}\beta \frac{(1+|r_m|)^2}{1+\beta|r_m|} T_\alpha(sin\theta) \tag{1.14}$$

where $|r_m| = 1$ is the modal reflectivity for perfect mirrors and $T_\alpha(sin\theta) = 1$ the far field transmission into free space for a perfect taper [62, 76, 81].

Claudon *et al.* successfully fabricated a device with a claimed extraction efficiency of η = 72 % and $\Delta\lambda$ = 70 nm using non-resonant optical pumping [76] and a NA = 0.75. This high extraction efficiency over a broad spectral range allows for probing of the QD over its entire emission wavelength. The measurement of the auto-correlation function a $g^{(2)}(0) < 0.008$ was measured above saturation; this is below the values measured for QD-cavity structures [59], where the suppression of multiphoton emission was only achieved under low pump powers or by resonant excitation schemes.

Time-resolved photoluminescence measurements were carried out and measured the QD emission rate with changing normalized wire diameter (d/λ) [84]. It was experimentally shown that the Purcell factor moderately increased to 1.5 for $(d/\lambda = 0.25 \pm 0.01)$. Other work showed that the lifetime consistently reduced with increasing pillar diameter and was found to be as low as 1.7 ns at d/λ = 0.245 [85]. On the other hand, strong inhibition was observed below d/λ = 0.16 [84] and d/λ = 0.18 [85].

Both strong inhibition into radiative modes and moderate SE enhancement confirm the potential of photonic nanowires to achieve $\beta > 0.9$ for on-axis emitters. $\beta > 0.9$ is achievable for d/λ = 0.20-0.29 which further relaxes fabrication constrains [76]. For off-axis emitters a β-factor of 0.9 with a normalized displacement approximately 25% of the wire radius was established using fully vectorial calculations. In addition, a perfectly

circular pillar is not polarization sensitive, only elliptical pillars have been shown to enhance spontaneous emission into a certain polarization. In a pillar, the dipole orientation along the x-y plane can be arbitrary. However, nanowires show 11 times higher Gaussian emission intensity profile when the dipole is in the x-y plane, perpendicular to the wire axis z [86]. By imaging the far field emission using a CCD camera it was observed that only the single HE_{11} mode is supported, for $d/\lambda > 0.23$ the nanowire supports an additional TE_{01} mode and at $d/\lambda > 0.25$ an additional TM_{01} mode, making the nanowire a multimode waveguide. From the far field imaging it is evident that as more modes are supported emission is directed into wider angles. The far field emission of the nanowire is Gaussian and overlaps by 98.8 % with an optical fiber far field. A 93 % $\pm$ 3 % coupling efficiency into an antireflection coated fiber with NA = 0.1 of the Gaussian HE_{11} mode was claimed. The nanowire geometry allows fiber coupling near unity [86], which has not been achieved with planar cavities ($\eta \approx 45$ %) [87] and micro-pillar cavities ($\eta \approx$ 70 %) [88].

The high extraction efficiency over a broadband, the high tolerance of the emitter location compared to other structures and the high coupling effcieny of HE_{11} into an optical fiber make the nanowire antenna the ideal choice for optical studies of QDs.

1.4 Conclusion

InAs QD's are well suited for quantum photonic applications due to their excellent quantum efficiencies, single photon emission and a variety of quantum states that can be optically controlled. They can as well be incorporated into semiconductor heterostructures, that can be manufactured using technologies already developed in the semiconductor industry (see Tab. 1.1 a - e). In case of a single photon source, K.H. Madsen et al. emphasizes the importance of the count rate (number of detected photons) and prioritizes them over the source collection efficiency η [74]. Table 1.1 shows important figures of merit for optical cavities and broadband antennas with embedded QDs. The count rate, extraction efficiency η , Purcell enhancement F_P, single photon purity $g^{(2)}(0)(\%)$ and visibility of indistinguishability, important for QIP applications, are listed.

	Countrate (kHz)	$g^{(2)}(0)(\%)$	$\eta(\%)$	F_P	Ind.(%)
a) Photonic crystal	293	4	44.3	6	70 %
b) μ-pillar	700	15	79	3.9	82%
c) μ-pillar	4000	40	38	2-4	NA
d) Nanowire	65	0.8	72	1	NA
e) Planar antenna	4000	0.1	12	1	> 90%

Table 1.1 State of the art figures of merit reported in literature for single photon sources [74], count rate in (kHz), $g^{(2)}(0)(\%)$, extraction efficiencies η, Purcell-factor $F_p = \gamma/\gamma_{bulk}$. The table list includes a) Photonic crystal [74], b) Micro-pillar cavity (free standing) [57], c) Micro-pillar cavity (electric contacts)[59], d) Photonic nanowire [76], e) Planar antenna [77, 89].

Most notably there is a discrepancy between count rate and extraction efficiency between the experimental reports which is most likely due to poor coupling optics. Compared to micro-pillars, photonic crystals have higher Q-factors and lower mode volumes. A disadvantage of PC's is the lower and (in plane) dipole orientation dependent extraction efficiency [74]. A perfectly circular pillar on the other hand is not polarization sensitive, only elliptical pillars have shown to enhance spontaneous emission into a specific polarization [81]. However, the dipole needs to be oriented along the x-y plane, and not parallel to the wire z-axis to achieve a high intensity Gaussian far field emission pattern [86]. By carefully preselecting a QD and directing the emitted light in a particular direction, micro-pillars can have higher extraction efficiencies and count rates than photonic crystals (see Tab.1.1 b - c). In general, cavities have low mode volumes, high Q values, high Purcell factors and enable strong light-matter interaction. The disadvantage of cavities is the need for high accuracy of spectral and spatial matching of the emitter to the cavity mode, which are both vital for Purcell enhancement.

In contrast broadband optical antennas are less sensitive to the dipole location, orientation and emission wavelength than optical cavities. Broadband antennas sacrifice the high Q-factors and high Purcell enhancement for enhanced extraction efficiency over a broader spectrum ($\Delta\lambda$ = 70 - 110 nm) [76, 77].

Planar dielectric antennas outperform state of the art photonic crystals with low $g^{(2)}$ (designed for high outcoupling) and high photon indistinguishability. They compete with micro-pillars as well showing similar count rates (see Tab.1.1 c), with an outcoupling efficiency over a broader range including charge tunability. The disadvantage is that planar dielectric antennas have a relatively low extraction efficiency. Nevertheless, due to better optics very high count rates have been achieved.

The nanowire antenna has a higher extraction efficiency than the planar dielectric antenna and PC. The Gaussian far field emission pattern (HE_{11}) of the nanowire antenna is optimal for coupling into single mode fibers. The arbitrary dipole orientation along the x-y plane, and high tolerance of the axial position, while still enabling a high β, make the nanowire easier to fabricate then resonant cavities. The high theoretical extraction efficiency of 90% is very promising and could enable practical QIP technologies. The high broadband extraction efficiency ($\Delta\lambda$ = 70 nm) allows the use of QDs with a variation in confinement energies.

In summary, nanowires have a higher extraction efficiency than planar dielectric antennas combined with a low $g^{(2)}$. We can conclude that due to the nanowire antenna's high extraction efficiency and broad optical outcoupling, it is quite suitable for a tunable light emitting device.

Chapter 2

Nanowire antenna fabrication

To fabricate a waveguide on the order of the wavelength of infrared light, nanometer precision is essential and state of the art nanofabrication equipment is required. This chapter will discuss each technique used in the fabrication procedure and show the fabrication results. To fabricate a strain tunable photonic nanowire with an embedded QD, the following procedure has been established.

Our fabrication procedure is summarized in Fig. 2.1. A wafer grown by molecular beam epitaxy (MBE) was cleaved by hand and cut into smaller fragments using a dicing saw (see section 2.1). A 100 nm (Au) mirror is deposited by electron beam evaporation (see section 2.2). After this, the wafer is inverted and bonded to a PMN-PT crystal with a 100 nm-thick Au layer using a thermo-compression bonding step at a temperature of 300° C and at a pressure of 2 MPa respectively (see section 2.3). Hydrochloric acid at 0° C is used to selectively etch the 1000 nm $Al_{0.65}Ga_{0.35}As$ sacrificial layer, allowing removal of the substrate wafer. Next, an e-beam-lithography shadow mask is defined in a 220 nm layer of PMMA/MMA [Poly(methyl methacrylate)] (see section 2.5) for a 90 nm-thick Ni dry-etch mask deposited by e-beam evaporation. The PMMA/MMA is removed using acetone in an ultrasonic bath to expose the Ni discs which act as masks for the final dry-etching process using $SiCl_4$/Ar (see section 2.6). The sample was immersed in Dilute Nitric acid (1:10 HNO_3:H_2O) for 180 s to remove remaining Ni and to improve the taper angle. This resulted in the high efficiency nanowires characterized in the thesis. The methods used to prepare the samples for PL measurements and the electric contacting of the piezoelectric crystal are discussed in section 3.4.

2.1 Sample preparation

A two inch wafer, grown and characterised by Faebian Bastiman, Andrew Griffiths and Edmund Clarke at the III-V Nanotechnology Centre in Sheffield was used. The sample (wafer Nr.VN2459) was characterized by PL spectroscopy to create a wafer map. X-ray Diffraction (XRD) was used to confirm the composition as $Al_{0.65}Ga_{0.45}As$. Nomarski microscopy was used to assess the surface defect density as "low". The layer structure

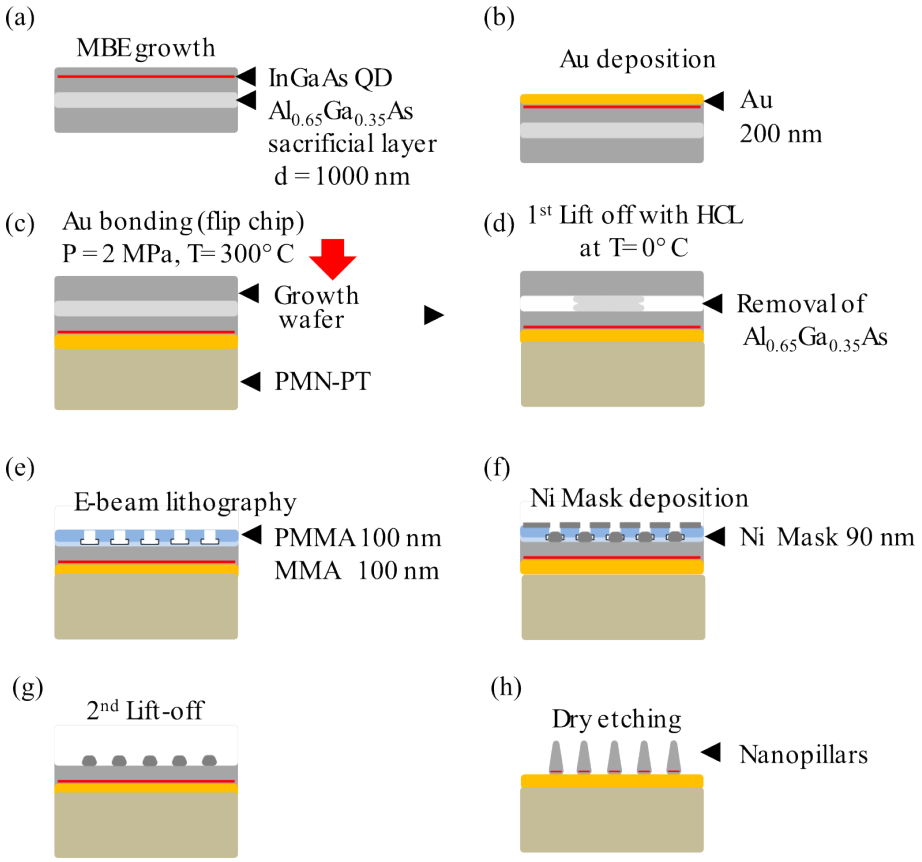

Fig. 2.1 A schematic of the fabrication procedure. (a) A sample consisting of self-assembled InGaAs quantum dots with a 110nm-thick capping layer and embedded in a 2 μm GaAs layer on an $Al_{0.65}Ga_{0.35}As$ sacrificial-etch layer is grown by MBE. (b) A 100 nm Au back mirror is deposited. (c) Following a flip-chip process, the Au layer is attached to the Au-coated PMN-PT crystal using Thermocompression bonding ($T = 300$ C$^\circ$ and $P = 2$ MPa). (d) Hydrochloric acid at $T = 0^\circ$ C is used to selectively etch the $Al_{0.65}Ga_{0.35}As$ layer. (e) Electron beam lithography is used to define circular apertures of the desired radius. (f) 90 nm of Ni is deposited followed by (g) lift-off in acetone to remove resist and (h) dry etching of nanowires.

consisted of a 1000 nm $Al_{0.65}Ga_{0.35}As$ sacrificial-etch layer (lift-off) followed by a 2 μm thick GaAs layer within which a layer of InAs QDs were grown 110 nm from the surface (see Fig. 2.2 c). To accelerate the lift-off process, small samples were required, Which were too small to handle individually. Samples of 5x5 mm^2 were cleaved using a diamond scribe see (Fig.2.2 a). From one piece, sections of 0.5 x 0.5 mm^2 were diced with 100 μm grooves using a dicing saw (Disco DAD 320) (see Fig.2.2 b). The wafer was then cleaned in a ultrasonic bath using acetone to remove any GaAs flakes from the surface. Prior to metal deposition oxygen plasma cleaning was carried out. The PMN-PT was cleaned in a oxygen plasma as well, prior to metal deposition.

2.2 Electron beam evaporation

Electron beam evaporation is a physical material deposition technique where a source inside a crucible is heated with an electron beam. An electron beam is directed using

a) b) c)

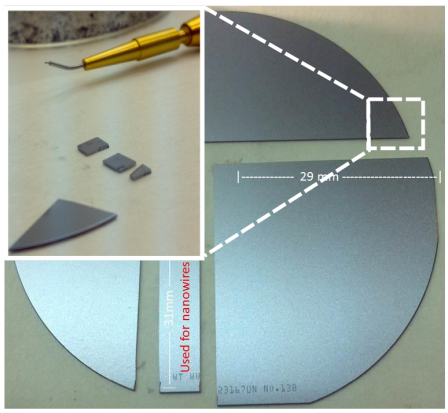

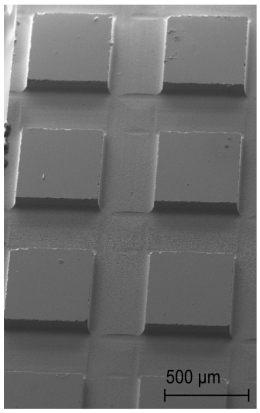

VN2459 (design 7):

Epi-Structure definition

	Material Composition	Thickness
Layer 5	GaAs	110 nm
Layer 4	InAs QDs	
Layer 3	GaAs	2000 nm
Layer 2	$Al_{0.65}Ga_{0.35}As$	1000 nm
Layer 1	GaAs	200 nm

Fig. 2.2 Samples from a two inch wafer (sample VN2459) were first a) cleaved into 5 x 5 mm squares by hand using a diamond scribe. b) The samples were then cut aprox 100 μm deep into 0.5 x 0.5 mm squares using a dicing saw. The SEM image shows a diced wafer piece. The squares are small to reduce lift-off time, but each square is large enough for the intended e-beam lithography pattern to be completely written within the 0.5 x 0.5 mm squares. c) Layer composition of the wafer.

electromagnets onto the evaporation source causing fast spot heating and evaporation. The evaporated material travels upward towards the sample where it resolidifies. For metal deposition, an Airco Inc. electron beam evaporator chamber was used (see Fig. 2.3). Prior to metal depostion, the GaAs pieces were immersed in 1:18 NH_4OH/H_2O_2 to remove the native oxide layer. Alternatively, an oxygen cleaning plasma was used.

To create a planar mirror the samples can be coated with Au [76]. The Au layer also acts as a bonding medium in wafer bonding [90]. To improve bonding between the GaAs substrate and the Au layer a 5 nm Cr or TiO_2 intermediate adhesion layer was deposited prior to Au deposition. Ni evaporation for the dry etch mask did not require an adhesion layer. For metal deposition, the samples were mounted on a two inch glass wafer using vacuum grease. PMN-PT samples were mounted using vacuum tape. The samples were then placed face down into the sample holder carousel (see Fig. 2.4 c).

The piezoelectric crystal in the film thickness monitor (FTM) was replaced prior to every evaporation to avoid failure during evaporation. When calibrated and positioned correctly thickness changes of 1 Å can be measured. The samples, the evaporation sources, the thickness monitor and an observation mirror had to be aligned before the chamber was sealed and evacuated. The e-beam chamber was evacuated down to 4×10^{-6} mbar using a oil diffusion pump backed up by a rotary roughing pump. The pressure was measured using an Active Inverted Magnetron Gauge (Edwards AIM-S-NW25). A LN_2 cold trap was filled with 5 l of LN_2 after the pressure reached 10^{-3} mbar.

Evaporation was carried out at pressures of 10^{-5} mbar. The power and position of the electron beam had to be adjusted manually throughout the evaporation process. This was essential to keep a constant evaporation rate and to inhibit over heating and contamination

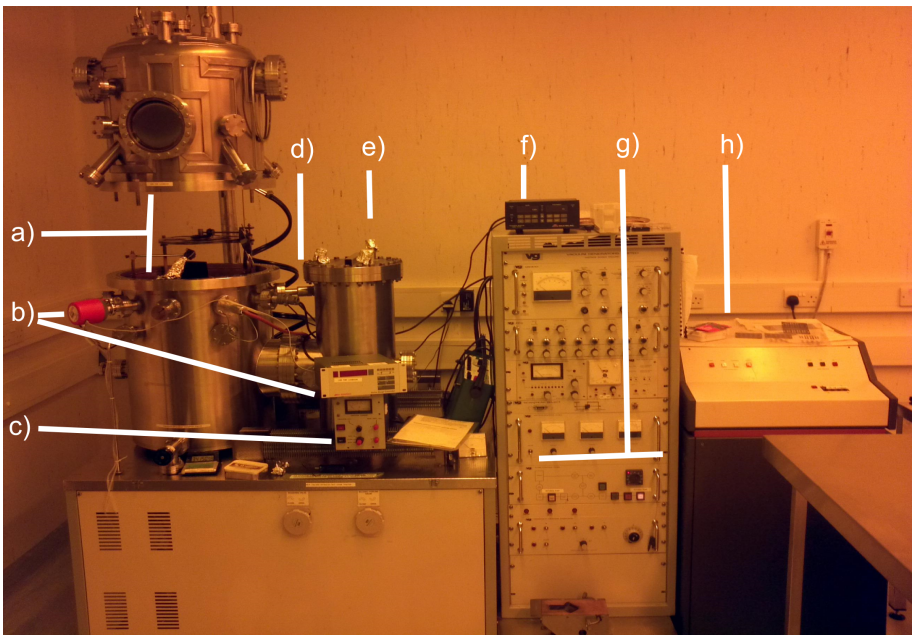

Fig. 2.3 E-beam evaporator with a) evaporation chamber, b) pressure gauge, c) electron gun power and xy-position control, d) sample-holder rotator, e) LN_2 cold trap, f) thickness monitor, g) diffusion pump controll panel, h) power supply for electron gun.

of the evaporation source. Electron beam currents of 15 - 25 mA were used. The thickness and evaporation rate was monitored using a film thickness monitor (FTM SF-290). Evaporation rates between 0.5 and 0.9 Å/s for Ni and 1 - 3 Å/s for Au were used while manually sweeping the electron beam over the source.

All metals seemed to adhere better to the samples, even after sonication, when an oxygen cleaning plasma was used.

If the evaporation source used in the graphite cuvette was smaller then the e-beam spot size (d = 1 cm), graphite was evaporating as well as Au. This leads to severe contamination of the metal layer, which was observable under the optical microscope showing graphite impurities on the metal surface. If the impurities are visible by eye, it means they are larger than the 100 nm Au thickness and inhibit bonding. Larger sources should be used to avoid contamination.

Ni was evaporated from a sufficiently large source. The right temperature (via electron gun current) was difficult to control, and evaporation rates above 2 Å/s often lead to spitting of the Ni source and occasionally resulted in failure of the thickness monitor. The surface of the metals evaporated consisted of 20 - 30 nm size metal clusters (see Fig.2.5 a)-c). The metals evaporated onto a polished GaAs surface seem to have fully covered the surface (see Fig.2.5 a), whereas the metal layer evaporated onto the PMN-PT shows gaps (see Fig.2.5 b). This became evident when placing the PMN-PT into a HF bath. The Au layer started to peel off and the etched PMN-PT was visible.

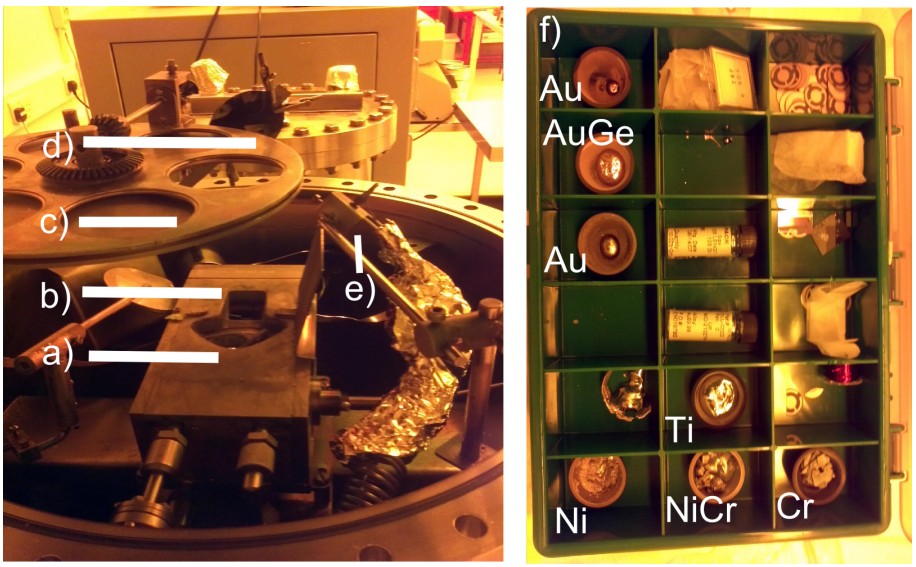

Fig. 2.4 Inside of e-beam evaporator with a) evaporation source rotator, b) hole for electron beam, c) sample rotator, d) observation mirror, e) thicknes monitor, f) evaporation sources.

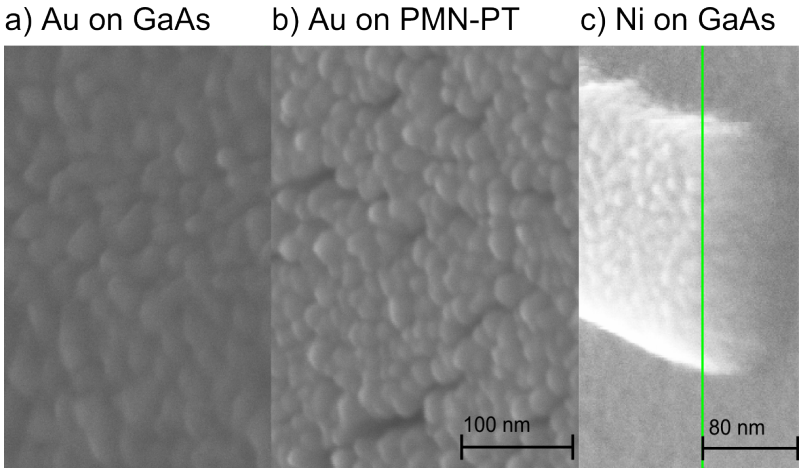

Fig. 2.5 SEM images showing the surface of a) Au on GaAs (d = 100 nm), b) Au on PMN-PT (d = 100 nm) and c) Ni on GaAs (d = 90 nm). The Au on PMN-Pt shows gaps in between the 20 - 30 nm metal clusters.

2.3 Thermocompression bonding

Wafer bonding was carried out using a thermocompression bonding step. Other bonding methods such adhesion using epoxy, or hydrogen bonding were found to be unsuitable. They were of bad quality or interfered with the subsequent fabrication procedures. The Au coated GaAs wafer with a 500 x 500 μm^2 checkerboard pattern and a 10 x 10 mm^2 PMN-PT sample coated on both sides with Au were brought into contact using tweezers under a laminar flow cabinet. Great care was taken not to create any lateral movement and scratch the 100 nm Au layer on either side. The two parts had to be aligned so that the sides were parallel to each other. This allowed easier navigation using xy nanopositioners during the following e-beam writing step and the optical characterization of the finished device (see chapter 3).

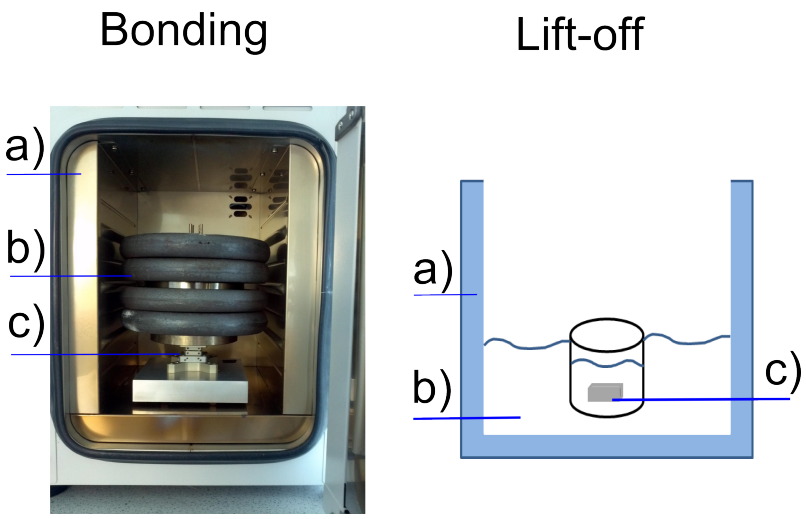

Fig. 2.6 Bonding: Setup for thermocompression bonding with a) oven b) weights and c) aluminum chucks with samples. Lift-off:sketch of lift-off setup with: a) Styrofoam container, b) ice water and, c) PTFE beaker with HCl and sample.

The samples to be bonded were placed between two sheets of lens tissue, which seemed to inhibit random cleaving of the sample during the thermal cycling. The lens tissue also inhibited bonding of the Au PMN-PT to the wafer bonder. The samples were placed into a home built wafer bonder (see Fig. 2.6). Weights were placed on top of the sample to reach pressures of 8 MPa for GaAs-GaAs Au bonding. The wafer bonder was placed into an oven (Binder ED23) and annealed for approximately 7 hours at 300 ° C. After bonding the sample was cleaned using acetone and a cotton bud to remove any lens tissue residue. The GaAs-GaAs bonded samples were thermally cycled in LN_2 and deionized water at room temperature. The bonding strength was tested by attempting to pull the wafers apart with tweezers, which was not possible. The PMN-PT was more brittle then GaAs therefore only 2 MPa pressure was used. This was sufficient for bonding, but no assessment of the quality of the bonding at these low pressures was made. At higher pressures the GaAs bonded very well to the PMN-PT, but the sample fragments were to small to be used for further processing.

2.4 Lift-off

The lift-off process which separates the growth wafer from the membrane containing the QDs was first attempted in 7 % HF for GaAs samples. However the PMN-PT crystal was etched by HF and the Au contacts flaked off. Therefore, highly concentrated HCl at 0 °C was used as it has better selectivity for PMN-PT. At 0 °C, the etch rate of the PMN-PT and GaAs is negligible compared to the the etch rate of the AlGaAs etch layer [91]. A styrofoam container was filled with ice (see Fig. 2.6). A PTFE beaker was placed into the ice bath and filled with 47% HCl acid. The styrofoam container was placed into a fridge which increased the melting time of the ice to approximately 24 hours. This allowed for an etching process to take place over 3-4 days continuously. The lift-off in HCl took

considerably longer, approximately 4 days for a 0.5 x 0.5 mm^2 membrane size (see Fig2.7 a). Lift-off in HF only required 24 h for a 5x5 mm^2 membrane size (see Fig2.7 d). The HF lift-off was faster and cleaner with less contamination of the sample surface (see Fig2.7 c). The HCL lift-off left a layer of cluster-like residue which acted as a micromask in the dry etching process (see Fig2.7 b).

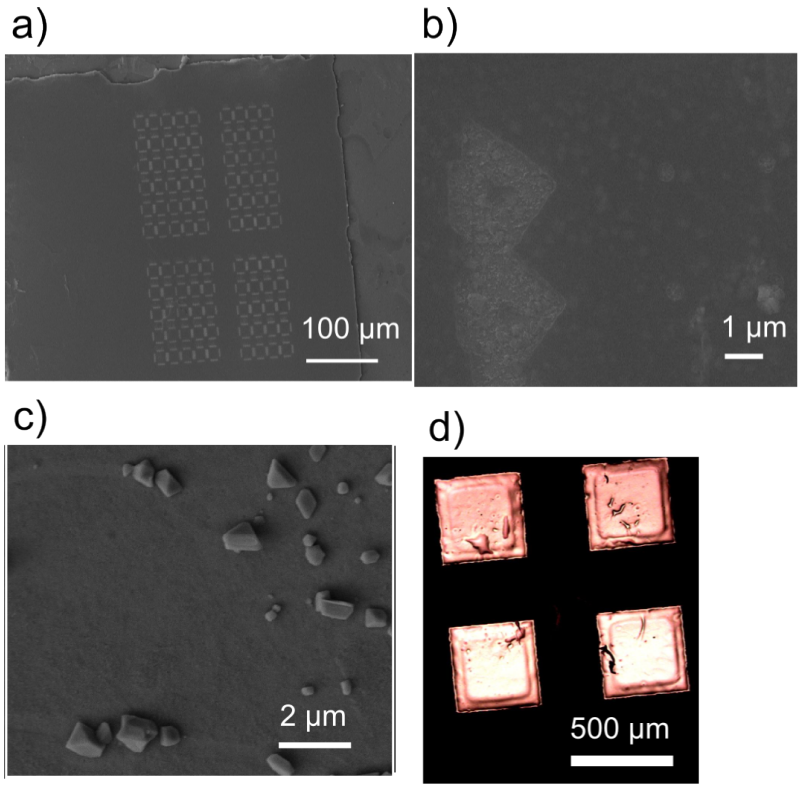

Fig. 2.7 SEM images showing a) GaAs membrane bonded to PMN-PT. b) GaAs membrane showing redeposition / etching after lift-off using HCl. c) GaAs after lift-off using HF with redeposition of AlGaAs sacrificial layer. c) Optical microscope image of GaAs membranes on flexible polymer.

2.5 Electron beam lithography

In electron beam lithography (EBL), a beam of focused electrons is used to alter the chemical composition of a resist. The electron source commonly used is a thermally assisted field emission gun [92].

A scanning electron microscope (SEM) is an integral part of a EBL system. In an SEM, magnetic lenses are used to focus the emitted electrons onto the sample. Deflectors are used to move the electron beam and to blank the beam. The acceleration voltage of the electrons ranges from 1-500 kV [92]. Voltages greater than 250 kV can cause damage to the underlying substrate. The advantage of high energy electrons is less forward scattering and therefore higher contrast but the backscatter range increases with an exponential factor of about 1.7. A good backscatter yield for III-V materials can be found at an acceleration voltage of 140 kV [92].

The pattern to be written is drawn in CAD software and saved as a GDSII file which can be interpreted by the e-beam lithography control software. Due to scattering, complex structures need proximity correction. The dose (in $\mu C/cm^{-2}$) of electrons applied to the resist needs to be exact. If the dose exceeds the required amount the resist hardens instead of softening. On the other hand, unwanted areas between closely spaced features can be exposed which lead to deformation of the intended structure. To compensate for overexposure one can write smaller structures or, one can create several layers in the GDSII CAD file. Commercial software and features in the EBL-system software for proximity correction are available. 3D proximity effect correction should be used for features below 50 nm.

The system used in this thesis is a Raith PIONEER (Fig.2.8). It is a new compact electron beam lithography (EBL) system based on thermal field emission (TFE) technology. The SEM column is manufactured by Zeiss with acceleration voltages ranging from 1-30 kV. It is equipped with a secondary electron detector and an InLens detector which significantly improves secondary electron collection efficiency for enhanced bright high contrast imaging. The InLens detector achieves high image quality at low voltages and therefore delivers excellent sample surface information. The PIONEER is a EBL/SEM hybrid with a third-party pattern generator. The sample stage is controlled by a laser interferometer. The manufacturers system specifications are listed below in Table 2.1.

Beam size (resolution)	2.5 nm (1.6 nm)
Minimum feature size	20 nm
Field stitching	50 nm (mean+2σ)
Overlay accuracy (alignment)	50nm (mean+2σ)
Laserstage travel range	50x50x25 mm

Table 2.1 Raith Pioneer main specifications for EBL system as stated by manufacturer (Raith GMBH).

2.5.1 Spin coating

Prior to spin coating, the GaAs wafer was heated on a hot plate for 2 min at 170°C to remove any moisture on the surface. An oxygen cleaning plasma was used if heating was not sufficient . The temperature of the hot plate was measured using a surface thermometer calibrated against a pyrometer. The resist is spin coated onto a GaAs substrate using a spincoater (Spin 150, see Fig. 2.9 a). A 4 mm thick aluminum chuck, with a 0.5 mm diameter hole suitable for the 5x5 mm samples was used.

After the wafer piece has been placed onto the chuck a N_2 gun was used for a final time to clean the wafer prior to applying the e-beam resist. A spin speed up to 6000 rpm is used to control the resist thickness. The resist is a polymer diluted in a solvent. In this case polymethylmethacrylate (PMMA) in Anisole (michrochem 950 PMMA A 5%) and methylmethacrylate (MMA) in ethyl lactate (MMA(8.5)MAA EL 6) as a copolymer for a

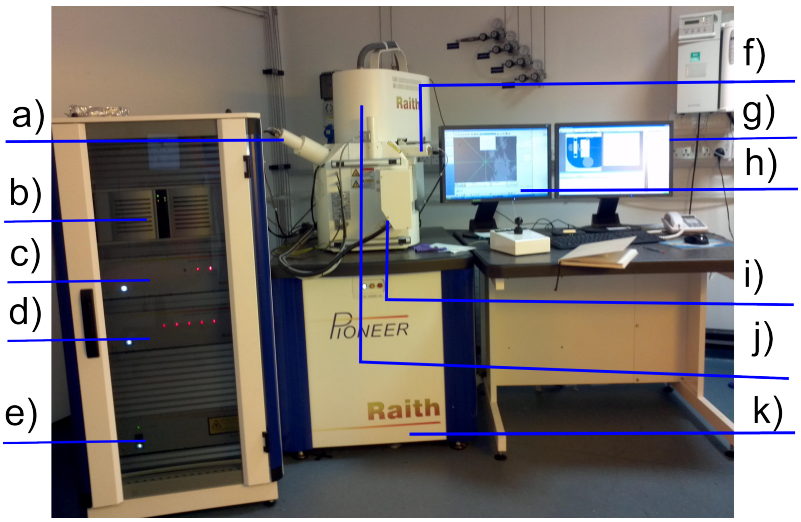

Fig. 2.8 Photograph showing Raith pioneer EBL system with a) SE2 detector, b) PC, c) beam blank controller, d) precision stage controller, e) laser interferometer source, f) InLens detector and control monitors for g)EBL and h) SEM, i) sample load lock, j) SEM column, k) floating table.

bi-layer process was used. If the desired resist thickness cannot be achieved the viscosity of the resist is reduced by dilution with the appropriate solvent.

For enhanced lift-off, a bi-layer of PMMA and MMA was used. A 3% MMA in ethyl lactate solution was applied using a micropipette. The MMA wets the surface of the GaAs wafer and does not bead up, signifying that the moisture has been removed sufficiently. The resist was spin coated at 6000 rpm for 90 s with a ramp up speed of 500 rpm/s. The wafer was baked on a hot plate for 2 min at 140° C to remove the remaining solvent. A hot plate is used, as it reduces the bake time from 30 min to 90 sec compared to an convection oven, due to a faster heat transfer.

A second layer of resist, 3% PMMA in Anisole solution was spin coated on top of the MMA. Spin coating was carried out for 90s. A thickness of 100 nm was achieved at spin speeds between 5000-6000 rpm. After spin coating, the wafer was again baked on a hot plate at 140 °C for 2 min. The thickness of the PMMA/MMA dual layer was confirmed by scratching the PMMA with a scalpel and measuring the grooves with a DekTak profilometer.

2.5.2 SEM

For the EBL step, the samples were clamped to a grounded sample holder. The wafer clamp held the sample in place and acted as ground. Before each e-beam writing step the SEM was aligned. This involved several iterations of focus, stigmatization and aperture alignment. As a guide for the eye a small drop of Polystyrene (PS) spheres d = 120 nm (agar scientific S130-1 5 ml) were placed at the left bottom corner of the sample using a sharp object. PS spheres were imaged with low acceleration voltages (10 kV) (see Fig.2.10 a). At high acceleration voltages (30 kV) the polystyrene spheres became

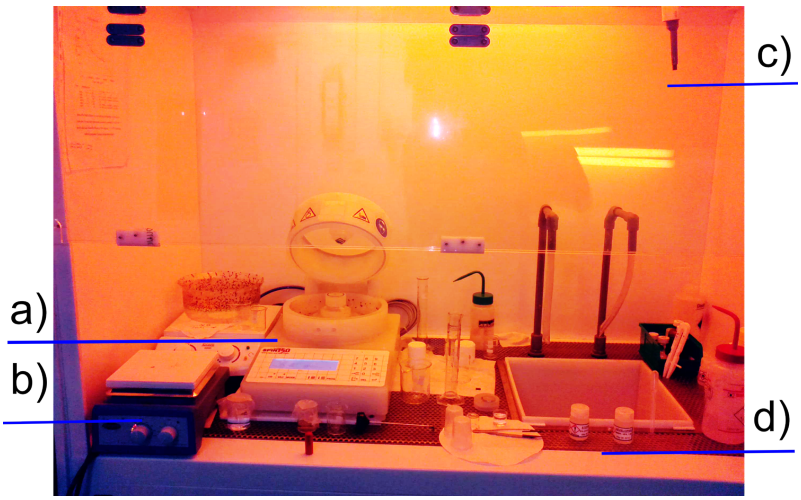

Fig. 2.9 Laminar fume hood used for sample preperation with a) spin coater, b) hotplate, c) micropipette d) chemicals for resist development and removal. The spin coater has been calibrated and programmed for the desired resist thicknesses

.

transparent, therefore Au colloids with particles 100 nm in diameter (Gold Colloid:100nm BBInternational) were used (Fig.2.10 b). The spheres/particles were used to aid focusing and alignment of the SEM. The working distance was set to 6 mm, which is the optimized distance for the EBL. The shorter the working distance, the smaller the focal spot of the electron beam, and therefore the better the focus. The acceleration voltage of the electron gun can be switched on when the sample chamber reached a pressure below 2.5×10^{-5} mbar. The global coordinates of the sample position (XY) were read in and assigned to a local coordinate system (UV) that compensated for the rotation of the sample with respect to the sample holder. The SEM focus, stigmatization and aperture alignment have to be fine adjusted prior to every imaging or writing procedure and the settings are only valid for a certain combination of acceleration voltage, working distance and aperture size used. To check the quality of alignment of the SEM, a close up of a high contrast structure, i.e closeup of a Ni mask shows "noise ripples" of 5 nm size (see Fig.2.10 c). Commonly, values between 3 - 7 nm have been achieved demonstrating good alignment. In addition, the electron beam profile was measured by zooming in completely and keeping the electron beam at the same spot for 3 - 180 s. The electrons accelerate in the sample chamber towards the sample surface. The build-up of impurities on the sample surface creates an image proportional to the cross-section and height of the Gaussian beam profile of the electron beam intensity distribution. From the shape and size of this "image" one can determine the quality of alignment (see Fig.2.10 d). A circular spot size is a measure of good stigmatization alignment,but if the spot is elliptical the stigmatization has to be repeated. A high intensity area in the centre of a circle is a measure of good aperture alignment. If the majority of contamination is not deposited in the center of the spot, the aperture alignment has to be corrected. Spot sizes of 20 nm are desired, as they are a measure of focus quality,and the alignment procedures have to be repeated until a circular Gaussian spot between 20-50 nm size is achieved.

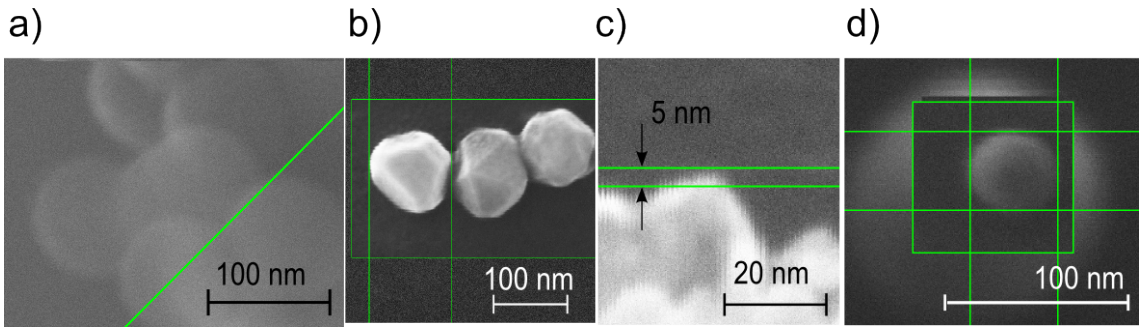

Fig. 2.10 Shows SEM images with nanoparticles used for SEM alignment. a) Polystyrene spheres d = 100 nm were used for low acceleration voltages (10 KV). b) Au colloid d = 100 nm was used for high acceleration voltages (30 KV). c) closeup of a Ni mask showing "noise ripples" of 5 nm size. Commonly values between 3 - 7 nm have been achieved. d) A "burned spot" made by holding the electron beam still. Both c) and d) are a measure for good alignment of stigmation, aperture and focus.

2.5.3 E-beam resist exposure

After a successful beam alignment as described above, the beam current can be measured by directing the e-beam into a Faraday cup which is built into the sample holder. Beam currents ranged from 300 pA using a 30 μm aperture to 30 pA using a 10 μm aperture. The acceleration voltage has an influence on the beam current as well; at 10 kV the beam current was 190 pA while at 30 KV the beam current was 300 pA using the 30 μm aperture. The dose was set to 330 μC/cm^2 at 30 kV using a working distance of 6 mm or 8 mm. Dwell times between 2.5 and 0.4 μs and a step size between 15 nm and 2 nm were used to achieve a better resolution. The smallest dwell time possible is 0.4 μs =1/2.5 MHz where 2.5 MHz is the maximum frequency of the pattern generator. The smallest step size is limited by the pattern generator and the write field size. The smalest step size is calculated by dividing the write field size by 50000 and thus for the (100 μm) write field used, the smallest step size is 100 μm /50000 = 2 nm. The dwell time and step size determine the beam speed, which should be below 4 mm/s for high resolution exposure. For 300 nm to 140 nm circles a beam speed of 15 mm/s can be used.

The write field alignment is used to compensate for feature distortion due to the beam deflection, which is a crucial step to achieve high resolution results and should be carried out before every exposure. First, a manual write field alignment should be carried out with 4 markers which should be repeated at least twice. If the change in UV coordinates is below a factor of 0.0005, an automatic write field alignment with 8 markers can be carried out.

The dual layer PMMA/MMA was exposed using a gradually increasing dose from 0.5 - 1.5 $\times$ 330μC/cm^2 vertically with an increment of 0.1, and with increasing mask size with an increment of 35 nm horizontally (see Fig 2.11). To decrease the total exposure time it is possible to expose the pattern in meander mode rather than line mode. Another option is to reduce the settling time. The settling time was reduced to 2 ms. In a pattern with a lot of separate features as in our circle matrix the settling time makes up most of

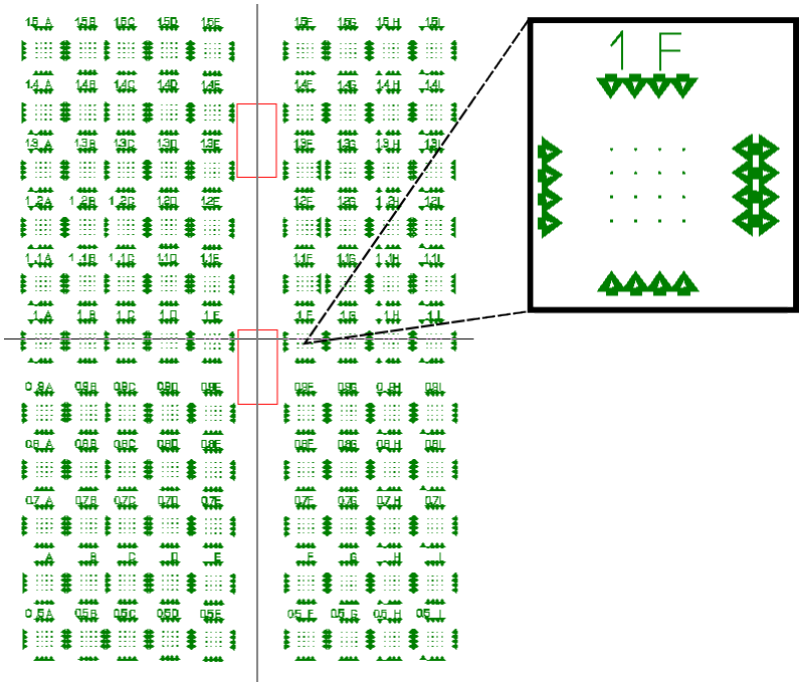

Fig. 2.11 GDSII file used to expose matrix of circular masks including markers. The dose was varied between 0.5 and 1.5 in 0.1 steps. Mask sizes varied from 350 nm diamter to 140 nm diamter in 35 nm steps from A to I.

the exposure time.

The exposed samples were developed in 1:3 (methylisobutylketon/isopropanol) buffer solution for 30 s. The 1:3 ratio of developer/buffer solution in this case gives a slower developement time, but a higher contrast. The development process was stopped by imersion in an IPA bath for 30 s. The samples were then dried using a N_2 gun. This resulted in an array of gradually increasing mask sizes ranging from 120nm - 500 nm (see Fig 2.12).

After a successful e-beam writing step in the PMMA/MMA on GaAs, the sample was cleaned in a low power oxygen plasma for 4 s before a 90 nm Ni layer was evaporated by e-beam evaporation. Fig.2.13 shows the Ni dry etching masks after the e-beam resist has been removed in an ultrasonic bath with acetone. Fig.2.13 a)-b) show a top view with circular shapes. Fig.2.13 c) shows an irregular shaped circle due to underexposure of the e-beam resist. Fig.2.13 d)-e) shows a side view at 45° of a Ni disk evaporated onto the double layer e-beam resist. The bottom layer shows a 90 nm thick Ni mask, whereas the top part ("crown") is assumed to be Ni that was evaporated onto the sidewalls of the PMMA Mask.

2.6 Reactive ion etching of GaAs and related alloys

All dry-etching was carried out on an Oxford Plasmalab 100 ICP 65 system (see Fig. 2.15). After a calibration phase, where all parameters were changed systematically to see their influence on the nanowire geometry, a two-step process was established to etch a tapered nanowire.

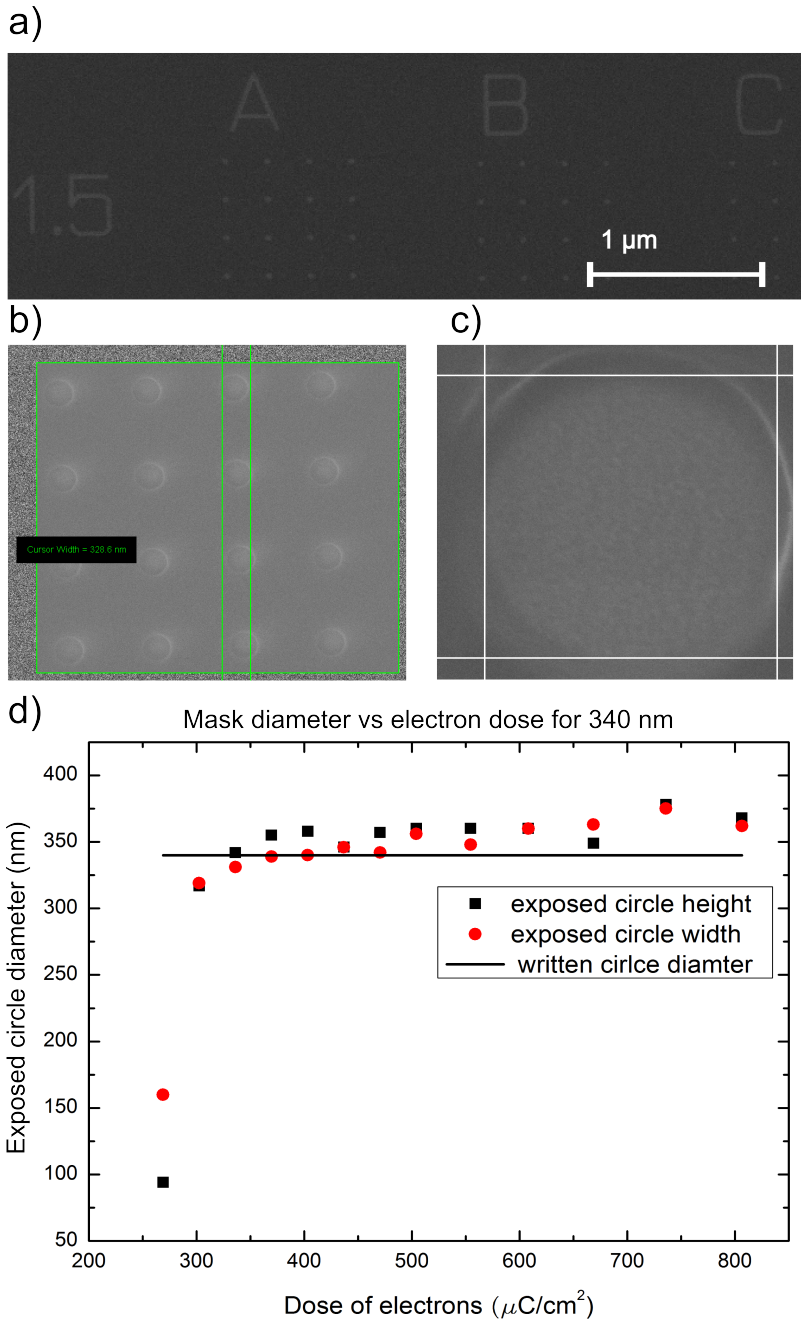

Fig. 2.12 SEM images showing that developed e-beam resist with part of the pattern and markers. a) Markers are well defined and b) - c) and are far enough apart to not show signs of proximity effects (elliptic instead of circular). d) The dose test for e-beam writing step. 340 nm circles were written with different doses. The dose recommend by the manufacturer of 330μC/cm^2 was confirmed to be the ideal dose.

The standard dry etching process is reactive ion etching (RIE) [93]. Here. a radio frequency (RF) electrode (13.56 MHz) is used to create an oscillating electric field which ionizes a gas to form a plasma, and accelerates ions towards the sample at energies >50eV and ion-densities of 10^{11} ions/cm^3 at a pressure 10 mT.

A more advanced version is the inductively coupled plasma system where the plasma is created by a time-varying magnetic fields. A ICP-RIE system is categorized as high-density-plasma etching (HDPE). In these systems, two energy sources are used; the RF

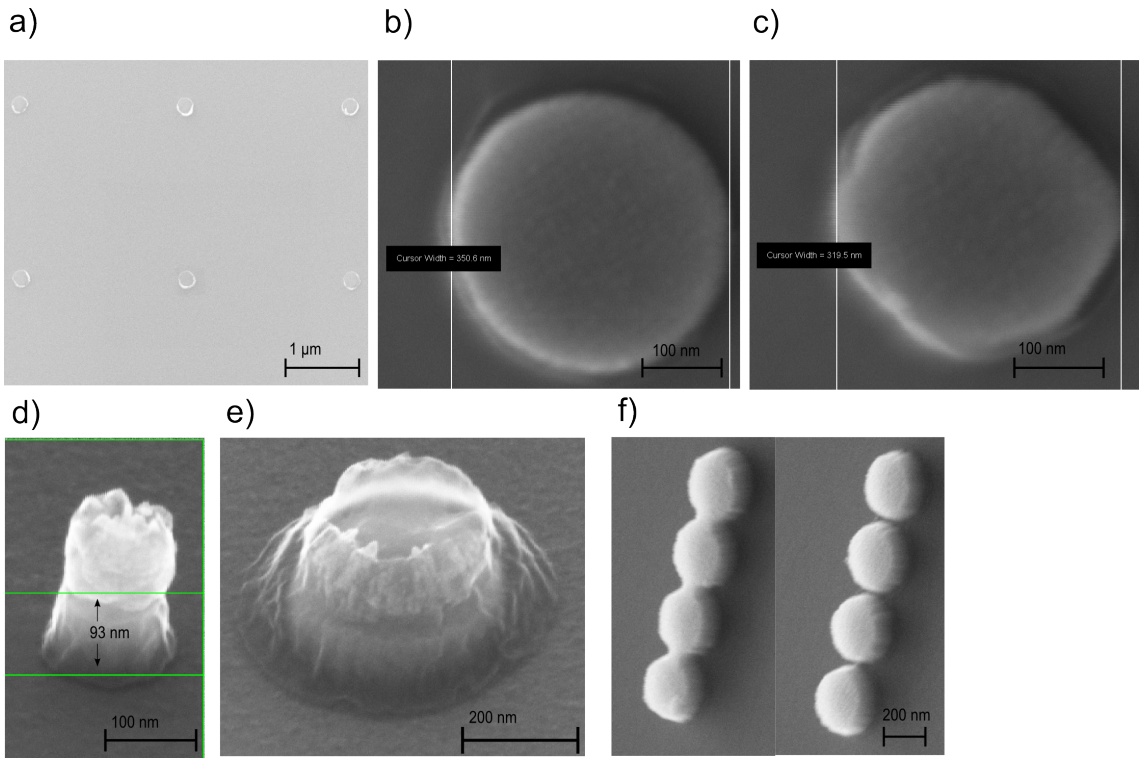

Fig. 2.13 SEM images of the Ni mask after PMMA has been removed using acetone and an ultrasonic bath at low power to not destroy the GaAs membrane. a) Array of Ni discs, b) close up of circular Ni disc, c) close up of misshaped Ni disc due to under exposure of PMMA. d) Side view at 45° of a Ni disc evaporated onto double layer resist. The bottom layer shows 90 nm thick Ni mask, whereas the top part is assumed to be Ni that was evaporated onto the sidewalls of the PMMA mask. e) a larger Ni disk. f) Left: Ni mask shows proximity effect due to overdose. Right: no proximity effect, the Ni disks are separated.

power controls the ion bombardment energy and the inductively coupled RF power (ICP) is used to generate the plasma. HDPE allows semi-independent control over the ratio of ionized and neutral species in the plasma and the sputtering energy. Bias voltages can be kept below 200 V, reducing damage, whereas the etch rate can be increased by increasing the ion density to 10^{13} ions/cm^3. This means that the same chemistry can be used in RIE and HDPE allthough there might be a loss of selectivity. For example, there is a lower selectivity for photoresists in HDPE (2-4) than in RIE (>10).

A schematic drawing of the RIE/ICP chamber used is shown in Fig. 2.14. The etch gases enter the chamber with a set flow rate using a massflow controller (see Fig. 2.15 b). The gases are heated by an alternating electric field created by RF electrodes(Fig. 2.14 e,g) and by alternating magnetic fields (Fig. 2.14 d). Only the electrons respond to the alternating electronic and magnetic fields and a fraction of the gases are dissociated into electrons and ions. The ions formed cannot respond fast enough to the changing electric field and only experience a time-averaged potential towards the powered cathode (sample holder). The energy and direction of the incident ions are determined by the DC potential which can be measured.

As a result, dry etching occurs at the sample surface and comprisis of two compo-

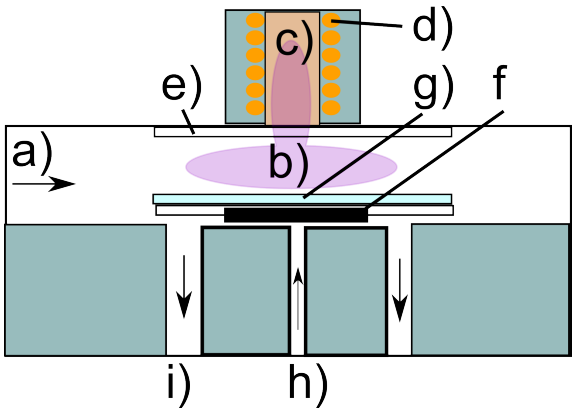

Fig. 2.14 Schematic diagram of RIE chamber a) reactant inlet, b) plasma, c) ICP tube, d) ICP coils, e) upper f) lower RF electrode and graphite sample holder,g) wafer clamp (quartz) and sample position h) inlet for He back cooling of the sample, i) outlet for used reactants and He.

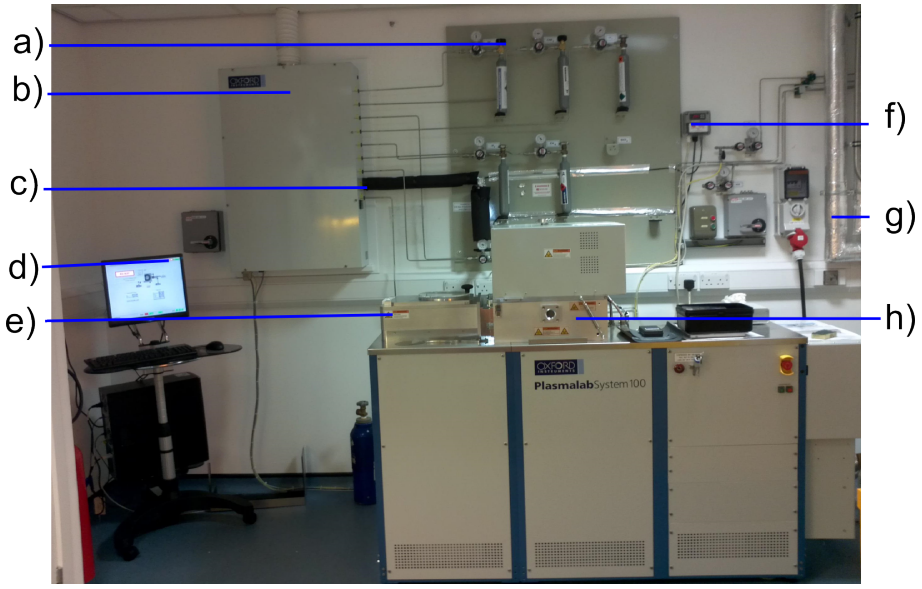

Fig. 2.15 Image of Plasmalab 100 system a) reactants, b) mass-flow control, c) $SiCl_4$ line (heated to 34° C), d) PC with control and monitor software, e) loadlock, f) heating unit for $SiCl_4$ line, g) cooling water, h) reaction chamber with view port.

nents: the chemical etch and the physical sputtering component. The chemical etch tends to introduce less surface damage, but can increase the anisotropy introducing crystallographic etching. A dry etch is preferred for mesa structures and controlled angle profiles. However, a chemical etch of 0.01 μm/min cannot be avoided at temperatures of 100 °C and 0.2 μm/min at 300 °C.

Chemical etching is accelerated by heat. High sputtering rates increase the sample temperature and therefore the isotropic chemical etch rate, thus the sample needs to be actively cooled (see Fig.2.14 h)). The sample should not be left in a Cl atmosphere after dry etching. Between alkane and halogen-based plasmas, halogen-based (F, Cl, Br, I) are more common. The most common are Cl_2 , BCl_3 and $SiCl_4$. Processes with intermediate etch rates tend to produce good surfaces. All etch recipes are guidelines and should be fine tuned on every reactor.

An example of a recipe used for etching GaAs [94] in an Oxford Plasmalab 100 ICP is shown in Tab. 2.2. Here, the $SiCl_4$ is the reactant carrying gas and Ar is used to dilute the Cl concentration and acts as a pure physical sputter component to remove reactants from the sample surface. $SiCl_4$ produces better surface morphologies, greater anisotropy, and less change in surface stoichiometry (less As loss at surface) than pure Cl_2 based etches. Nevertheless, ion implantation of Si at a DC bias of 250 V can be as high as 10^{19} cm^3 at the surface and 10^{15} cm^3 at 30 nm depth [93]. This is advantageous for n-type materials if ohmic contacts are required, but problematic for p-type materials. In the latter case, the surface needs to be etched away.

$SiCl_4$	7.5 sccm
Ar	15 sccm
Pressure	2mT (may need to be struck at >5mT)
ICP Power	150-250 W
Electrode	40-90 W(measured –120V to –175V bias)
Temperature	20 C
Backside He cooling	10 mbar

Table 2.2 Standard GaAs etch starting recipe from Oxford Instruments for Plasmalab 100.

Reactive Ion Etching is a process where results are influenced by many parameters. Even though greatest care was taken to keep most parameters constant, such as physical-chemical cleaning of the chamber and preconditioning, redeposition on the walls over time and previous materials/reactants used in the reaction chamber changed the results of the same etch recipe from batch to batch. In most cases, the etch recipes are slightly changed to reproduce the same results. Despite the change of behavior over time of the reaction chamber some trends have been observed.

To keep the sample temperature and therefore etch rate constant and anisotropic, Fomblin vacuum pump oil was used to adhere the samples to the sample holder. This prevented the samples from flipping over and is common practice to ensure thermal conductivity between the sample holder and the sample. Graphite plates were used as sample

holders. Graphite is chemically inert, has a high thermal conductivity and allows for a stable sample temperature during etching. Helium Backside cooling was used to create a thermal contact between the sample holder and the chamber was held constant at 20 °C using a closed cycle glycol chiller. Reducing the table temperature reduced the etch rate, but did not improve the Ni/GaAs selectivity, and therefore did not improve the taper angle. Without He backside cooling, an exponential increase of the etch rate with time was observed. With He backside cooling, the etch rate did not increase with time (see Fig.2.16).

He backside cooling visibly increased the selectivity between photoresist and GaAs. The He flow varied between 1.3 and 6 sccm depending on the He pressure and graphite plate used. The same sample holder was used to keep the He flow constant between samples. The amount of He backcooling is limited because 6 sccm of He flow would be a significant contribution to the chamber pressure. To achieve low pressures of 2 mT, the recommended amount of $SiCl_4$/Ar flow in the etch recipe had to be reduced.

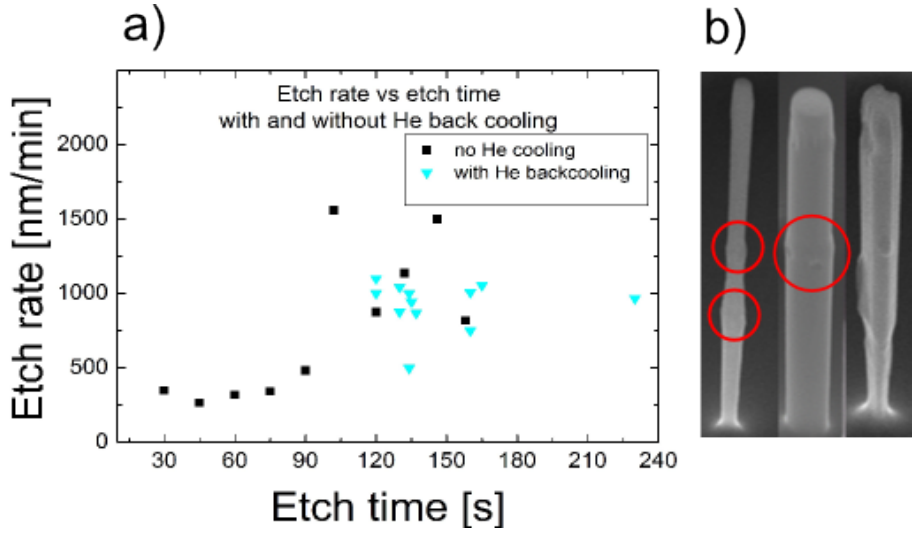

Fig. 2.16 a) The increase in etch rate with time without He backside cooling. Using He backside cooling the etch rate appears to be constant within a certain tolerance which is caused by irregular thermal conductivity of the sample and the sample holder and different sample holders used. b) bulges in the nanowire occur when He backside cooling is interupted, indicated by red circles. If He backside cooling is not used, selective etching of the crystal planes can occur depending on the etch recipe used.

When changing the chamber pressure from 2 to 12 mT for constant etch time of 150 s using recipe j) table 2.3, it can be observed that the etch rate increases (see Fig2.18 a-f). A cone is formed at 2 mT. At a chamber pressure of 3.7 mT a cone with a lower angle at the top is formed but an inverted taper at the bottom. This inverted taper seems to occur at higher pressures as well. The top taper angle narrows and at even higher pressures an elongated inverted taper forms, by changing the RF power (Fig2.18 g-i) it was observed that at low RF powers an inverted taper forms and at higher RF powers the bottom of the pillar is straight. This is due to the increase in DC bias which reduces the angle with which the reactive ions are accelerated towards the substrate. We can as well see that with

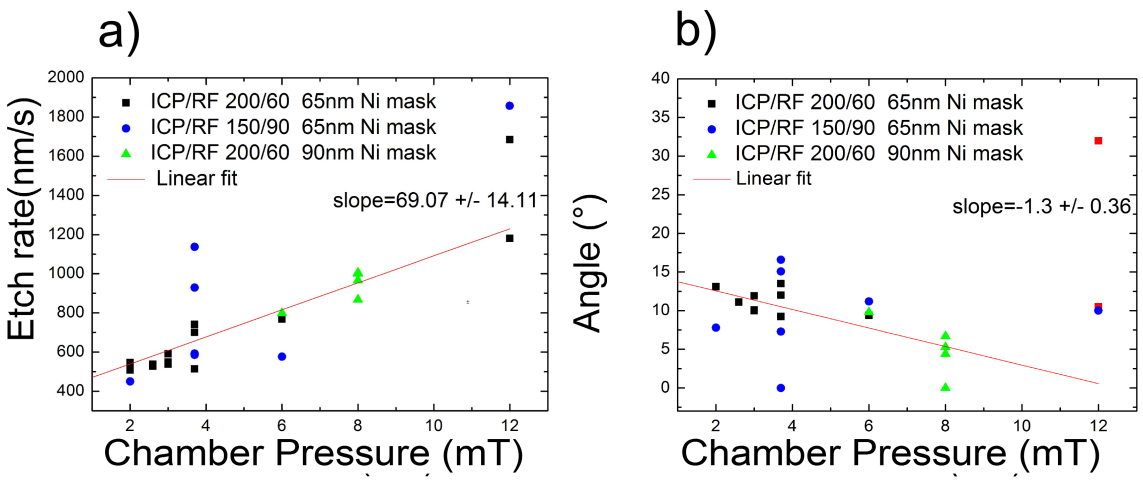

Fig. 2.17 Showing a) the change in etch rate (nm/s) vs chamber pressure. b) The change in taper angle α in (°) with chamber pressure. Both plots include data with different Ni mask thickneses and different RF power ratios. From b) it can be seen that the low angles at high power can only be achived with a thicker Ni mask.

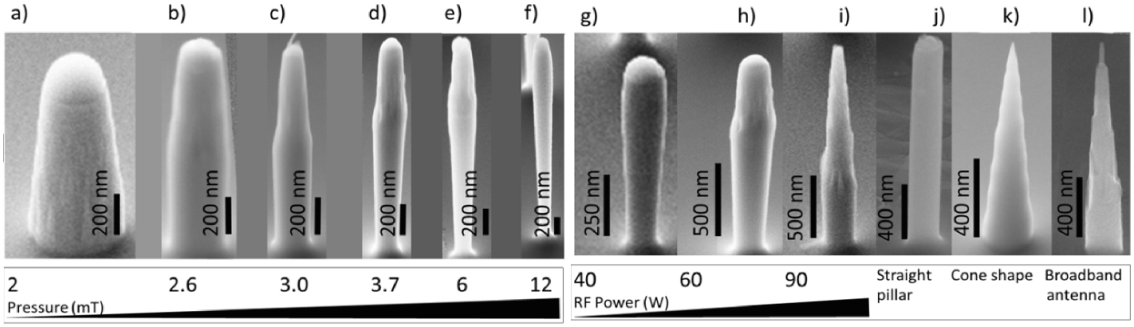

Fig. 2.18 SEM images showing the influence of dry etch parameters on the nanowire shape. a) - f) Pressure, with increasing pressure the top taper narrows, at P = 2.6 mT the sidewalls at the bottom of the wire are straight and at higher pressures an inverted taper forms.g) - i) increasing the RF power results in the formation of a top taper and the inverted taper at the bottom disapears.j) Straight pillar, k) cone shaped pillar, l) broadband antenna.

increased RF power a sharper tip forms.

Straight GaAs pillars (Fig.2.18 j) were etched using recipe j) table 2.3. The Ni dry etch mask used with d = 90 nm was found to be sufficient for straight pillar formation with an aspect ratio of up to 1:18. A higher pressure and higher ICP power increased the etch rate. The RF power of 60 W was chosen to reduce the formation of an inverted taper and to inhibit a top taper formation.

To create a conical pillar as shown in Fig.2.18 k) the Ni Mask was undercut and etched away by increasing the RF power, reducing ICP power and lowering the pressure, so the Chemical horizontal isotropic etch increased in comparison to the vertical anisotropic etch (see Tab.2.3 k). To have more control over the horizontal etch, the $SiCl_4$/Ar ratio was reduced from 1:2 to 1:3. Reducing the $SiCl_4$/Ar ratio and therefore reducing the chemical reactants leads to a higher physical etch and therefore a lower selectivity for the GaAs, resulting in higher mask erosion. The taper angles achieved was approximately 15°.

To fabricate the high efficiency nanowire required a two-step etch process, consisting of a recipe for a straight etch (Tab. 2.3 col. (j)) followed by a recipe for conical pillar (controlled undercut of the mask) (Tab. 2.3 col. (k)). First the straight bottom part was etched using the straight pillar recipe (30 s) and then the taper (225 s) using the conical pillar recipe. Introducing an additional high pressure etch at the end improved the taper angle but increased surface roughness. Taper angles as low as 3° have been produced using the recipe for the straight pillar, but it was not possible to reproduce these results consistently. To remove the remaining Ni and clean the taper from redeposited material, the sample was immersed in dilute nitric acid (1:10 $HNO_3 : H_2O$ for 90 s) [95]. After 120s the acid treatment improved the taper angle by up to 2°. The two step etching sequence and the nitric acid treatment resulted in the desired structure of the high efficiency nanowire antenna (Fig.2.18 l)) with taper angles between 7.7° and 10 °.

Parameter @ 20°C	Straight (j)	Cone (k)
RF power	60 W	90 W
ICP power	200 W	150 W
Pressure (P)	8 mT	2.7 mT
$SiCl_4$/Ar ratio	7.5/15 sccm	4/12 sccm
He flow	2.2 sccm	2.2 sccm
DC Bias	390 V	500 V
Etch rate	750 nm/min	480 nm/min

Table 2.3 Etch parameters for straight (j) and cone shaped (k) wires.

2.7 Conclusion

The photonic nanowire discussed in section 1.3.2.2 was successfully fabricated with the following recipe. First an electron beam evaporation step was used to create a Au mirror that also acted as a thermocompression bonding layer. The Au layer was characterized by SEM and consisted of 20 - 30 nm clusters. Thermocompression bonding was carried out in a home built wafer bonder. The membrane containing the QDs was removed from the growth wafer using HCl in an ice bath. The HCl etch step could be further optimised to reduce redeposition of reactants on the membrane surface which lead to micromasking in the dry etching step. E-beam lithography was then used to define Ni dry etch masks of 120 nm ato 500 nm diameter. A two step dry etching procedure was developed to etch the nanowire with height 2 μm, taper angles between 7.7° and 10° and diameters ranging from 120 nm to 500 nm. The surface roughness of the nanowire was determined to be the same as the Ni mask surface roughness. To achieve narrower taper angles and a lower surface roughness it is proposed to use a smoother dry etch mask. The experimental setup, and characterization of the optical properties and strain-tunability of the fabricated nanowire are discussed in the following chapters.

Chapter 3

Cryogenic optical spectroscopy

Performing photoluminescence measurements on QD's in a nanowire presents an experimental challenge. A set-up must be constructed that allows for low temperature experiments to be carried out in combination with imaging of the sample surface. High microscope resolution must be combined with high collection efficiency and excellent long term system stability. The following sections describe the experimental set-up. The confocal microscopes, spectrometer, time correlated single photon counting (TCSPC) setup and cryogenic equipment (see section 3.2) used to carry out low temperature spectroscopy are discussed. Three confocal microscopes were built for different projects during this thesis, two room temperature confocal microscopes heads (see section 3.1.1) and a miniature low temperature microscope (see section 3.1.2). One home built cryostat (see section 3.2.2) and two commercial turnkey cryostats (see section 3.2.1) were assembled and installed, respectively. Hfigh photon collection efficiency and stability and adaptability of the experimental system were a priority during design.

3.1 Confocal microscopy

To isolate a single nano-pillar with a diameter of 200-400 nm, a diffraction limited confocal microscope is essential. A simultaneous requirement is to maximize the collection efficiency from a single dot. This is important to achieve good signal to noise ratios which lead to shorter acquisition times and provide higher quality data [26]. Ultimately this efficiency will also impact on practical applications. Furthermore the system must operate at low (4 K) temperatures with long term stability. High precision nanometer movement is required to bring a single nanowire into focus. To deterministically study single nanowires, imaging of the sample should allow one to distinguish individual wires and their coordinates on the sample. The microscope should allow for future alterations that may be essential to change the experiments.

A confocal microscope uses the same objective lens for excitation and collection [96]. It operates on the principal that a small aperture can be used to prevent collection of all off-axis and out of focus light. This is achieved through point illumination and point

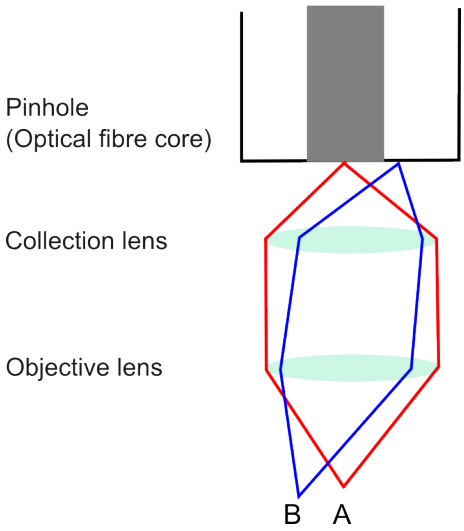

Fig. 3.1 Schematic diagram of the confocal microscope principle. Light from point A is in focus and is directed into a fibre. Light from point B will not be collected by the fibre.

collection of the light [26, 96]. Light from the sample is collected by an objective lens and focused onto a fibre via a collection lens (see Fig 3.1). The fibre core acts as a pinhole and prevents light from point B to enter the fibre while light from point A is collected [26, 97]. Out of focus light is also prevented from reaching the fibre core (not shown in diagram).

A confocal microscope provides the highest resolution obtainable from conventional optics as only light from the exact focus of the objective lens is imaged, and in the ideal case the system's spatial resolution is limited by diffraction. The spot size ΔX, which is the full width at half maximum (FWHM) of the Airy function can be approximated by using the Sparrow criterion (see eqn.3.1).

$$\Delta X = \frac{0.52\lambda}{NA_{objective} n_{med}} \tag{3.1}$$

where $NA_{objective}$ is the numerical aperture of the objective lens, n_{med} is the refractive index of the host material and λ the wavelength of light in vacuum [98]. From the equation, it is obvious that a higher NA will have a smaller focus. A higher NA also has a higher collection efficiency (see section 1.3.2.2 Fig. 1.13) and as a result a better signal to noise ratio [96]. The three confocal microscopes that have been built and characterized are listed in table 3.1.

Microscopes	
miniature	To be used in future experiments
1300 nm	Used by L.Sapienza *et.al* [20]
950 nm	Used for results in chapter 4

Table 3.1 An overview of the confocal microscopes built and characterized in this thesis.

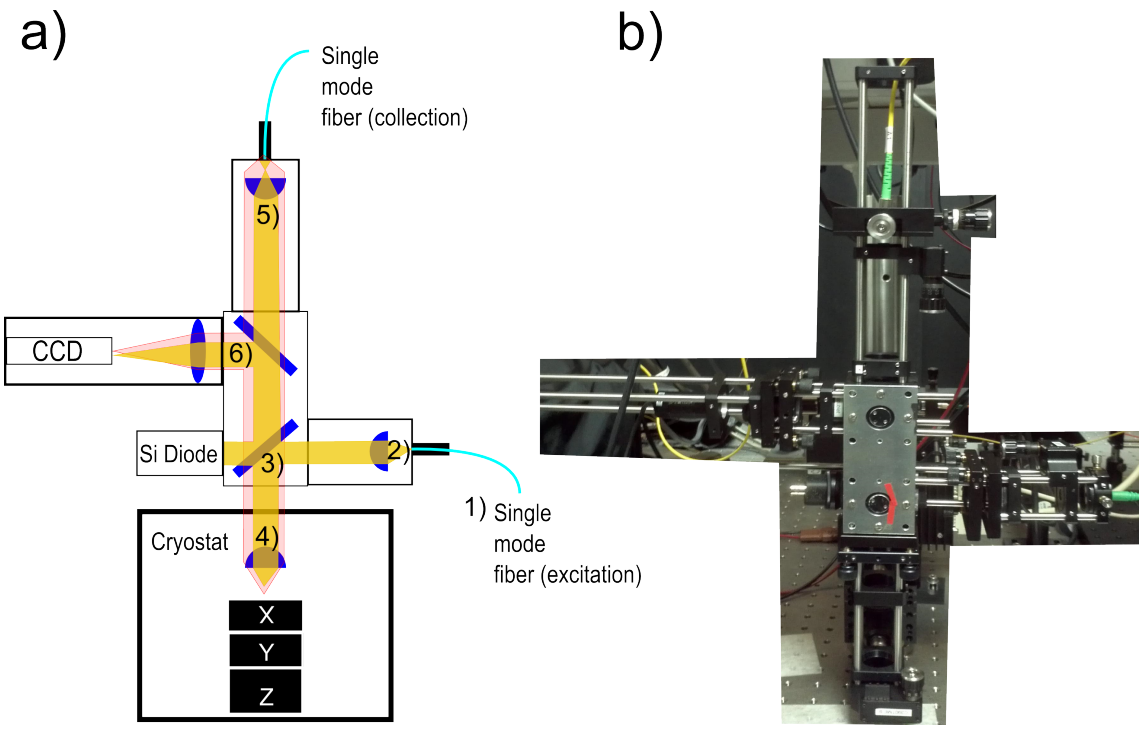

Fig. 3.2 a) Schematic diagram of the confocal microscope head used for low temperature QD studies. 1) fibre coupled excitation laser, 2) excitation arm with collimation lens, 3) 1st beam splitter, 4) objective lens, 5) collection arm with fib coupling optics, 6) 2nd beam splitter for imaging and achromatic doublet lens. b) photograph of confocal microscope head.

3.1.1 Room temperature confocal microscopes heads for operation at 950 nm and 1300 nm

Two room temperature microscope heads were built to guide excitation light to the sample and collect photoluminescence at λ_{col} = 950 nm and λ_{col} = 1300 nm. Collimated laser light and stage scanning simplifies the optical setup [96]. The microscopes are optimized for non-resonant excitation at λ_{exc} = 830 nm. The excitation laser and the spectrometer are connected by single mode optical fibres to the microscope head, which allows for adaptability of the setup. The system is build using Thorlabs parts. The pinhole of the confocal microscope is provided by the optical fibre (980 HP) of the collection arm and has a diameter $d_{fibrecore}$ = 3.6 μm. The microscope head is mounted on the microscope tube, which is inside the cryostat (see Fig.3.2 a). The microscope head is at room temperature which allows continuous adjustments during experiments. Both microscopes are designed to allow maximum transmission for the PL signal to the collection arm. This has been achieved by using anti-reflection coatings on all lenses for the desired wavelength (see Table 3.2).

The excitation light from a 830 nm CW laser is fibre coupled and guided to the excitation arm of the microscope head using a single mode optical fibre for 830 nm (see Fig.3.2 a). The fibre coupling allows for the source to be changed to a pulsed laser diode for lifetime measurements without interfering with optical alignment of the microscope head (see sec-

Confocal microscope parts	950 nm	1300 nm
Collection lens	C280TME-B	C280TME-C
Imaging lens	AC254-100-B	AC254-075-C
Beam splitter	BK7 (5mm)	BK7 (5mm)
Excitation lens	C280TME-B	C280TME-B
CCD camera	finger camera (conrad el. 191133)	contour IR (oelabs)
Si diode (power meter)	SM1PD1A Si	SM1PD1A Si
Objective lens	LT-APO/vis/(0.82NA)	C330TME-C (0.68 NA)

Table 3.2 The optical parts used to build the λ = 950 nm and λ =1300 nm confocal microscope head.

tion 3.3.2). The fibre coupling also allows for the excitation power to be attenuated with absorptive neutral density (ND) filters (see Fig.3.14).

At the microscope head, the excitation light is collimated using an aspheric lens (see tab.3.2 excitation lens) and directed to the first beam splitter consisting of a 5 mm thick BK7 glass tilted at 45°.

At the beam splitter, 4% of the excitation power is reflected downwards at each glass-air interface towards the sample and 92% is transmitted to a photo diode to measure the excitation power. The light reflected at the first glass-air interface is is directed towards the sample. The light reflected towards the sample at the second glass air interface forms a "ghost spot" 4 mm away from the real spot, which is blocked by the cage plate of the objective lens which acts as an aperture. Reducing these unwanted reflections is necessary to simplify alignment.

The objective focuses the excitation light onto the sample and collects the PL signal. To achieve a high collection efficiency, a lens with a high NA was chosen. Due to the many cooling cycles to cryogenic temperatures, the choice of materials and therefore the NA of the lens is limited. For the 950 nm head, a novel objective compound lens from attocube (LT-APO/VIS/0.82) has been used with a NA = 0.82 and a working distance w = 0.35 mm.

The PL signal collected by the objective lens is collimated and passes through a BK7 glass window and two beam splitters before it reaches the collection arm, where it is focused onto a 99:1 fibre beam splitter. The fibre splitter guides the PL signal to the spectrometer. At the same time, it allows laser light through the 1% arm from a resonant laser (λ =950 nm) to enter the microscope for alignment purposes without having to detach fibres at the the head or the spectrometer itself.

At the second beam splitter, 4% of the light is directed towards a CCD camera which uses an achromatic doublet lens (see tab.3.2) to project an image of the focal spot. This image is used for alignment purposes. The same lens and camera are used for white light imaging of the sample surface which is described in the next section.

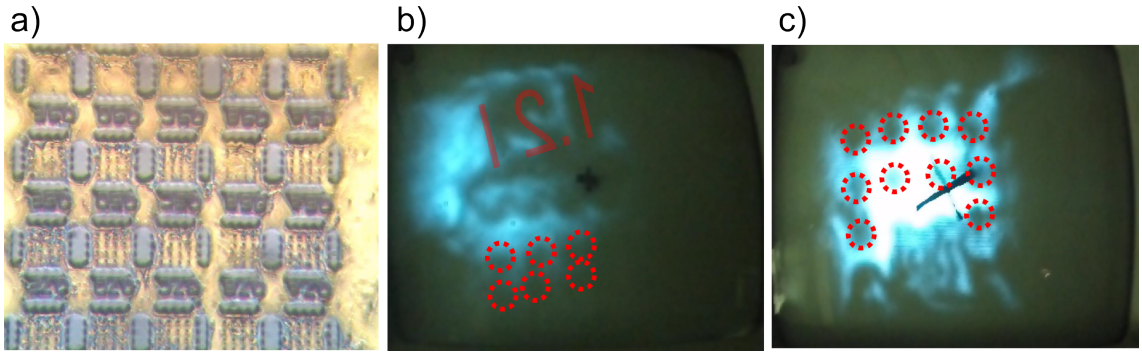

Fig. 3.3 a) Sample image using optical microscope showing GaAs pillars, markers and the Au mirror. b)-c) Snapshot from CRT monitor showing the sample at 4K inside cryostat. The image is a mirror image of the marker and 16 pillars. The cross hair was placed at focal point of 950 nm alignment laser.

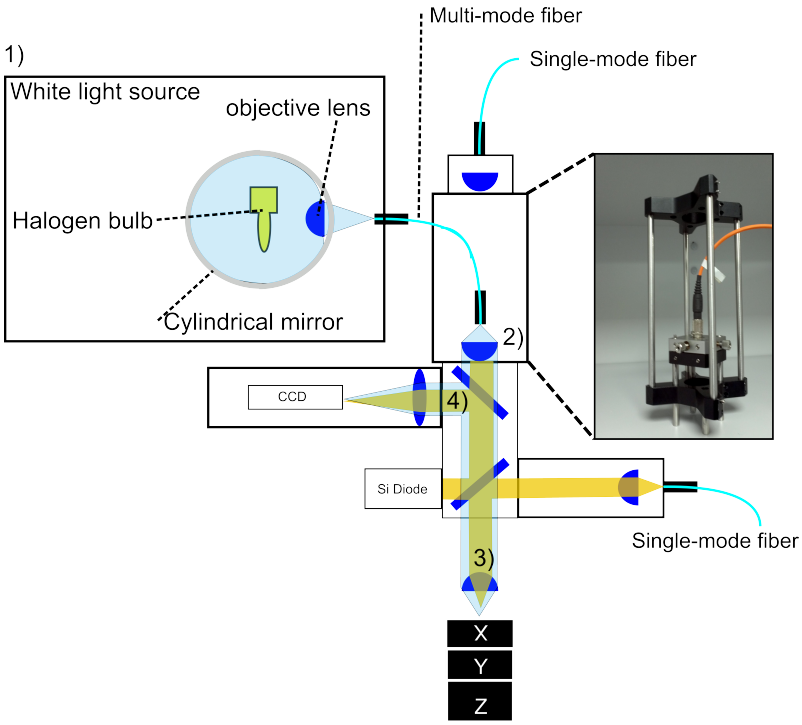

Fig. 3.4 Schematic of the confocal microscope head in imaging mode showing 1) white light source, 2) outcoupling lens, 3) objective lens, 4) imaging lens with CCD camera. Inset : photograph of removable outcoupling end of white light source.

3.1.1.1 White light imaging of the sample surface at 4K

The samples investigated comprised a set of nanowires arranged in a matrix with different diameters Fig.3.3 a). The set of one diameter contained 16 nanowires marked with arrows and a code for each diameter (see Fig.3.3 b). To image the sample surface, and the nanowires and markers etched into the GaAs membrane, the "950 nm" confocal microscope was equipped with a fibre coupled white light source to illuminate the sample as in (Fig.3.4). The CCD camera already mounted on the head, which serves as an alignment tool, was used to image the sample.

Imaging of the sample surface allows to deterministic investigation of nanowires. Furthermore, it allows the correlation of the nanowires physical dimensions, e.g. diameter and taper angle, from SEM images with the PL signal. This enables conclusions about nanowire dimensions influencing the optical performance. For reflection mode imaging, a coherent broadband light source is preferred which does not cause interference from different layers which can alter the image of the sample, even in the presence of axial chromatic aberration [96]. The working principle is shown in Fig. 3.4 and explained in detail below.

The most suitable solution, was found to be a Halogen bulb coupled to a multimode fibre using a (NA = 0.25 WD =10.6 mm) objective lens mounted to a z translator (SM1Z). For alignment in the xy plane, the multimode fibre was attached to a xy stage (ST1XY-D/M). The outcoupling end of the multimode fibre was mounted to a xy-flexure translation mount (CP1XY). The xy stage was used to move the fibre relative to the aspheric lens (A220TM NA = 0.26, f = 11 mm), and align the beam of light with the objective lens at the bottom of the microscope tube. The aspheric lens to fibre distance was adjusted using the thread inside a cage plate, so that a spot with the size similar to the objective lens diameter at approximately 1.5 m away was formed. The outcoupling optics of the multimode fibre were housed in a 30-60 mm cage plate adapter (LCPO2/M). This allowed for the out coupling optics to be removed without disturbing alignment of the head and switching between imaging and confocal microscopy mode.

The white light reflected at the sample surface passes back through objective lens and up through the microscope head. The sample stage z-motors were used to bring the sample into focus.

At the second beam splitter, 4% of the light is reflected towards the imaging arm. An achromatic doublet lens (AC508-100-B-ML, f = 100 mm) was used as the imaging lens which projects an image onto the moveable CCD camera. By changing the CCD to imaging lens distance and the sample to objective lens distance, it was possible to focus and magnify the image appropriately. The magnification of the microscope is determined by the magnification of the objective lens and the imaging lens. The total magnification was measured by calculating the size of a projected feature on the CCD and comparing it with the real dimensions on the sample. The real distance between 4 pillars on the sample is 7.5 μm. The same length occupies 1.615 μm on the CCD sensor, giving an optical

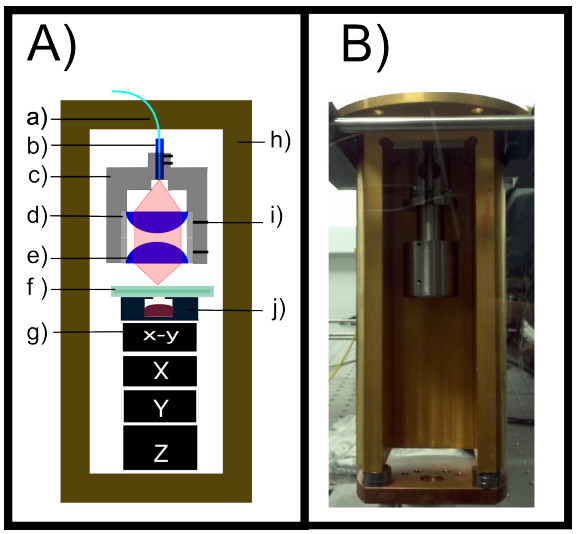

Fig. 3.5 A) miniature confocal microscope setup a) optical fibre, b) ceramic fibre ferrule, c) titanium lens tube, d) collimation lens, e) objective lens, f) sample, g) (x-y) scanner and x,y,z step motors, h) monolithic copper housing, i) grubbscrew, j) button with Si photodiode. B) photograph of real device (x,y,z nanopositioners not shown).

magnification of approximately 200. This magnification is sufficient to deterministically choose a single nanowire using the focal spot of the excitation laser. In addition, a marker on the monitor was used to mark the position of the collection spot (see Fig.3.3 c).

3.1.2 Miniature low temperature confocal microscope

The miniature microscope is a compact confocal microscope constructed to be cooled down to < 4 K (see Fig.3.5). Only an optical fibre connects the microscope between the low temperature part inside the cryostat and room temperature on the outside of the cryostat. The optical design allows for a much higher collection efficiency due to a reduced number of air/glass interfaces. The miniaturization of such an optical two lens system placed together with the sample and its positioning system in a monolithic housing was described by A. Hoegele, whose report was used as the basis of the optical design [97] .

3.1.2.1 Requirements

A useful and cost effective tool for scientific research is a single cryostat (see section 3.2.2) allowing both PL measurements of quantum dots and the use of superconducting nanowire single-photon detectors (SNSPDs) [99]. For PL measurements of QD's a confocal microscope is commonly used. Ideally, this would be a fibre based confocal microscope for cryogenic operation which provides precise and reliable sample scanning and high mechanical stability with negligible drift over many days of operation (see section 3.1.2.4). The objective should have a high numerical aperture (NA) operating at the diffraction limit and sample scanning should be possible with nanometre precision over a millimeter range even at low temperatures. In a drift free system, the focal spot should move by less than 100 nm so that continuous alignment is not required. Titanium, due

to its low relative displacement and mechanical deformation, provides low drift when temperature is changed or magnetic fields are introduced. Titanium was used for the fabrication of the microscope and Au coated oxygen free copper for a monolithic housing (see Fig. 3.5 B). A compact design with close spacing between sample, objective lens and collimation lens is desired to minimize vibrations. A single glass fibre serves as an optical guide for both excitation and collection from the sample. The fibre provides the connection between the low temperature environment and the rest of the experiment at room temperature. The single mode fibre plays the same role as the pinhole [100] in a conventional confocal microscope [101].

The pulsed tube cryostat used works without He exchange gas in a high vacuum for optimal operation. All heat is conducted away by the oxygen free Cu which was chosen for its high thermal conductivity. Cu ribbons are commercially available (attocube Thermal Coupling Device: ATC100) to improve the heat transfer from the sample to the cold head.

3.1.2.2 Optical design

The optical design consist of a Geltech aspheric collimator lens (C220TME-B) with NA of 0.25, f = 11 mm, and a clear aperture of 5.5 mm. The objective lens (C330TEM-B) has an NA = 0.68, focal length f = 3.1 mm, and a clear aperture of 5 mm. The core of the single mode fibre (Thorlabs 980 HP NA = 0.20) with a diameter of 3.6 μm acts as a pinhole. The boundary conditions for the choice of the collimation lens were first to match the NA to that of the optical fibre. The collimation lens yields a clear aperture of 4.49 mm which in turn results in an effective NA of our objective of NA = 0.58. Using equation 3.1 (in section 3.1) a theoretical spot size of 818 nm is obtained.

Due to the compact design of the microscope, commercial single mode FC/APC optic patch cables could not be used. A single mode fibre for 950 nm was cleaved by hand and glued into a suitable ceramic ferrule using optical UV-curing adhesive (Thorlabs NOA63). The fibre was chosen for its single mode operation at 950 nm (λ = 980-1600 nm), suitable NA, and most importantly smallest long term bending radius available of 13 mm). The smaller bending radius allowed the microscope to be as short as possible to reduce vibrations. The end of the fibre was hand polished using a Thorlabs polishing kit (CK03 - FC/PC Termination / Connectorization Tool Kit). The other end of the fibre was hand polished with the same procedure but using a commercial FC/PC connector.

To optimize the system for maximum collection efficiency, a resonant 950 nm laser was used for the alignment. The higher loss for an 830 nm excitation is not relevant. The resonant laser was fibre coupled to a 99:1 fibre splitter. The 99% arm was used to couple the laser light to a 2nd set of fibre coupling optics. Here the light was collimated and focused onto the hand polished FC PC connector with only 20 % less coupling efficiency compared to a commercially polished fibre.

The lenses were mounted in titanium lens mounts fabricated at Heriot Watt (see

Fig.3.5A).The lens tubes were fixed and the fibre ferrule was adjusted for optimum collimation along a distance of 1.5 m. The transmission from the ferrule to the sample was found to be approximately 80%.

3.1.2.3 Determination of the focal plane and spatial resolution

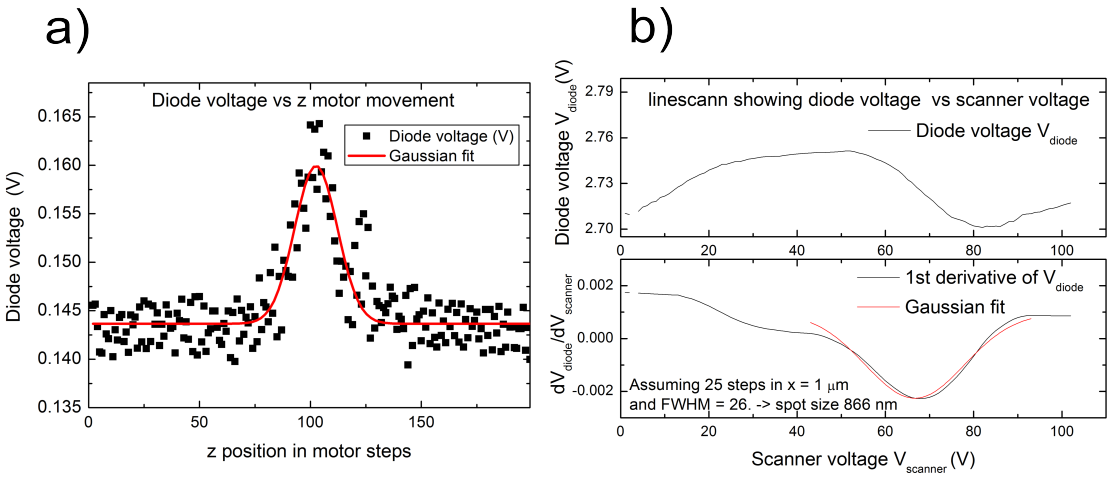

Fig. 3.6 a) Scatter plot of the photodiode voltage as a function of z motor steps. When the sample is in focus the highest power is transmitted. b) Top graph shows a line scan of a checkerboard sample. Bottom graph shows the the derivative dVwith a Gaussian function (FWHM = 26 V) fitted to the peak. The calibration for the scanner Voltage to distance is 25 V/1 μm.

In the larger heads that operate at room temperature (section 3.1.1), the focal plane is determined by imaging the focused laser reflected from the sample surface on a CCD camera. The miniature microscope does not have this option. To determine the focal plane one can measure the change in transmitted and reflected powers as the sample scans through the focal plane. A photodiode (Thorlabs FDS100) was mounted beneath a sample to measure the transmitted power. The coarse adjustment of the focus was carried out by eye, with the knowledge of the working distance of the objective lens. The sample was moved through the focus, away from the objective lens, using the Z nanopositioner (ANP_Z101). A piezo step controller (ANC 300) with an ANM 150 module was used to control the nanopositioners. The ANC 300 was connected via a USB cable to a PC. A Python code was used to send step signals to move the Z motor up and down and record values of transmitted power as a function of steps using the voltage values of the photodiode.The motor step number was plotted vs the transmitted power. Fig.3.6 shows a maximum of transmitted light at 100 steps from the start point.

After the sample was moved to the point of highest transmission, the spatial resolution of the microscope was determined using a checker-board with 10 μm periodicity (Cr on glass) and the same photodiode as above to measure the transmission. The transmission through the checker-board is given by a convolution of the Gaussian focal intensity distribution with the transmission function of the checker-board. The edges of the squares

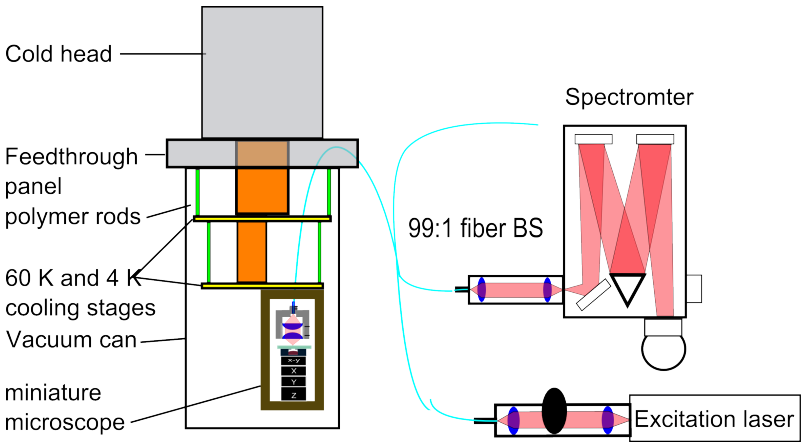

Fig. 3.7 Proposed setup for PL measurements using a home built cryostat which is designed to house single nanowire detectors at the same time as a confocal miniature microscope. The sketch shows a simplified cryostat setup, optical fibre beam splitter used to connect the low temperature inside to the room temperature outside, with connected excitation laser and spectrometer for sample characterization.

compared to the focal spot diameter are sharp and the transmitted power is determined by the Gaussian error function [97]. The FWHM of the corresponding derivative dT/dx is equal to the focal spot size. A transmission map of the checkerboard was recorded using an attocube compact open loop xy-scanner (ANSxy100/std) controlled by a ANC200 piezo scann controller and a python code. The same code was used to record the transmission as a function of xy piezo voltage using a Keithley multimeter. A line scan is shown in Fig.3.6 b). The first derivative of a horizontal line scan of the 2D map orthogonal to the checkerboard squares was is plotted below. A Lorentzian curve at the transition between transparent glass and opaque chrome mask was fitted. The FWHM of the derivative was taken as the focal spot size, which was found to be 866 nm. The theoretical spot size at the diffraction limit was calculated to be 818 nm.

3.1.2.4 Proposed spectroscopy setup

The microscope is placed into the pulsed tube cryostat and the out coupling end is connected using a fibre connector to a fibre connecting the low temperature inside of the cryostat directly to the room temperature on the outside of the cryostat (see Fig. 3.7). Here the fibre end is connected to a 99:1 fibre splitter. The 99 % arm is coupled to a spectrometer. The 1 % arm is coupled to a 830 nm excitation laser.

3.2 Cryogenics: Pulsed-Tube Refrigerators

Fundamental research in physics often requires the use of low or variable temperatures. Many phenomena also involve the application of high magnetic fields, usually generated by superconducting magnets. Previously, liquid helium baths have been used to reach temperatures of 4 K. Due to the heavy logistics, insecure supplies and steadily increasing

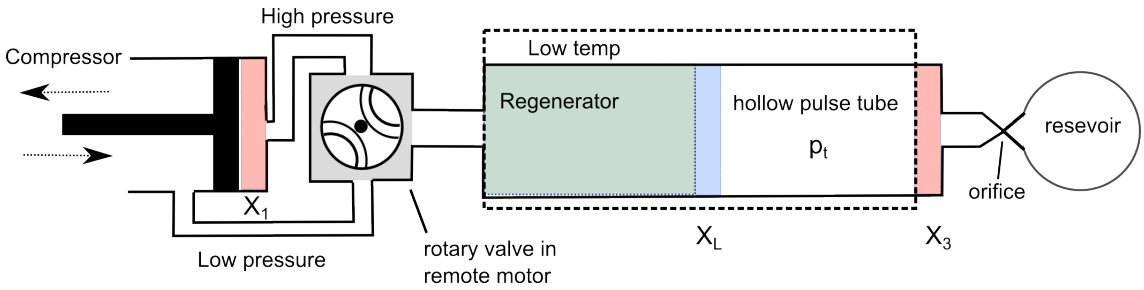

Fig. 3.8 Schematic diagram of a pulsed tube cryostat with sketch of compressor, high/low-pressure He-flex lines, remote motor with rotary valve, regenerator, thermally isolated pulse tube, orifice, reservoir. Heat exchange point are red(hot) and blue(cold). The area between the heat regenerator and X_3 (in doted lines) is below room temperature and in vacuum.

price of liquid helium, pulsed tube cryostats have become more viable for research applications and do not consume liquid helium. Pulsed tube refrigerators (PTR) make use of a closed He cycle [102] and can be made without moving parts and electro-magnetic interferences in the low temperature part. They are therefore ideal for high precision measurements. PTRs have first been proposed by W. E. Gifford and R. C. Longsworth in 1960's and were first built in 1984 by Mikulin, reaching temperatures of 105 K.

In a PTR the compression is achieved with a remote compressor as shown in Fig.3.8. As the gas is compressed the generated heat is conducted away to cooling water at the first heat exchanger X_1. The compressor delivers constant pressure which is guided to a remote motor through a high pressure He-flex line. The remote motor is separated by a He-flex line from the cold head to reduce vibrations and noise in the cold head. The rotary valve in the remote motor alternatively lets high pressure gas into the cold head or removes high pressure gas and guides it back through a low pressure He-flex line to the compressor. The operation frequency is 1 to 2 Hz for lower temperatures (below 20 K) which results in a smooth pressure variation in the pulse tube and no acoustic effects such as traveling pressure waves or fast pressure changes [103].

The high pressure gas enters the hot end of the regenerator. The regenerator is filled with a porous material and is connected to the cold end of the hollow pulse tube. In a U shaped cooler the regenerator encloses the pulse tube and pre-cools the high pressure gas before it passes the cold end X_L. In the regenerator and in the heat exchanger the heat contact between the gas and its surrounding material is good, and the temperature T_a of the gas is practically the same as that of the surrounding medium. The function of the pulse tube is to separate the warm end X_3 and the cold end X_L [102, 103]. Therefore the tube has to be large enough that the gas travels only a part of the tube length. Minimizing turbulence inside the pulse tube is crucial for the operation of the PTR [102]. The gas in the pulse tube is thermally isolated and the temperature varies with pressure. The gas inside the hollow pulse tube is separated into three parts (see Fig. 3.9); (i) The gas in the middle of the pulse tube forms an insulating barrier between the cold end and the warm end because it never leaves the pulse tube. (ii) The gas at the cold end moves in and out

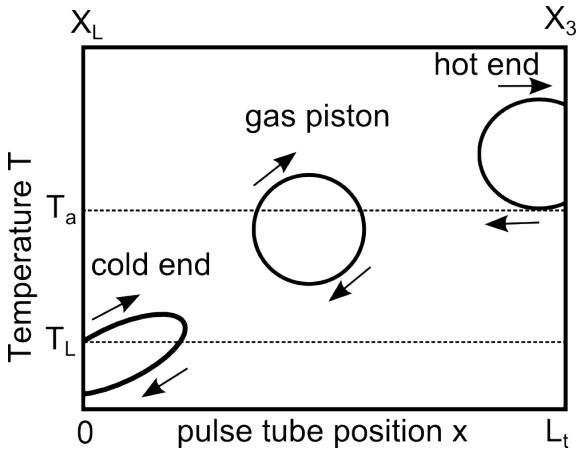

Fig. 3.9 A schematic diagram showing the temperature variations of the gas with respect to the pulse tube position as the pressure oscillates. At the cold end gas enters with temperature T_L and leaves at a lower temperature. The gas piston does not leave the pulse tube, it moves to the right with high T and to the left with low T. At the hot end gas enters with temperature T_a and leaves at a higher temperature.

via the heat exchanger X_L and (iii) gas at the warm end moves in and out of the heat exchanger X_3. Together they form a "gas piston" [103].

During the compression process the gas flows from right to left. The gas enters the regenerator with temperature T_a and leaves the regenerator with T_L[103]. The regenerator takes out, and stores heat from the gas while flowing through the porous material [103]. At the cold end X_L gas flows from the regenerator with temperature T_L into the pulse tube. At the warm end of the pulse tube X_3 the compressed hot gas flows through an orifice into a reservoir volume. The gas leaves with a higher temperature then the inlet temperature T_a and gives heat to the surroundings [103, 104]. The volume of the reservoir is large enough that oscillating pressure variations can be neglected [102].

During the expansion process the gas in the pulse tube expands adiabatically and therefore reduces its temperature. The cooled gas then flows through X_L with temperature below T_L and creates a cooling effect. In addition, the gas takes heat from the regenerator previously stored [104]. At the warm end X_3, the gas flows out of the reservoir into the pulse tube through the orifice at temperature T_a. Then the cycle repeats.

In conclusion: gas which moves back and forth and remains inside the pulse tube, moves to the right with a high temperature and to the left with a low temperature. This creates a net enthalpy flow in the pulse tube. The thermodynamic processes inside the tube are complex, an in depth discussion can be found in [103]. Two stage PTR's temperatures of 2.1 K have been obtained which is close to the λ-point of Helium. Three stage PTR's can reach temperatures as low as 1.3 K using ^{3}He as an exchange gas. The low noise, low maintenance and costs effectiveness of PTRs make them the ideal choice for low temperature experiments. The installation and maintenance of two commercial cryostats (see section 3.2.1) as well as the assembly and installation of a home built cryostat (see section 3.2.2) have been a part of my PhD and were necessary to conduct low temperature measurements.

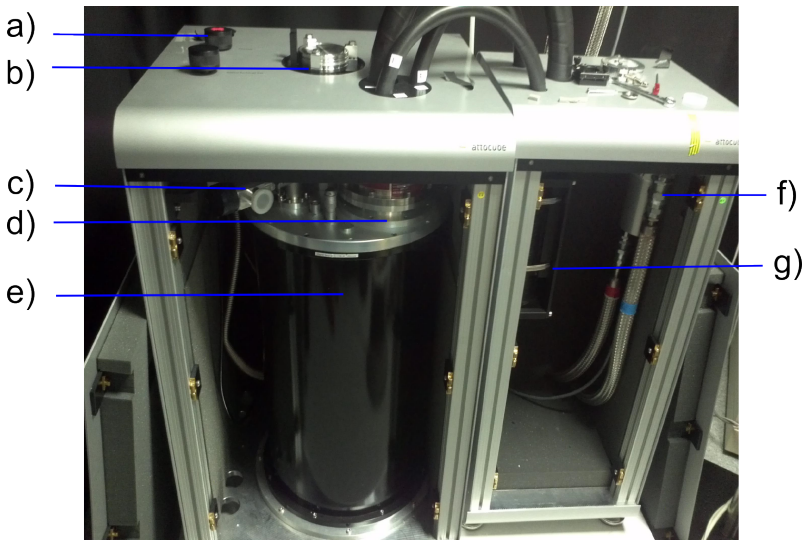

Fig. 3.10 Photograph of cryostat without cover: a) valves for sample tube evacuation and He purge, b) sample tube insert, c) valve for vacuum can evacuation, d) cold head e) vacuum can f) remote motor g) He reservoir.

3.2.1 attoDRY1000

Attocube's attoDRY1000 system provides a ready platform for sensitive measurements at cryogenic or variable temperatures ranging from 4 K to 300 K with high temperature stability of $\pm$ 10 mK at 4 K [104]. The system has been optimized for reduced vibrations and acoustic noise and claims to be the market leader with less than 100 pm RMS vibrations at the sample location. This is possible by hosting the cryostat in a attoDAMP anti-vibration cabinet (see Fig. 3.10).

The main advantage of the system is the design that allows fast turn around times for sample exchanges. The samples can be exchanged without warming up and venting the entire cryostat. Only the sample tube, via a top loading system, is exchanged and can be cooled down within 1-2 h. Inside the sample tube, a low pressure He environment is used as an exchange gas. The cooling power at the sample location is 5mW (at 5K).

The two systems purchased have built in superconducting magnets with a magnetic flux density (B) up to B = 9 T which increases the cool down time of the entire cryostat from 10 to 15 h. The cryostat is well isolated from the compressor, but vibrations from the environment and the compressor, which were assumed to still travel through the lab floor had to be reduced by placing the cryostat onto an additional vibration isolation platform using air springs. The compressors were placed onto vibration isolating pads. Both measures ensured that low frequency vibrations can not travel to the cryostat through the suspended laboratory floor. This vibration isolation eliminated vibrations previously measurable by a fluctuating PL signal and moving laser focal-spot visible on the microscope's CCD camera.

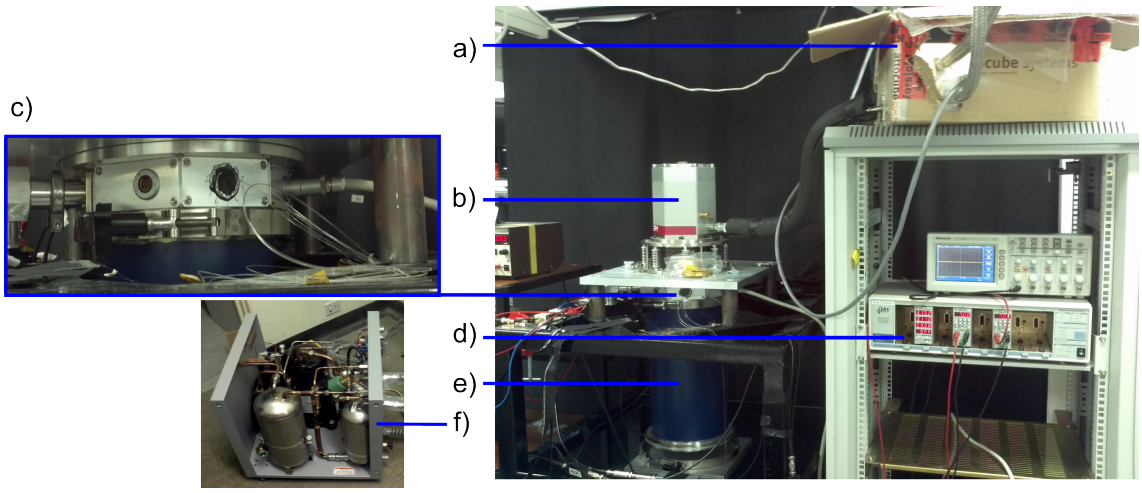

Fig. 3.11 setup of home built cryostat with a) remote motor, b) cold head, c) vent valve, feed-through for fibres and cables, d) SIM900 unit for temperature read out, e) vacuum can, f) remote compressor

3.2.2 PT403-RM CRYOREFRIGERATOR

A home built cryostat was assembled using a pulsed tube cryostat from Cryomech including a cold head (PT403) with remote motor and compressor package (CP830 Water Cooled) (see Fig.3.11 b). The connection between the remote motor and the compressor were established with Helium flex limes (1/2"' ID) for high pressure and (3/4" ID) for low pressure, as well as a cold head motor cord. The remote motor includes the moving parts necessary for a PTR and is only connected with a Helium flex line to the cold head to isolate vibrations Fig.3.11 f). The steel main frame, feed through, vacuum can, heat shield and temperature stages were designed by Dr. M.Tanner, Prof. R. Hadfield and co-designed and manufactured by the Heriot-Watt mechanical workshop. In-house fabrication of all components apart from the cooling cycle allowed a hugely reduced cost for a state-of-the-art cryostat in comparison to a commercially available turnkey version such as the attodry1000.

3.2.2.1 Cold head

The cold head stages and thermally insulating rods were glued using a two component epoxy (Stycast 2850 FT Black Epoxy - with Catalyst 23LV)(Fig. 3.12 b,e) (Fig. 3.12 e). The heat exchanger was connected using flexible copper ribbons to the 60 K and 4 K stages (Fig. 3.12 d). The cold head is mounted on a spring for vibration isolation, which contracts when the chamber is evacuated, resulting in the change of sample stage to heat exchanger distance. To improve the thermal conductivity the oxygen-free copper parts were cleaned from a layer of oxide and coated with a heat conducting paste (Apiezon N grease (25g) for cryogenic heatsinking and fixed with brass screws which contract at low temperatues and create a better contact.

To carry out experiments the cryostat had to be equipped with feed-throughs for optical fibres and electric wires. Aluminum plates were manufactured with the required

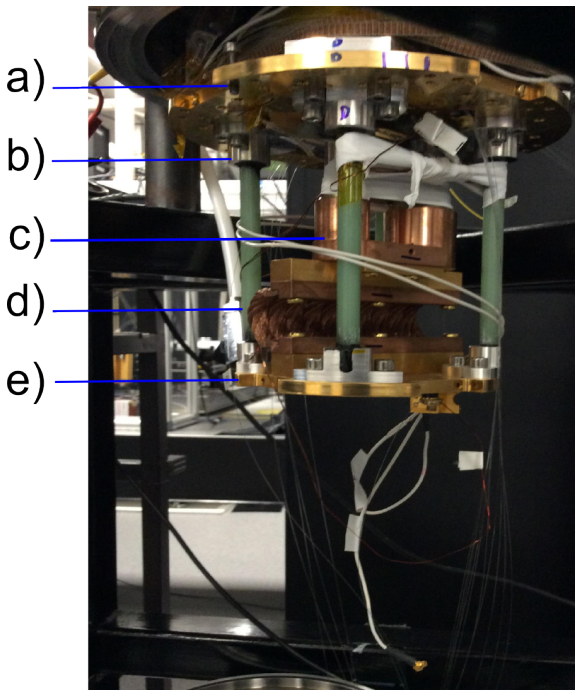

Fig. 3.12 Image of the cryostat inside a) first cooling stage (60K), b) aluminum part with glued polymer rod, c) second stage heat exchange (4K), d) flexible Cu ribbons for heat exchange, e) sample stage

feed-through hole sizes for Fisher connectors, SMA connectors and fibre feed-throughs. The aluminum plates are interchangeable and allow for different types of feed-throughs to be easily upgraded. The Fisher and SMA connectors were fixed using the supplied nuts onto the aluminum plates. Two Fisher connectors were integrated: one 12 pin connector for temperature read out and one 18 pin connector for nanopozitioners, scanners, photodiodes. The fisher connectors were soldered to a 12 pair twisted Copper ribbon ("woven loom") with 90 μm diameter and a resistance of 2.3 Ω/m. The cables were wrapped around the top part and thermally anchored to the 60 K stage using clamps and brass screws. The wires from the temperature diodes were soldered directly onto the copper loom. The cables from the 18 pin Fisher connector were soldered to two 18 pin plug bars which are compatible with attocube's nanopositioner cable standard new and old pin size. Two types of optical fibres were used (980 HP) and (1310BHP). Inside the cryostat the fibres were wrapped around the 60 K stage for thermal anchoring. In addition, they were clamped on the 60 K and 4 K stage for the same purpose before reaching the sample/detector mounted on the 4 K stage. The fibres were spliced using an automated fibre splicer to detectors inside the cryostat. To measure the temperature in the cryostat, Lakeshore DT-670 diodes were purchased. 3 diodes were mounted to monitor the temperature in the cryostat. A DT-670D-CU diode (30 K - 100 K $\pm$ 0.25 K) is placed at the first stage (60 K). A DT-670A-CU diode (2 K - 100 K $\pm$ 0.25 K) at the coldest point of the cryostat's second stage heat exchanger and one at the 4K stage to measure the sample temperature. The diodes were fastened using brass screws and heatsink paste was applied to create a good thermal contact. The diodes were connected to a fisher connector via a cop-

per loom. A break-out box was made to function as an adapter. The breakout box allowed to connect the fisher connector to two separate 6-pin serial ribbons which were suitable to be connected to a SIM922 diode temperature monitor, capable of reading and displaying 4 temperature diodes, housed inside a Standford Research Systems (SRS) SIM900 mainframe. In addition the SIM900 mainframe included two SIM928 voltage sources that function as a power supply for superconducting nanowire single-photon detectors (SNSPDs). The calibration curve supplied by Lake Shore for the voltage to temperature conversion was programmed into the SIM922 diode module using a python code via a USB to serial connection.

Apart from solid conduction and residual gas condution thermal radiation is the dominating heat load contribution. Therefore a heat shield ensures that no thermal radiation from the room temperature vacuum can heat the sample. The heat shield and the upper interior part of the cryostat is wrapped in mylar, to further reduce thermal radiation reaching the center of the cryostat. The cryostat is evacuated using a turbo pump backed by a scroll pump. When the cryostat reached pressures below 10^{-4} mbar the compressor can be switched on to start the cooling. The heat exchanger (coldest point in cryostat (see section3.2) acts as a cold trap for the remaining air molecules and reduces the vacuum even further at low temperatures. A computer program that uses the serial port of the SIM900 unit recorded the temperatures vs time during cool-down.

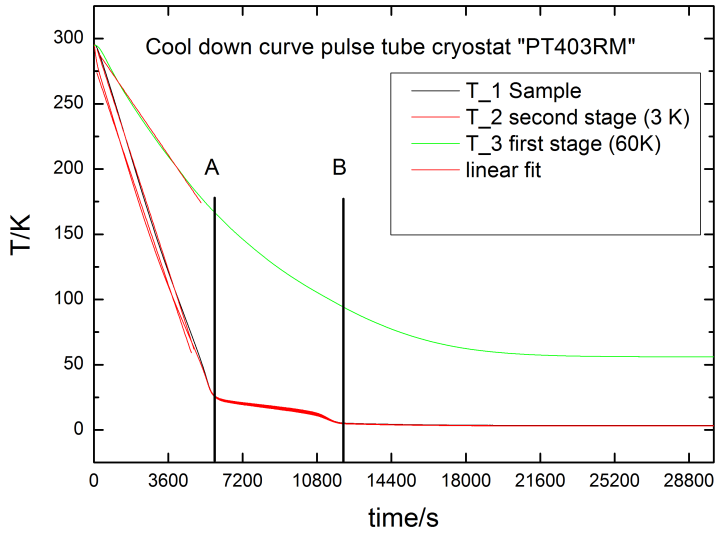

Fig. 3.13 Cryostat temperature vs time during cool down for final cooldown. Graphs shows the temperature measured at three point in the cryostat. Sample holder temperature T_1, second (3 K) cooldown stage T_2 and First (60 K) stage. The two points marked A and B show the time span which is needed to cool down the first stage to $\approx$ 100 K before the second stage can reach its minimum temperature of $\approx$ 3 K.

The cool down rate was determined by a linear fit to the T vs time plot of the first temp diode attached to a second cooling stage and was measured to be 119.3 K/h. At the end of the second cooldown the cryostat reached a temperature of 2.7 K after 8 hours

using Mylar wrapped around the heat shield with a cooldown rate of 106.9 K/h. The third cooldown with all optical fibres and electrical wires implemented which created an additional heatflux into the cryostat did not seem to influence the cooldown rate (172.8 K/h). The better vacuum in the chamber of 1.77×10^{-5} mbar instead of 2×10^{-4} mbar seemed to have a better insulating effect(see Tab. 3.3). The solid heat conductors connected to the outer cryostat wall at room temperature did not seem to reduce the cooling power. Fig.3.13 shows a slow down in cooling between point A and B, which is due to the 60 K stage not being cold enough. When it reaches approximately 100 K, the second stage is able to reach its lowest temperature which fluctuates between 2.8 K and 3.2 K. The cryostat is able to reach a temperature of 3 K at the second stage heat exchanger with $\pm$ 0.2 K due to the pulsed nature of the cryostat. The sample temperature only fluctuates by $\pm$ 0.1 K and reaches 3.2 K. The cool down time can be improved by adding a LN_2 precooling loop to the system.

Cooldown #	cooldown rate (K/h)	Vacuum in (mbar)
1 (no mylar)	-119.3	$2x10^{-4}$
2 (with mylar)	-106.9	$2.00x10^{-4}$
3 (all wires and fibres)	-172.8	$1.77x10^{-5}$

Table 3.3 Cool down rates compared to the chamber vacuum and amount of heat conducting materials placed in the cryostat. It was noted that the vacuum level is the main contributor of heat exchange and therefore determines the cooldown rate. The minimum temperature that can be reached is determined by the amount of solid heat conductors and thermal radiation, hence the cryostat acts as a cold trap and residual gas is trapped on the heat exchanger.

3.3 Optical spectroscopy

Optical spectroscopy provides a way to study a wide range of the energies and properties of QD's. In photoluminescence spectroscopy (PL), the sample is excited using laser light. In the case of resonant excitation carriers are created within the confined quantum levels. For non-resonant excitation, carriers within the continuum states of the sample are created. Commonly the wetting-layer or substrate energy levels are used which have fast relaxation times of < 35 ps [105, 106]. As the excitation power is increased, excitons form faster than they recombine, and higher lying energy levels are filled [107, 108]. Fig.3.14 shows the experimental setup used for non-resonant PL spectroscopy of the QDs investigated in this thesis. A microscope head collects the signal from the sample inside a crypostat with lasers for excitation and alignment purposes, a spectrometer to measure spectra (see section 3.3.1) and Hanbury Brown-Twiss interferometer (HBT) used for time correlated single photon counting measurements (TCSPC) (see section 3.3.2).

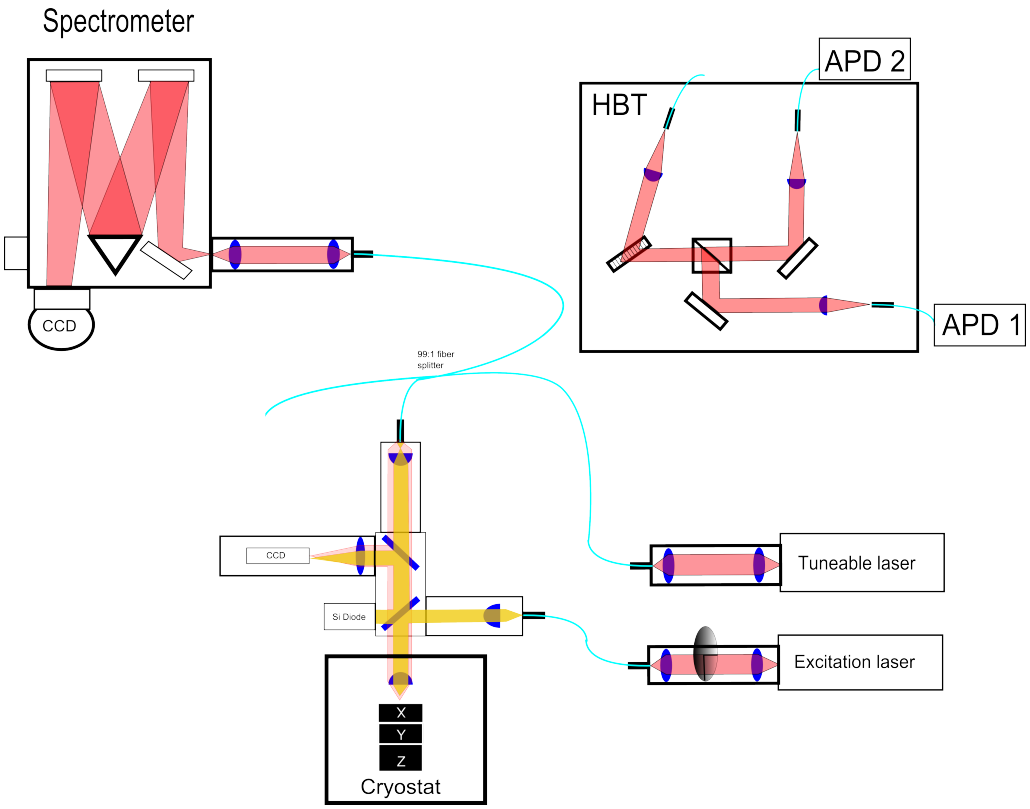

Fig. 3.14 Experimental spectroscopy setup overview showing the microscope head, cryostat, spectrometer with CCD, HBT, excitation laser with ND filter wheel, wavelength tunable excitation laser.

3.3.1 Photoluminescence spectroscopy

Photoluminescent spectra were taken using a spectrometer (Acton research corporation 0.5 m) equiped with a liquid nitrogen cooled CCD camera (Princeton instruments). The fibre coupled PL signal from the microscope head is guided to the XY translator (ST1XY-D/M) of the spectrometer coupling optics (see Fig.3.15 a). The coupling optics of the spectrometer consists of two achromatic doublet lenses, a collimating lens (f = 50 mm) and a focusing lens (f = 100 mm), focuses the light onto a size variable entrance slit. The effective NA of the coupling optics matches the NA of the spectrometer which allows maximum coupling efficiency without the loss of spectral resolution. Additionally a long pass filter was used to block 830 nm CW laser light used for excitation. After the PL signal passes the entrance slit it is reflected by two mirrors before it is diffracted by a grating (see Fig.3.15 d). The spectrometer has three gratings mounted on a turret (see Fig.3.15 e). The gratings with 300, 1200 and 1800 grooves/mm are blazed at 500, 750 and 500 nm respectively. From the grating the light is guided onto a final mirror which reflect the diffracted light onto the CCD camera or onto a flip mirror which allows the light to be directed to the exit port (see Fig.3.15 f,h). The back-illuminated CCD camera has a liquid nitrogen cooled Si array with 1340 x 100 pixels each 20μ x 20μ in size (see Fig.3.15 f - g). A heater keeps the the camera at - 110 °C. The low temperature allows for a high sensitivity with a background noise of 100 counts per pixel caused by electric read

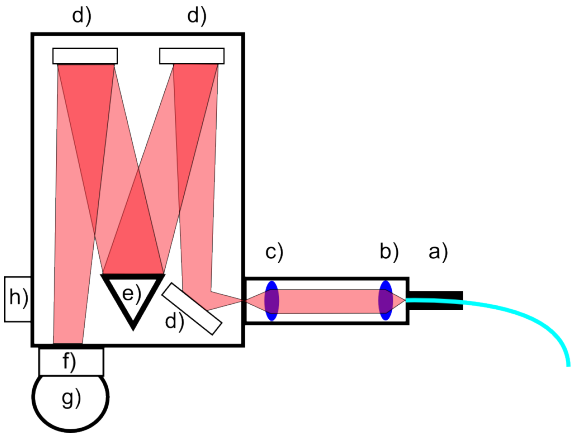

Fig. 3.15 Schematic diagram of SP-500i spectrometer a) coupling optics with b) collimating lens c) focusing lens d) mirrors e) motor controlled gratings f) CCD camera with g) Liquid Nitrogen reservoir h) optional exit port.

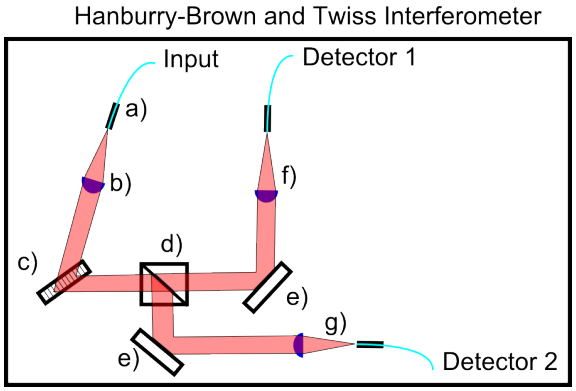

Fig. 3.16 Schematic diagram of HBT a) PL signal from microscope head b) collimating lens c) transmission grating d) beamsplitter cube e) mirrors on gimbal mounts f) detector arm 1, g) detector arm 2.

out noise which can be changed by a bias option. The quantum efficiency of the CCD is 30 % at 950 nm. By using the 1800 grating a maximum resolution of 35 μeV is obtained which is the FWHM of a narowband laser at 950 nm.

3.3.2 Time-correlated single photon counting

An essential tool in quantum optics is a light source that emits an exact number of photons at regular time intervals [109]. Such a source can be used in metrology and QIP (see section 1.2.4). To investigate the antibunching properties ($g^{(2)}$) and spontaneous emission rate (Γ) of a quantum emitter, temporal analysis is required.

Second order correlation measurements describe the statistical behavior of the intensity of the light field and a time delay τ, and are used to measure the antibunching properties of a source. Lifetime measurements are used to measure the spontaneous emission decay rate of an emitter. A Hanburry-Brown-Twiss Interferometer (HBT) is used to carry out second order correlation measurements. This measurement technique is not effected by the loss between the emitter and the detector [106] and the detector dead time is over-

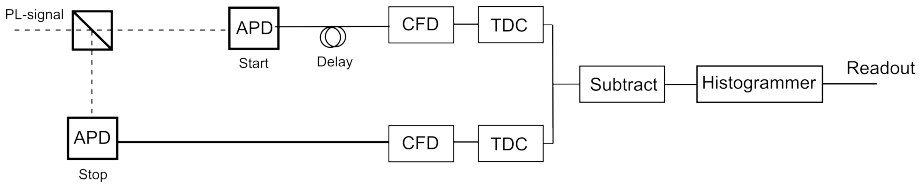

Fig. 3.17 flowchart of the PicoHarp 300 readout and timing electronics.

come by using two independent detectors [12]. Auto- and cross-correlation measurements can be carried out with minor changes to the setup.

Fig. 3.16 shows a sketch of the HBT used. Light is guided to the HBT using an optical fibre (see Fig 3.16 a). The light is collimated using an achromatic lens (AC254-075-B, NA = 0.167). Alignment of the fibre relative to the lens is controlled using a z-translation mount (SM1Z) which moves the lens and a XY translator which moves the fibre [110]. The collimated light is directed onto a spectrometer. The spectrometer guides a specific transition in the single QD PL spectra towards the desired collection arms. The spectrometer consists of a volume phase grating (Wasatch photonics 1200 lines/mm) with 25 x 25 mm clear aperture, which has a low polarization dependence and a transmission of 80% at 950 nm. This type of grating allows for near to 100 % transmission into first order diffraction. The resolution of the HBT is 51.65, 353, 841 μeV if a 5.5, 50 or 100 μm diameter optical fibre core is used as using a larger diameter core increases efficiency but reduces the resolution. The light from the transmission grating is directed onto 50:50 beam splitter cube (BSC,BS014). The grating and the BSC are mounted on a precision rotation platform (PR01/M). Two Gimbal mounts (GM200M/M) with mirrors (BB2-E03)are used to reflect the light exiting the BSC towards the two collection arms of the HBT. The mirrors are used as a filter which allows optimization of the arms for different wavelength in case of cross-correlation measurements and the same wavelength for auto correlation measurements. Two inch mirrors have been chosen to eliminate shadowing [110]. The HBT uses a aluminum breadboard (MB3045/M) as a base, which makes the HBT portable within the laboratory. The detectors used were two silicon single photon avalanche diodes with a timing jitter of 535 ps and a joint probability distribution of FWHM $\sqrt{(}2)$ x 535 ps = 756 ps.

For the timing electronics a PicoHarp 300 TCSPC system was used. It has a time resolution of up to 4 ps and the Instrument Response Funcion (IRF) can be as low as 40 ps FWHM if matched with modern APDs. For pulsed excitation a diode laser controller (PDL 800-B) was used which also provided an electronic trigger signal to the PicoHarp 300 sync. channel. One arm of the HBT acts as the start, the other as the stop signal. The APD's are connected to the start and stop channels of The PicoHarp 300 (see Fig.3.17 f - g). The start and stop channels have a constant fraction discriminator (CFD) which extracts the exact timing information from the detector pulse that can vary in amplitude. In conventional systems the signals are fed to a time to amplitude converter (TAC). The result is a voltage proportional to the time difference between the two signals [111]. The

voltage is then fed to an analog to digital converter (ADC) which addresses the timing value to the histogrammer. In the Picoharp the TAC and ADC are replaced by a Time to Digital Converter (TDC) which allows for picosecond timing and the virtual extension of the measurements period using digital counters. Two of these circuits are used in the PicoHarp 300 on each input channel. The two time figures ($\tau = t_{start} - t_{stop}$) from the start and stop channel are subtracted and then histogrammed. The time delay τ is binnned as a number of photons per time delay.

The data is the unnormalized correlation function $G^{(2)}$ convolved with the instrument response function (IRF). The data is deconvolved with the IRF, normalized and fitted with equation 3.2 [112, 113].

$$g^{(2)}(\tau) = 1 - a * e^{-\tau/t_d} \tag{3.2}$$

where the decay time is $t_d = 1/(\Gamma + Wp)$, and a is a fitting parameter, Γ is the electron–hole recombination rate, and W_p is the effective pump rate into the radiatively active upper state. The factor a compensates for background and residual biexcitonic effects [113].

In Time-correlated single photon counting (TCSPC), arrival times of photons are histogrammed over many excitation and fluorescence cycles [111]. The resulting histogram shows a time dependent intensity profile of the emitted light, represents the fluorescent decay and is a measure of the spontaneous emission rate (see section 1.2.4). The measurements are carried out in the low excitation regime. The transmission grating in the HBT is used to filter the adequate exciton emission lines. A pulsed laser triggers start using a BNC sync cable and the APD acts as the stop channel. The collected data is shown in Fig. 3.18 and is a convolution of the exponential decay and the IRF [114]. The IRF is measured by directing the pulsed laser directly into the HBT. The instrument response time is the FWHM of the IRF. After deconvolution with the IRF the data is fitted using an exponential decay function (see eqn:3.3)

$$A_t = A_{t_0} * e^{-(t/\tau)} \tag{3.3}$$

Where A_{t_0} is the initial amplitude at t = 0 and τ the lifetime is the time at which the quantity is reduced to 1/e times its initial value. Both the lifetime and $g^{(2)}$ have been measured and are presented in the results chapter.

3.3.3 Setup efficiency

The efficiency of the setup has to be measured so the extraction efficiency of the nanowire can be determined. The optical path from the nanowire to the CCD consist of the following optical components with their respective transmission efficiencies: a objective lens $T_{obj} = 93\%$, glass window (BK7) $T_{BK7} = 94\%$, two beamsplitters combined (BS) $T_{BS} = 63\%$, a long pass filter $T_{LP} = 85\%$. This is followed by coupling into collection

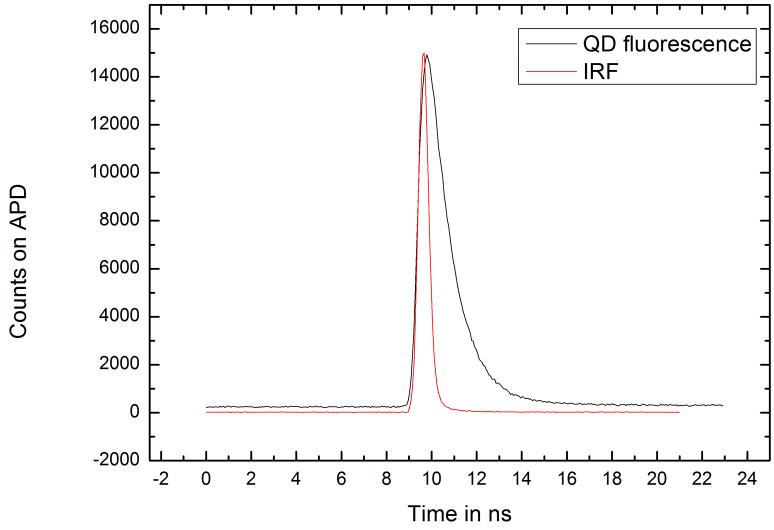

Fig. 3.18 Graph of a convolved QD fluorescence exponential decay and the IRF.

fibre at the top of the head. The transmission efficiency due to alignment and collection at the top of the microscope head was $T_{align} = 6\%$. This collection fibre was one end of a 99/1 fibre beam splitter with the collection arm transmitting $T_{99/1} = 98\%$. The combined transmission efficiency of the microscope is then

$$T_{\mu scope} = T_{obj} x T_{BK7} x T_{BS} x T_{LP} x T_{align} = 3.05\% \tag{3.4}$$

This combined transmission efficiencies were measured both individually and collectively. The Hanburry-Brown-Twiss (HBT) interferometer has an efficiency of $T_{HBT} = 56.56\%$, and the quantum efficiency for each of the APDs is $QE_{APD} = 26\%$. Using the known APD quantum efficiency, the counts on the APD and the corresponding photoluminescent spectra of both laser light and QD emission, the efficiency of the coupling into the spectrometer and CCD using the 1800 l/mm grating was found to be $T_{spec} = 0.42\%$, this was verified by measurements at high and low powers.

3.4 Strain-tuning using piezoelectric crystals

The piezoelectric effect was first observed in quartz crystals by Pierre and Jacques Curie in 1880 [115–117]. Piezoelectric materials convert mechanical to electrical energy and vice versa [118]. The ability to change shape under an electric field is called electrostriction and is observed in all dielectric materials that are composed of more than one type of ion. When the material is exposed to an external electric field, positive ions in the crystal lattice will be slightly displaced in the direction of the field and negative ions will be displaced in the opposite direction. This displacement results in an overall strain (elongation) of the bulk material in the direction of the field, and a reduced thickness in the orthogonal (in

plane) direction.

Ferroelectric materials spontaneously change their polarization which is reversible unlike in piezoelectric materials and shape under and applied electric field, below the ferroelectric phase transition temperature T_C (Curie point) [117]. Alternative materials are relaxor based ferroelectrics, where the transition between piezoelectric behavior and loss of piezoelectric capability does not occur at a specific temperature T_C , but over a temperature range (Curie range) [119].

One of the most studied perovskite (ABO_3) relaxor-ferroelectric materials is the PMN-PT where the PMN is the relaxor and PT the ferroelectric. Unlike the PZTs, PMN-PTs can be grown as large single crystals [120]. PMN-PTs have a high dielectric permittivity, high electrostriction and are suitable for multilayer capacitors, actuators, transducers, acoustic sensors and electro-optical (photonic) devices [121, 122]. PMN-PTs show a 5-10 times higher piezoelectric coefficient d_{ij} [117, 118, 122] and strain then PZT's. Especially near the morphotropic phase boundary (MPB), the piezoelectric coefficient is naturally high [122]. The MPB is a phase transition between the tetragonal and the rhombohedral ferroelectric phases in a composition temperature diagram (see Fig.3.19 a). The MPB is strongly temperature dependent in relaxor-PT single crystals and varies as a result of composition and mechanical pressure [117, 123]. Due to the composition dependent crystal properties, the piezoelectric strain decreases with lower PT content [122].

When the PNM-PT is grown it is in its natural relaxor state and needs to be poled before first time use, using a electric field. The electric field, above a treshold of 2.2KV/cm, induces a micro-to-macrodomain phase transition from rhombohedral to monoclinic [122]. A current spike in a I-V diagram can be observed. After removal of the field the relaxor state does not recover and a permament ferroelectric state is maintained.

A PMN-PT is suitable to apply strain to thin films at cryogenic temperatures, allowing the investigation of bi-axial strain dependence of physical properties [122]. The piezoelectric effect reduces with decreasing temperature, and at 50 K drops below 25% of the room temperature value (see Fig.3.19 b). The strain at low temperatures is reversible if no domain switching occurs. Therefore, the crystal should be cooled while a positive electric field is applied. The voltages applied at low temperature should be between $-E_c < 0 < E_{max}$, where E_c is the coercive electric field and E_{max} the maximum electric field in the direction of poling. Commonly, maximum electric fields of E_{max} = 30kV/cm at cryogenic temperatures without a He athmosphere are used [122].

A 10 x 10 mm 28%PMN-PT polished substrate was used to carry out bi-axial strain tuning experiments. To apply a voltage to the PMN-PT, it is coated with 5 nm Cr as an adhesion layer and a 100 nm Au contact layer by e-beam evaporation. PL spectroscopy was used to measure QD emission detuning with respect to the applied electric field to the PMN-PT. To carry out PL spectroscopy of the strain tunable sample at low temperatures, it has to be mounted on a sample holder that allows for electrical contacting. The sample was placed onto Au coated GaAs wafer and held in place with silver paint (see Fig. 3.20).

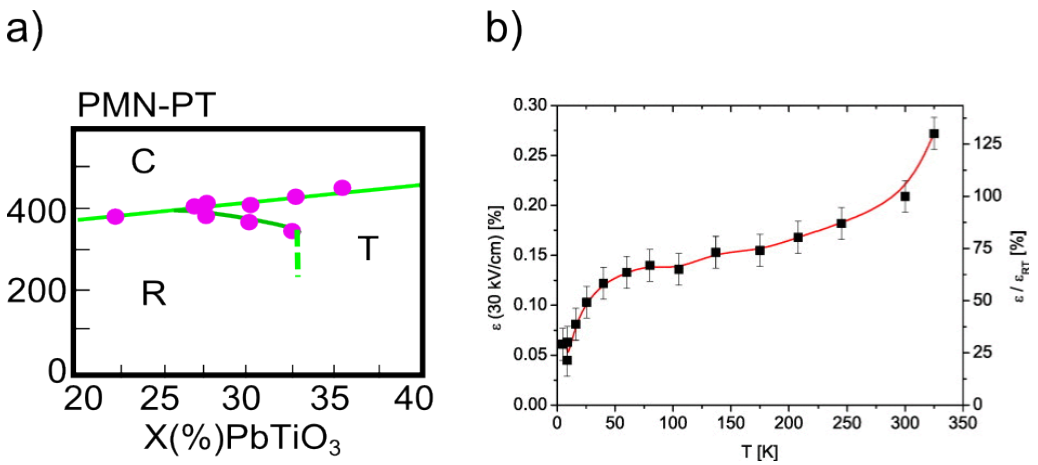

Fig. 3.19 Temperature dependent properties of PMN-PT a) phase diagram with composition X on the x axis and temperature T on the y axis. MPB between R (rhombohedral) and T (tetragonal). Area marked C is above T_C. Graph taken from [117]. b) strain vs PMN-PT temperature at an aplied electric field of 30 kV/cm. Absolute strain on left y axis and relative strain to room temp on right y axis. Graph taken from [122].

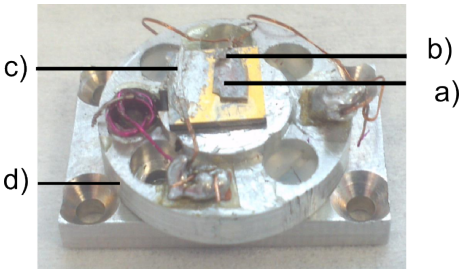

Fig. 3.20 Photograph of aluminum button used as a sample mount and as contact pad for electric wiring. a) PMN-PT with GaAs nanowires, b) top contact, c) bottom contact, d) sample holder.

The GaAs wafer was fixed onto a Al sample holder with vacuum grease. The Al button allows the mounting of the sample to the xyz-nanopositioners using Teflon screws. The top and bottom of the PMN-PT Au layer was contacted to a Cu wire using silver paint, the Cu wires were fixed with clear wax to the sample holder. The positive pole was used as the top contact and ground as the back contact (see Fig.3.21).

As described above before first time use the PMN-PT needs to be poled. A power supply (Stanford Instruments PS350/5000V-25W) and a multimeter (Keithley 2000) were connected to a PC via a General Purpose Interface Bus (GPIB) port and controlled using a Labview code written by Dr S.Kumar. A voltage sweep from 0 to 300 V was carried out several times and the current was measured as described above. The first voltage sweep showed the characteristic current peak when the PMN-PT undergoes poling (see Fig.3.22). The second and third sweep did not show this peak. This showed that the PMN-PT is sufficiently contacted and the poling of the crystal worked.

In the experimental setup the breakoutbox for attocube microscope tube was used to apply voltages between 1-990 V at 11 K. He exchange gas is used to transfer heat between the sample and the cryostat. Due to the high voltages applied, the He exchange

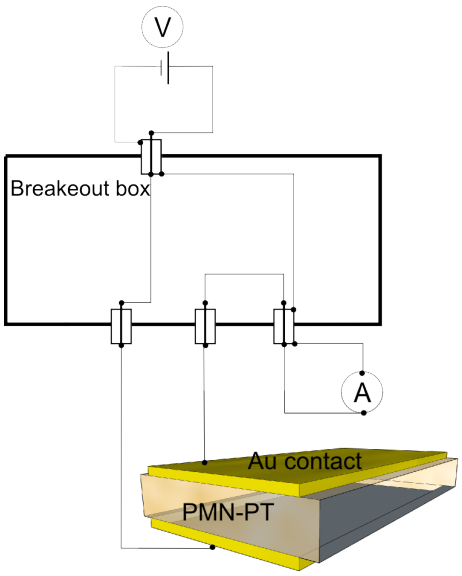

Fig. 3.21 Setup diagram used for strain tuning. Voltage source (V) and high voltage Breakout box, Ammeter (A) and Sample. The top of the sample is grounded to avoid charges accumulating near the dot.

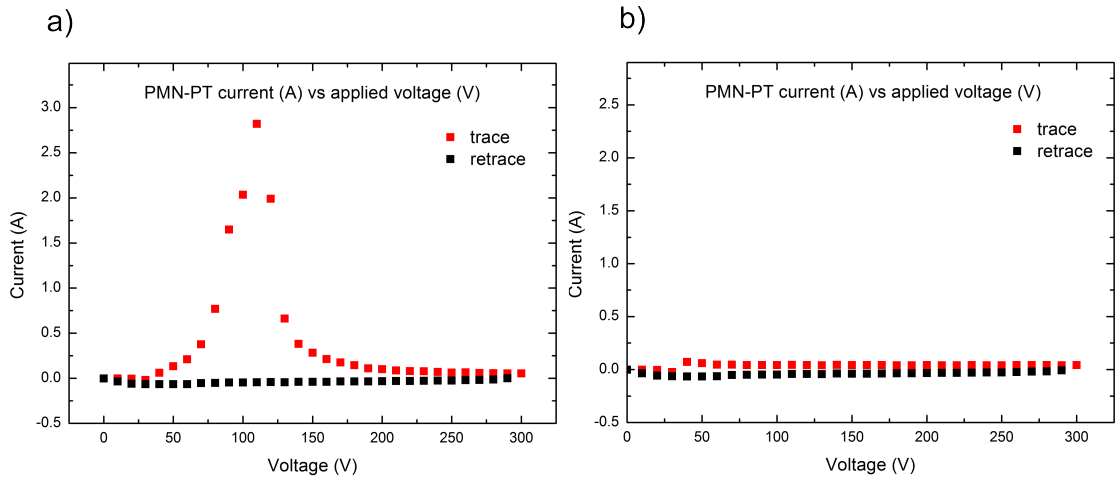

Fig. 3.22 Current vs voltage graphs showing a) current spike on the first sweep/trace but none on the retrace. b) Second voltage sweep shows no current spike on trace or retrace indicating that poling was successful

gas pressure had to be reduced to 5×10^{-3} mbar. In previous strain-tuning experiments using PZT's, pressures of 15 mbar caused plasma strikes at 300 V. For low temperature strain tuning experiments, 300 V should be applied to the sample while cooling down. Even though the sample was poled at room temperature and a voltage of 300 V was applied when cooled down, the sample still triggered the current safety switch after a threshold voltage of first 400 V then 500 V. After several voltage cycles of the sample it was possible to apply 500 V. After cleaning the sample in acetone and a second cool down it was possible to reach a bias voltage of 990 V after several voltage cycles. Keeping the sample under a higher voltage for longer time periods allowed a current to flow as well and triggered the current safety switch.

PL spectra for different nanowires were taken using different bias voltages applied to

the PMN-PT. The exciton emission was fitted using a Lorentzian function to determine the exact QD emission peak intensity. This allowed to determine the shift in the centre wavelength with respect to the applied strain.

Chapter 4

Spectroscopy results

4.1 PL spectroscopy of nanowires

Pl spectra of the nanowires were taken at 4.5 K as described in section 3.3.1. High and low power (inset) PL-spectra of a QD (DOT A) in one of the brightest nanowires are shown in Fig.4.1. The exciton states are identified by the characteristic Coulomb interactions observed in experiments with similar QDs in charge tunable devices [124] and the linear (quadratic) power dependence for single X^0 (bi-) excitons XX. The spectra in Fig.4.1 are representative of what is typically observed from QDs in the nanowires, except with varying central energies and peak intensities. At low excitation the XX emission line is not visible (see Fig.4.1 Inset). As the excitation power is increased the XX line appears and becomes dominant (see Fig.4.1), if the power is further increased the X^0 line intensity reduces (not shown). Further confirmation of the state assignment can be obtained by measuring the photon-intensity correlations between separate excitonic states [125].

Numerous nanowires across the sample with constant D (110 nm) and h (2 μm) but varying d and α were measured. Prior to optical characterization, the nanowire diameter d of each group of 16 nominal identical nanowires was measured using a SEM. A map of the approximate nanowire diameter across the sample was noted. From the nanowire diameter measured by SEM the most promising groups of nanowires were selected to carry out PL measurements. The brightest nanowires were found in the group marked with I13 with an average d = 232 $\pm$ 4 nm. From this section of the sample, and the neighboring sections marked I12 and I14 individual measurements of the nanowire diameter and angle were made. All pillars from section I12 - I14 have been individually optically characterized by PL measurements. Each spectrum was analyzed and the brightest quantum dot inside each pillar was noted in a table with the according measurements of the exact diameter and taper angle. The data is plotted in Fig.4.2 a) which shows the counts/s on the spectrometer CCD vs the normalized wire diameter and the top taper angle α (see Fig.4.2 b).

The normalized wire diameters varied between d/λ = 0.235 - 0.264, corresponding to a constant β >90 %. The taper angles varied between 7° - 15°, corresponding to a theoretical transmission efficiency between $\sim$ 70 % - 40 %. From Fig.4.2a-b) one can

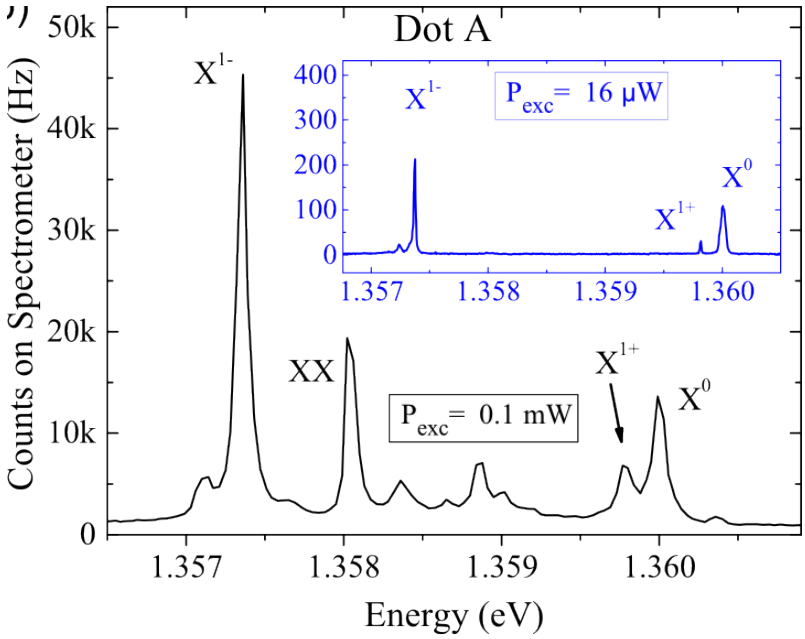

Fig. 4.1 PL spectra of QD (Dot A) in the brightest nanowire, showing the different exciton states at saturation from left to right X^{1-}, XX, X^{1+}, X^0. Inset: Low excitation power PL spectra of Dot A. The X^{1-}, X^{1+} and X^0 emission visible, at this low excitation power the XX line is not visible.

see that the QD with the highest PL intensity has a low $d/\lambda = 0.235$ and a low taper angle of 8.5°. At this normalized wire diameter, the majority of the light couples into the fundamental HE_{11} mode (see Fig. 1.13 a) and the taper angle corresponds to a theoretical transmission of $T \approx 65\%$, and a modal reflectivity of the planar Au mirror of $R \approx 0.9$ [62, 80–82, 84]. This gives a theoretical extraction efficiency of $\eta = \beta$x R x T = 0.9 x 0.9 x 0.65 = 0.53%.

The SEM images of the 16 brightest nanowires were compared. Correlations from the nanowire shape or surface roughness with the PL intensity could not be made, most likely due to the randomness of the QD location inside the nanowire which influences the spontaneous emission rate [84]. The QD with the lowest taper angle does not show a high PL signal, even though it has a low $d/\lambda = 0.248$. One could conclude that the QD is not located at the centre of the nanowire [84].

The surface of the nanowire is not perfect; it has dangling bonds and remaining impurities from the fabrication process. Ion damage approximately 30 nm deep, from implanted reactants during RIE, can be as high as 10^{19} cm^{-3} at the surface for Si ions with a DC Bias above 250 V [93], the DC bias used in our process was at times above 500 V. Non-resonant PL spectroscopy provides a tool to investigate the effect on QD's by nearby nanowire surface states and possible ion damage. When the nanowire is illuminated with a non-resonant laser, carriers above the GaAs band-gap are excited and can relax into the QD as well as fill defect surface states. When the excitation power (P_{exc}) is increased the number of carriers at the nanowire surface increases until they are saturated. Two QD's in one of the brightest nanowire were investigated (Dot A and B Fig.4.3 a) and b). A power

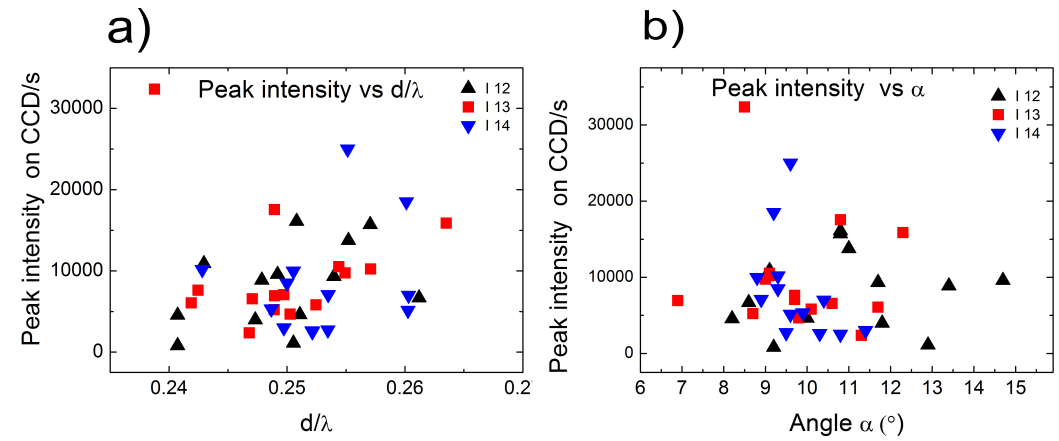

Fig. 4.2 a) Peak intensity on Spectromter CCD vs normalized pillar diameter d/λ. b) Peak intensity on Spectrometer CCD vs taper angle α.

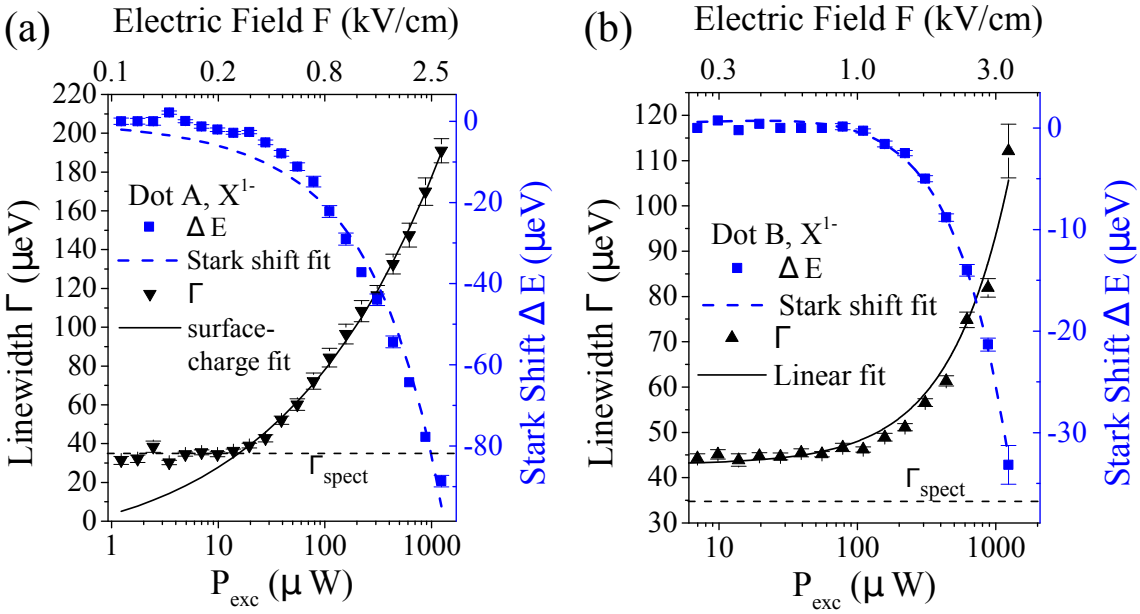

Fig. 4.3 The measured spectral linewidth (Γ) and Stark shifts (ΔE) as a function of excitation power (P_{exc}) are shown for the X^{1-} line for Dot A and Dot B in a) and b), respectively. A fit of the Stark effect allows an estimated field (F) to be calculated in each case. For Dot A, the *surface-charge fit* used to describe the dependence of Γ on P_{exc} is based on the fluctuating δF estimated from the electronic shot noise of the static F. For Dot B, the *surface-charge fit* fails to match the data as Γ exhibits a linear dependence to P_{exc}.

series was taken and the linewidth (Γ) and energy detuning (ΔE) of the X^{1-} emission line were plotted. For Dot A at $P_{exc} \leq 20\mu W$, ΔE is zero and Γ is resolution limited. For Dot B, ΔE is zero and Γ is constant ($\sim 45\mu eV$) but inhomogeneously broadened above the experimental resolution limit in the low power regime ($P_{exc} \leq 100\mu W$). For both QD's with increasing P_{exc}, ΔE increases and Γ broadens without saturation.

To better understand and quantify the effect of the surface states, we exploit the ability of the QD itself to function as in *insitu* probe of the local electric field [36, 37, 126, 127]. In an electric field, the quantum dot dipole produces a Stark shift with quadratic field dependence, and the energy detuning is given by $\Delta E = -pF + \beta F^2$, where F is the

electric field, p the permanent dipole moment, and β the polarizability.

To estimate F at the position of the QD based on ΔE observed in PL measurements, it was assumed that $\beta = -4\mu$eV/(kV/cm) [36, 37]. The fits from this procedure give in-plane dipole moments $p = 23 \pm 6\mu$eV/(kV/cm) and $-3.4 \pm 0.2\mu$eV/(kV/cm) for Dots A and B respectively, corresponding to an electron-hole seperation of $r = 2.3 \pm 0.6$Å and $r = -0.34 \pm 0.02$Å (from $p = er$). The fits are shown as the dashed lines in Fig.4.3, with the extracted values for F shown on the top x-axis in the figures. The fits agree well with the data and it was observed that F is linearly proportional to $\sqrt{P_{exc}}$ for each QD.

Furthermore we can estimate the fluctuating electric field, δF, by assuming the fluctuation (δn) in the number of electrons (n) located at the surface is proportional to the electronic shot noise: $\delta n \propto \sqrt{n}$. n was calculated by assuming electrons a distance $d/2$ create F, and then use δF to find the corresponding $\delta(\Delta E) \equiv \Gamma$ from the Stark equation. For Dot A, the estimated power broadening of Γ (shown as the solid line labeled *surface-charge fit* in Fig.4.3 a)) fits the experimental data very well above the system's resolution limit. The surface charge fit also enables us to estimate the power broadening below the resolution limit. Both the data and the extrapolated fit suggest the inhomogeneous broadening is dominated by the charges generated by the excitation laser at the nanowire surface.

The results from Dot A are promising for the generation of indistinguishable photons from a QD in a nanowire antenna. On the other hand, a fit with a linear dependence of Γ on P_{exc} is found to fit the data for Dot B much better than a surface charge fit, even in the high P_{exc} regime. This result suggests that unlike the behavior of Dot A's power broadening, Dot B's linewidth broadening is not primarily caused by the charges generated at the nanowire surface by non-resonant excitation.

4.1.1 Nanowire efficiency

Finite-difference time-domain (FDTD) simulations have been carried out by Dr. Yong Ma using Lumerical®, a commercial simulation software, to model the performance of the brightest nanowire fabricated. The results of the simulation are shown in Fig. 4.4 as a function of D, the radially centered dipole to mirror distance and include the following figures of merit: P_m the purcell factor, β the mode coupling efficiency into the HE_{11} mode, η the extraction efficiency and γ the collection efficiency. The simulated nanowire has a top taper angle α = 10°, h = 2 μm, and d/λ = 0.235 which is very close to the brightest fabricated nanowire Fig.4.7 a). At D = 110 nm, the nanowire has a extraction efficiency of 57% and a $P_m \approx 0.9$. Using a SiO^2 layer between the nanowire and the Au mirror increases the nanowire efficciency by 10-20% (verbal comun. Yong Ma).

To experimentally determine the extraction efficiency η of the nanowire, time-correlated single photon counting measurements were performed (Fig. 4.5 - 4.6). The correct excitonic line assignment and minimal dynamics (no bunching at i.e. $\tau > 1$) in the second order auto-correlation measurements enable estimation of the total η from a single dot (see Fig.

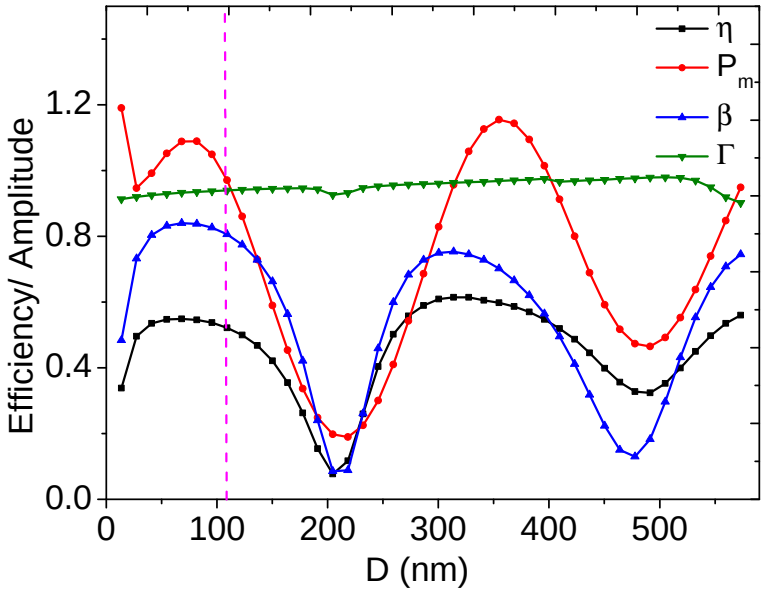

Fig. 4.4 Shows the figures of merit of a FDTD nanowire simulation. Which are:P_m the Purcell factor, β the mode coupling efficiency into the HE_{11} mode, η the extraction efficiency and Γ the collection efficiency.

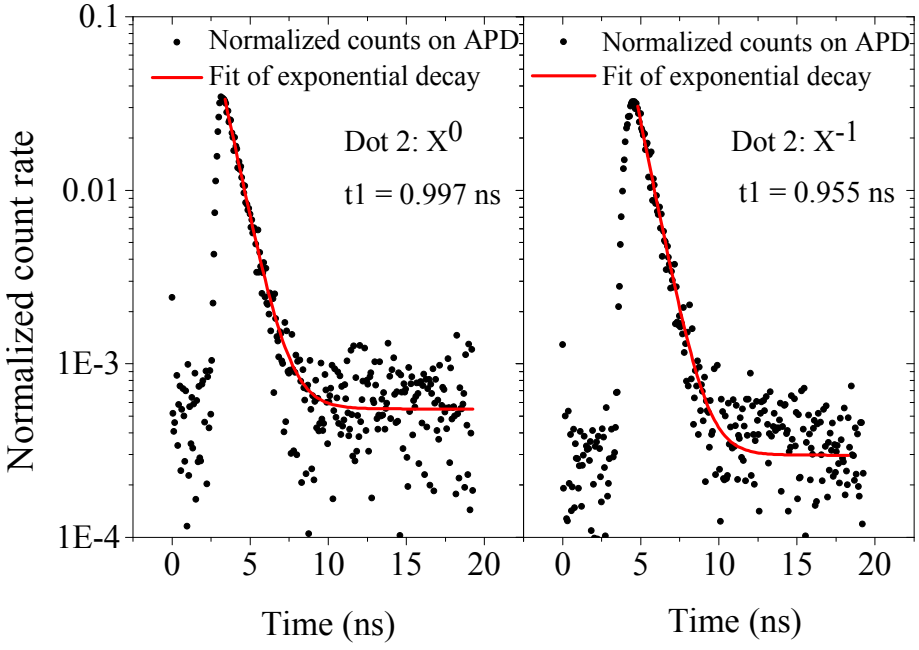

Fig. 4.5 Time-resolved photoluminescence of the X^0 and X^{-1} lines from Dot B. The determined transiion lifetimes are $\tau = 1$ ns approximately 10% to 20% longer than statistically expected for such dots [124] and in agreement with the slight inhibition of spontaneous emission predicted by P_m in Fig.4.4.

4.6). The power emitted by the QD at saturation is estimated from the emission rates of each excitonic state (defined as the inverse of the transition lifetime) and their relative integrated intensities. This is consistent with the photophysics of a QD emitter at saturation under contiuous-wave (cw) excitation, assuming perfect quantum efficiency. The time-resolved measurements show no evidence of complex dynamics, such as bi-exponential decay in autocorrelation measurements [128] (see Fig. 4.5). The measurements of the

X^0 and X^{-1} transitions for Dot B shown in Fig.4.5 each reveal transition lifetimes of τ = 1 ns, approximately 10% to 20% longer than statistically expected for such dots [124]. This is in agreement with the slight inhibition of spontaneous emission predicted by P_m in Fig.4.4.

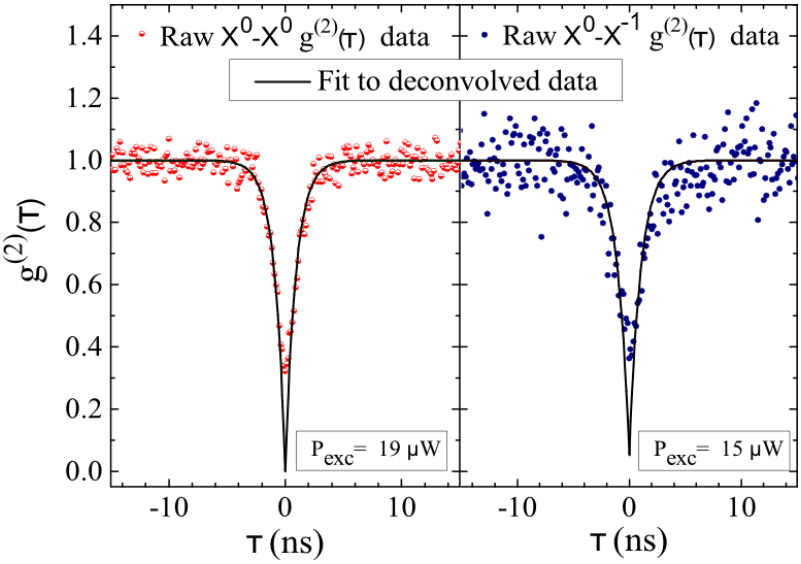

Fig. 4.6 Second order auto-correlation measurement of X^0 and cross-correlation between X^{-1} and X^0 for Dot B obtained at an excitation power of 19μW. The fit to the deconvolved data shows $g^2(0) \approx 0$ signifying high-purity single photon emission. The second order cross-correlation measurement between the X^0 and X^{-1} states also demonstrates clear antibunching, signifying that these states originate from the same QD [129].

Figure 4.6 shows the second order auto-correlation measuremtent of the X^{-1} state from Dot B. The raw data shows $g^2(0) < 0.5$ while the fit to the deconvolved data for detector jitter shows $g^2(0) \approx 0$, signifying high-purity single photon emission. The second order cross-correlation measurement between the X^0 and X^{-1} states also demonstrates clear antibunching, signifying that these states originate from the same QD [129]. Also the absence of complex dynamics demonstrates lack of the influence of surface charge fluctuations on charging of the QDs.

The efficiency of the experimental setup (from the objective lens to the CCD camera) was calibrated using a tunable laser at the QD emission wavelength. η was thus estimated for the 40 brightest dots in the 16 nominally identical nanowires as histogramed in Fig.4.7 b). The efficiency of the brightest QD was found to be $\eta_{max} = 57\%$ when each exciton state is included, and the average is $\bar{\eta} = 13\% \pm 10\%$. The most obvious explanation for the large standard deviation of η is the random positioning of the dots radially in the nanowires, which could be remedied in the future with a deterministic positioning technique [57]. The wavelength mismatch slightly contributes to the standard deviation as well. Additionally, the SEM images reveal surface defects and slight asymmetry in the nanowires, which may adversely affect performance.

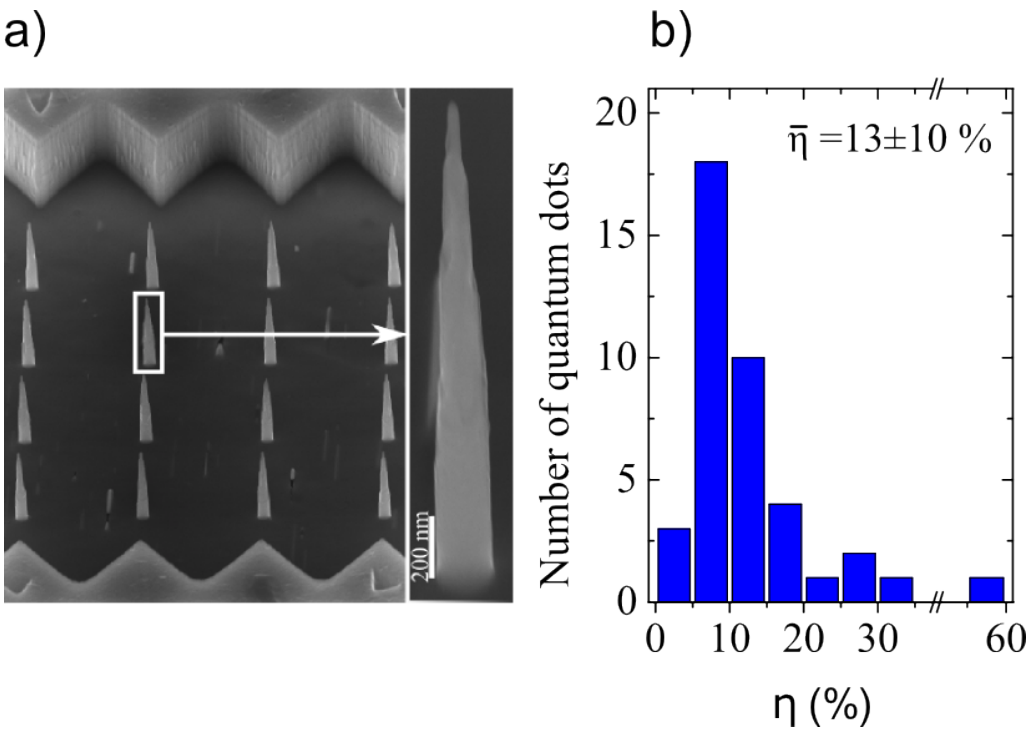

Fig. 4.7 a) SEM image of the brightest 16 nanowires, with the brightest nanowire being magnified. b) Shows a histogram of the estimated extraction efficiencies η from QDs in the 16 nanowires shown in a).

4.1.2 Strain-tuning

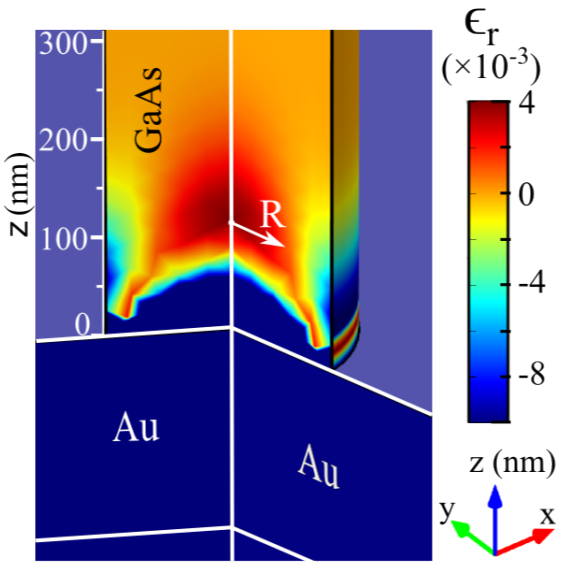

Fig. 4.8 Simulation of strain relaxation in the nanowire using the finite-element method. The plot shows the profile of relative strain $\varepsilon_r = \varepsilon(x,y,z)/|\varepsilon_0|$, where the strain is $\varepsilon(x,y,z)$ and the strain in the PMN-PT crystal is ε_0. The color legend is scaled to highlight the strain-field relaxation within the nanowire.

QD's change their emission properties when strain is applied. This was achieved by bonding the nanowires with the embedded QD's to a PMN-PT piezoelectric crystal. When a voltage is applied the material contracts or expands, depending on the electrical poling,

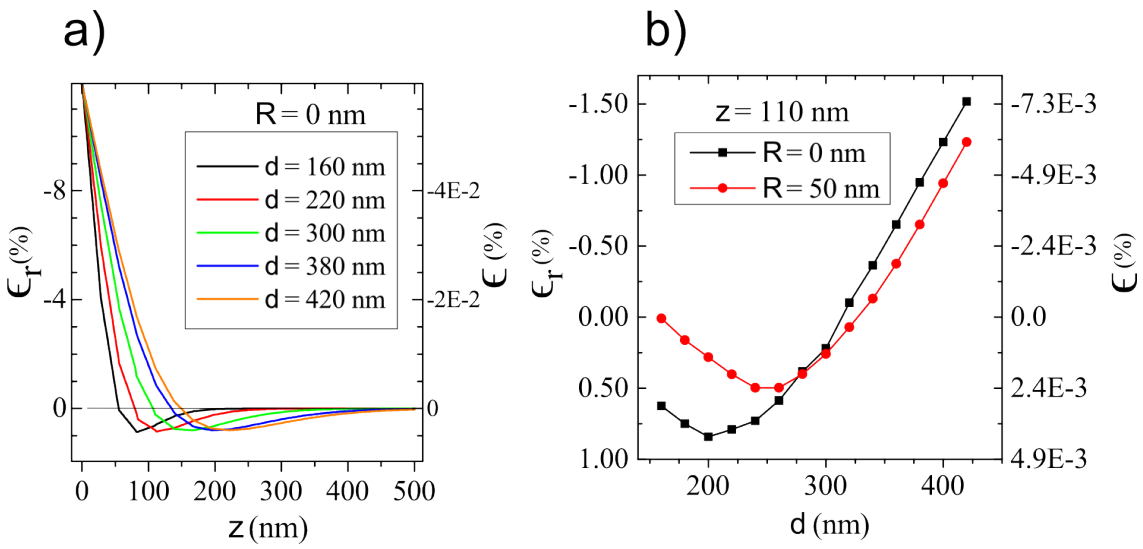

Fig. 4.9 a) Plot of the strain ε and relative strain ε_r as a function of the distance along the z axis from the Au/GaAs interface (z = 0 nm at radially centered position, R = 0 nm). b) Plot of ε and ε_r at z = 110 nm and R = 0 nm, 50 nm. The nanowire diameter is d = 220 nm in a), and ε_0 = -0.1% in a)-c).

as described in chapter 1. Using this method the QD is elastically strain tunable. The advantage of this material is that higher voltages can be applied and therefore more strain is created. The amount of strain transferred from the PMN-PT to the QD's relaxes across the GaAs structure. The strain relaxation across the nanowire was modeled using the finite element method (FEM) with the help of Dr. T.Dada and Mr G.C. Ballesteros. Comsol, a comercial software was used to quantitatively calculate the strain transfer across the 200 nm Au bonding layer and the remaining strain reaching the QD after a distance z (Fig.4.8). The strain-field relaxation was quantified by means of the relative strain (ε_r) defined as $\varepsilon_r = \varepsilon(x,y,z)/|\varepsilon_0|$, where $\varepsilon(x,y,z)$ is the strain at a given position with coordinates (x,y,z), and ε_0 is the strain in the PMN-PT crystal. Fig.4.8) shows the profile of relative strain ε_r with $\varepsilon_0 = -0.1\%$ and d = 220 nm. The color legend is scaled to highlight the strain-field relaxation within the nanowire. In Fig.4.9 a) shows the plot of ε_r (and ε) at the center of the nanowire R = 0 nm, as a function of axial position along the nanowire for different diameters d. Fig.4.9 b) shows the strain as a function of d for radial positions R = 0 nm and 50 nm for D = 110 nm.

The modeling confirmed that the strain relaxation is linear with respect to the applied strain, i.e. $\varepsilon_r \propto \varepsilon_0$, for $\varepsilon_0 = -0.05\%,...,-0.5\%$ (which is within the range expected for a single PMN-PT single crystal for an applied voltage of 0-1kV [122, 130]). The model shows that the strain field generated by the piezoelectric crystal relaxes substantially ($\approx$ 80%) across the 200 nm-thick Au layer. The remaining strain field transmitted across the Au/GaAs interface is highly dependent on the diameter of the nanowire as well as on the radial axial position within the nanowire. In particular, it was observed that relaxation increased with reduced nanowire diameter, Fig.4.9 a), as well as higher strain fields nearer the center of the nanowire, Fig.4.9 c). Although the applied strain is compressive, regions

of tensile strain are seen as the strain relaxes along the nanowire.

The axial position for optimal strain tuning is found to be in conflict with that required for optimal coupling to the HE_{11} mode. In fact, with geometry optimized for coupling at $\lambda = 950nm$ (i.e.,D = 80 nm, d = 220 nm, R = 0 nm), we obtain $\varepsilon_r = 0.04\%$. While changing to $D < 80$ nm significantly increases ε_r, it will likely lead to increased spectral fluctuations due to the effect of surface states at the mirror/nanowire interface [131, 132]. Keeping d = 220 nm and R = 0 nm for $D > 80$ nm, ε_r is maximized at $D \approx 110$ nm before completely relaxing by D = 250 nm. For a QD at R = 0 nm and D = 110 nm in a pillar with diameter d = 220 nm, the model predicts a relative strain of $\varepsilon_r = 0.8\%$, while η is only moderately affected (see Fig.4.4), demonstrating the validity of the device as an effcient and elastically tunable platform for quantum photonics.

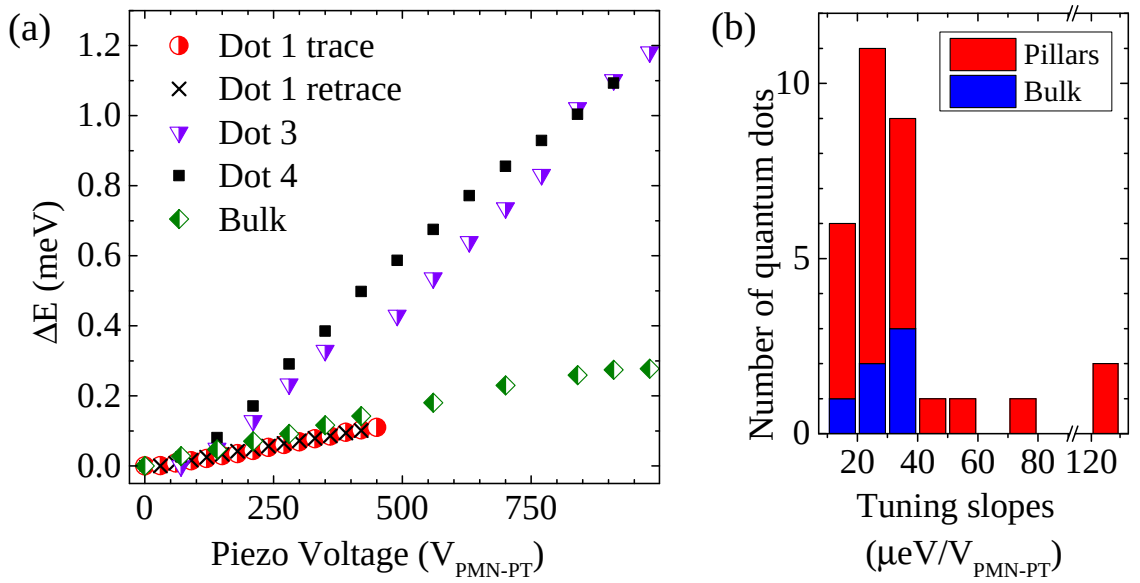

Fig. 4.10 a) Strain tuning the energies of different single QD excitons. Each QD in each pillar exhibits a different strain tuning slope (S=$\Delta E/\Delta V_{PMN-PT}$), as shown in the histogram in b). Also shown in the histogram are tuning slopes S_b for QDs in the μ-structure membrane (S_μ = 0.29 $\pm$ 0.06 μeV/VPMN-PT).

The above described elastic tuneability of the exciton states was demonstrated. Fig.4.10 a) shows several examples of exciton detuning for QDs in different nanowire antennas as a function of applied bias to the piezoelectric crystal (V_{PMN-PT}). Varied strain tuning slopes for each QD were observed in each nanowire, as summarized for 30 QDs in the histogram in Fig.4.10 b). Also shown in the histogram of the strain tuning are QDs located in the roughly 4 μm x 5 μm unetched region of the sample nearby the nanowires (micro-structure), partly visible in Fig.4.7 a) on top and bottom edges of the array.

In general, the strain tuning is achieved with small amounts of hysteresis, as shown for Dot 1. A maximum amplitude of $\delta E \approx 1.2$ meV was achieved in the experiment. The large standard deviation in tuning is expected for two reasons: (i) the amplitude and even sign of the strain field is highly dependent on the radial position of the QD in the nanowire (as shown in Fig.4.9); and (ii) strain tuning of the quantum states is highly dependent on

the exact morphology of the dot, which is unique for every QD [20, 31, 133]. In spite of the significant strain field relaxation in the Au contact and the nanowire, we achieve substantial *insitu* strain tuning of the QD excitonic transition energies.

Further improvement in the tuning range can be obtained by reducing the Au layer thickness H. In addition it would be possible to move the QD closer to the mirror, which may however lead to more spectral fluctuations. Increasing the wire diameter and using QD that emit at a longer wavelength would reduce the strain relaxation as well.

4.2 Conclusion

The optical spectroscopy of the 48 brightest nanowires with different diameters and taper angles showed a correlation between a reduced taper angle and increased extraction efficiency. The extraction efficiency also increased for a reduced normalized nanowire diameter d/λ.

The linewidth broadening Γ and Stark shift ΔE was measured as a function of excitation power. The Stark shift was associated with the increase of charges on the nanowire surface. The linewidth broadening was associated with the fluctuation of charges at the nanowire surface.

Lifetime measurements of the X^0 and X^{-1} emission line showed lifetimes of 1.0 ns and 0.96 ns respectively. The lifetimes are 10% to 20% longer then expected for such dots but in agreement with the slight inhibition of spontaneous emission predicted by P_m in Fig.4.4. The extraction efficiency of the brightest nanowire was determined to be η_{max} = 57%, and the average extraction efficiency of $\bar{\eta} = 13\% \pm 10\%$.

Simulation of strain relaxation predicted that a relative strain of ε = 0.8% is experienced at the QD location, and that 80 % of the strain created by the PMN-PT relax across the Au bonding layer. Nevertheless a maximum energy shift of ΔE = 1.2 meV was achieved. It is proposed that by using a negative voltage -0.4 kV an additional 40 % tensile strain can be achieved. Furthermore reducing the Au layer will likely favor the strain tunability as well.

Chapter 5

Conclusion

5.1 Conclusion

An elastically-tunable QD embedded in a nanowire waveguide emitting single photons with resolution limited linewidths was demonstrated. The device enables strain tuning which could enable resonant fluorescence experiments, reduction of fine structure splitting for entangled photon-pair generation, and two photon interference from separate QDs in nanowire antennas.

Nanofabrication techniques have been adopted to fabricate a strain-tunable nanowire antenna with an embedded InAs/GaAs semicondcutor quantum dot. The key fabrication techniques used were e-beam lithography, thermo-compression bonding, lift-off and reactive ion etching. Nanwoires with diameters between d = 120 nm and 500 nm have been fabricated and aspect ratios of up to 1:18 have been achieved. Taper angles as low as α = 1° have been achieved and angles as low as α = 10° have been fabricated frequently. The Ni mask used for dry etching reduced the fabrication complexity, but the nanowire surface roughness was increased. The achieved nanowire geometry is closer to theoretically proposed geometry by Friedler *et al.* [62] which had a straight bottom compared to work by J.Claudon *et al.* [76] whose nanowire has an inverted taper.

For optical characterization an experimental set-up has been constructed that combines confocal microscopy with low temperature pulsed tube cryostats to carry out experiments at 4K. Two commercial pulsed tube cryostats and a homebuild system were assembled. The microscope was succefully modified to allow white light imaging of the sample surface with a magnification and resolution good enough to distinguish, and deterministically select, individual nanowires with diameter $d < 200$ nm and height $h = 2$ μm. A low temperature miniature confocal microscope for 950 nm, suitable for the home built cryostat was build and characterized. A procedure to find the focal plane by measuring the transmission was adopted.

The properties of the embedded QD have been investigated using non resonant PL spectrocopy and TCSPS. The shape of the nanowire determined by SEM was correlated to the peak emission intensity of the brightest QDs inside individual nanowires. Two

trends predicted by computer models were observed. (i) It was shown that the emission intensity increased with a reduced top taper angle. (ii) A reduced normalized wire diameter also increased the emission intensity. The fitting of the stark shift model to the QD emission line emphasized the importance of the QD's environment. In addition to the free charges at the nanowire surface, increasing excitation power leads to an increase in carriers in the wetting layer and therefore fluctuations of the QD electrostatic environment and dephasing [57]. The linewidth broadening and the energy detuning observed at increasing excitation power due to surface charges on the nanowire are yet to be overcome to improve device performance. At low excitation powers QDs with resolution limited linewidth have been measured. Stark shifts with more then 80 μeV have been measured.

The lifetime of the exciton states was found to be $\tau \approx 1$ ns. The extraction efficiency of the nanowire was estimated using the lifetime of the embedded QD at saturation and was found to be 57% for the brightest nanowire, which is an improvement factor of x 63 compared to a QD in bulk. FDTD simulation of a similar nanowire geometry resulted in a similar maximum η, signifying that the brightest nanowire measured likely had a QD at the center of the nanowire.

Single-photon emission of the device was confirmed by measuring the second order correlation function and was found to be $g^{(2)} \approx 0$ after deconvolution at low excitation rates.

By bonding the nanowires to a PMN-PT, the peak emission wavelength of the QDs was elastically tuned by up to 1.2 meV using compressive strain. FEM was used to simulate the strain relaxation originating in the PMN-PT across the Au bonding layer to the GaAs nanowire structure, more precisely the strain at the QD location inside the nanowire. For the ideal nanowire diameter, d = 220 nm, the maximum transferred strain was created at the QD location 110 nm from the Au mirror. With increasing wire diameter the location of maximum strain shifted further away from the Au mirror. It was shown that 80% of the strain field relaxes across the Au mirror. The energy detuning caused by strain is much larger then the energy detuning caused by the stark shift.

By reducing the dipole to mirror distance and using a DBR mirror instead of the Au mirror, in addition the taper angle it should be possible to exceed the extraction efficiency of all devices in table 1.1. The high extraction efficiency and count rate combined with a low $g^{(2)}$, indicate the capability of the device as a elastically strain tunable single photons source for metrology and QIP applications.

5.2 Outlook

A combination of strain- and electrostatic tuning of the emission wavelength is an advantage over high Q cavities that enables resonance fluorescence, and allows tuning the emission of two different QDs into resonance and create indistinguishable photons, or by canceling the FSS creating entangled photon pairs [134, 135]. A bright tunable light

source of indistinguishable photons at telecom wavelength is a sought after tool in quantum photonics and would allow for prospective experiments.

To further improve the performance of the nanowire, and its suitability as a wavelength tunable single photon source some changes could be made. To reduce the linewidth broadening caused by charges at the nanowire surface, it is proposed to anneal the nanowires so that impurities implanted during the dry etching process diffuse out.

A surface passivisation step might reduce the number of free electrons at the surface. The surface roughness could be reduced by improving the dry etch conditions and by using a different etch mask.

A planar Au mirror has a theoretical reflectivity r = 0.91. Reflectivity of a bare Au layer without the Si dioxide is only 0.6 for d/λ = 0.235 [76]. Alternatively using a DBR with 99% reflectivity could improve the wire performance, although it would compromise the ability to strain tune the QD. In addition using a DBR would simplify the fabrication process by making the flip-chip process redundant. For future work it is proposed to use QDs that emit at a longer wavelength for example 1300 nm or 1550 nm. This would make the device more suitable for long distance fiber communication.

In addition, the larger nanowire diameter would allow wider nanowires d = 305 - 364 nm which would have less strain relaxation and improve strain tuning. The strain tunability of nanowires has been shown and could be improved by reducing the Au bonding layer thickness between the GaAs nanowires and the PMN-PT. The full potential of the strain created by PMN-PT was not used, by applying a negative bias to the PMN-PT as low as - 400 V the tuning range of emission wavelength (ΔE = 1.2 meV) of the QD could have been increased by 40% using tensile strain.

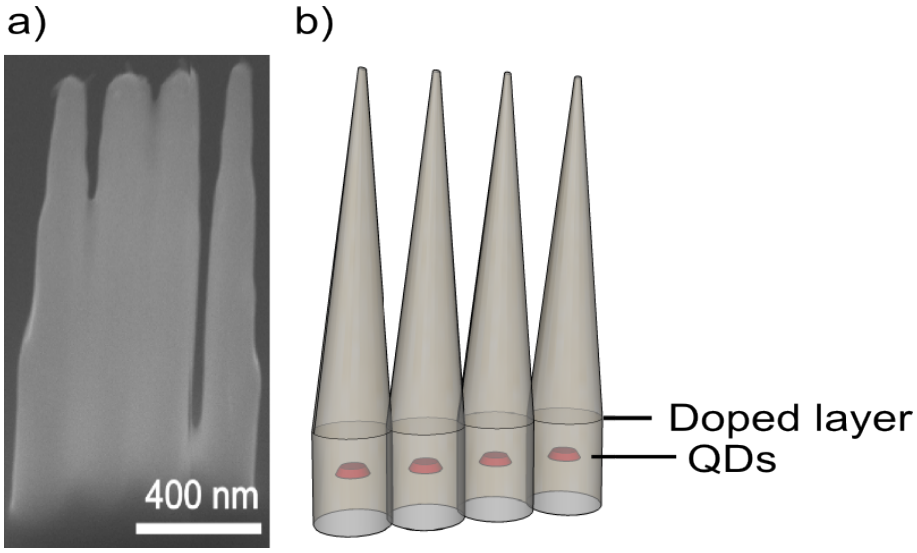

Fig. 5.1 SEM image of a) nanowires in close proximity. 3 of 4 wires have physical contact in between and would potentially allow electric current to flow through. The nanowires have a top taper angle of 5 . And should therefore have a higher extraction efficiency then the nanowires measured previously.b) Top view of sketch showing nanowires touching each other slightly to allow strain transfer and electric current to flow. c) side view of pillar array with doped layer.

To add another degree of freedom and allow to further change the emission wavelength of QDs it is proposed to make the nanowire charge tunable. It is believed that by placing the nanowires in close proximity (see Fig. 5.1 a), and by placing many wires in series as shown in [136], it would be possible to create an electric contact between them using a doped layer above the QD location (see Fig. 5.1 b). In addition, by placing the wires together one could increase their effective diameter, which in turn increases the strain that can be applied to the QDs. Arranging the nanowires in a pattern where they transfer strain to each other (hexagonal structure) could increase the strain tunability as well. Wires in close proximity have also shown lower top taper angles and should therefore have a higher extraction efficiency. It is believed that the lower taper angle is created by competition for chemical reactants during dry etching that reduces the undercut of the etchmask.

Implementing the suggested improvements in the existing device structure is a worthwhile challenge that should be taken up soon.

References

[1] E. Gibney. Physics: Quantum computer quest. Nature, 516:24–26, Dec 2014.

[2] R.P. Feynman. Simulating physics with computers. International Journal of Theoretical Physics, 21(6-7):467–488, 1982.

[3] P.W. Shor. Algorithms for quantum computation: discrete logarithms and factoring. In Foundations of Computer Science, 1994 Proceedings., 35th Annual Symposium on, pages 124–134, Nov 1994.

[4] L.K. Grover. A fast quantum mechanical algorithm for database search. In Proceedings of the Twenty-eighth Annual ACM Symposium on Theory of Computing, STOC '96, pages 212–219, New York, NY, USA, 1996. ACM.

[5] H.J Kimble. The quantum internet. Nature, 453(7198):1023–1030, 2008.

[6] N.S Sangouard, C. Simon, H. de Riedmatten, and N. Gisin. Quantum repeaters based on atomic ensembles and linear optics. Rev. Mod. Phys., 83:33–80, Mar 2011.

[7] C. Santori, D. Fattal, J. Vučković, G.S Solomon, and Y. Yamamoto. Indistinguishable photons from a single-photon device. Nature, 419(6907):594–597, 2002.

[8] S. Ates, S.M. Ulrich, S. Reitzenstein, A. Löffler, A. Forchel, and P. Michler. Post-selected indistinguishable photons from the resonance fluorescence of a single quantum dot in a microcavity. Physical Review Letters, 103(16):167402, 2009.

[9] Y. He, Y. He, Y. Wei, D. Wu, M. Atatüre, C. Schneider, S. Höfling, M. Kamp, C-Y. Lu, and J-W. Pan. On-demand semiconductor single-photon source with near-unity indistinguishability. Nature Nanotechnology, 8(3):213–217, 2013.

[10] R. B. Patel, Anthony J. Bennett, I. Farrer, C. A. Nicoll, D. A. Ritchie, and A. J. Shields. Two-photon interference of the emission from electrically tunable remote quantum dots. Nature Photonics, 4(9):632–635, July 2010.

[11] E.B. Flagg, A. Muller, S.V. Polyakov, A.x Ling, A. Migdall, and G.S. Solomon. Interference of single photons from two separate semiconductor quantum dots. Phys. Rev. Lett., 104:137401, 2010.

[12] A. Tartakovskii. Quantum Dots Optics, Electron Transport and Future Applications. 2012.

[13] S. Kumar. Tuning of single semiconductor quantum dots and their host structures via strain and in situ laser processing. TU-Chemnitz, 2013.

[14] G.H. Wannier. The structure of electronic excitation levels in insulating crystals. Phys. Rev., 52:191–197, Aug 1937.

[15] M. Bayer, O. Stern, P. Hawrylak, S. Fafard, and A. Forchel. Hidden symmetries in the energy levels of excitonic artificial atoms. Nature, 405(6789):923–926, 2000. 10.1038/35016020.

[16] R. J. Warburton, C.S. Durr, K. Karrai, J. P. Kotthaus, G. Medeiros-Ribeiro, and P.M. Petroff. Charged excitons in self-assembled semiconductor quantum dots. Phys. Rev. Lett., 79:5282–5285, Dec 1997.

[17] D.J. Griffiths. Introduction to Quantum Mechanics. Pearson Prentice Hall, 2005.

[18] M. Bayer, A. Kuther, A. Forchel, A. Gorbunov, V. B. Timofeev, F. Schäfer, J. P. Reithmaier, T. L. Reinecke, and S. N. Walck. Electron and hole *g* factors and exchange interaction from studies of the exciton fine structure in $in_{0.60}ga_{0.40}as$ quantum dots. Phys. Rev. Lett., 82:1748–1751, Feb 1999.

[19] A.J. Bennett, M.A. Pooley, R.M. Stevenson, M.B. Ward, R.B. Patel, A.B. de La Giroday, N. Sköld, I. Farrer, C.A. Nicoll, D.A. Ritchie, et al. Electric-field-induced coherent coupling of the exciton states in a single quantum dot. Nature Physics, 6(12):947–950, 2010.

[20] L. Sapienza, R. Malein, C. Kuklewicz, P. Kremer, K. Srinivasan, A. Griffiths, E. Clarke, M. Gong, R.J. Warburton, and B.D. Gerardot. Exciton fine-structure splitting of telecom-wavelength single quantum dots: Statistics and external strain tuning. Physical Review B, 88(15):155330, 2013.

[21] R. M. Stevenson, R. J. Young, P. Atkinson, K. Cooper, D. A. Ritchie, and A. J. Shields. A semiconductor source of triggered entangled photon pairs. Nature, 439(7073):179–182, 2006.

[22] R. Hafenbrak, S.M. Ulrich, P. Michler, L. Wang, A. Rastelli, and O.G. Schmidt. Triggered polarization-entangled photon pairs from a single quantum dot up to 30k. New Journal of Physics, 9(9):315, 2007.

[23] D. Bimberg, M. Grundmann, and N.N. Ledentsov. Quantum dot heterostructures. Willey, 1998.

[24] R. J. Warburton. Self-assembled semiconductor quantum dots. Contemporary Physics, 43(5):351–364, 2002.

[25] D. Leonard, K. Pond, and P. M. Petroff. Critical layer thickness for self-assembled inas islands on gaas. Phys. Rev. B, 50:11687–11692, Oct 1994.

[26] PhD P.A. Dalgarno. Time correlated single photon counting on charge tunable semiconductor quantum dots. Heriot Watt University, 2005.

[27] J. M. Garcıa, T. Mankad, P. O. Holtz, P. J. Wellman, and P. M. Petroff. Electronic states tuning of inas self-assembled quantum dots. Applied Physics Letters, 72(24), 1998.

[28] H. Pettersson, R. Warburton, and A. Lorke. Excitons in self-assembled quantum ring-like structures. Physica E, 6(1-4):510–513, 2000.

[29] R. Trotta, E. Zallo, C. Ortix, P. Atkinson, J. D. Plumhof, J. van den Brink, A. Rastelli, and O. G. Schmidt. Universal recovery of the energy-level degeneracy of bright excitons in ingaas quantum dots without a structure symmetry. Phys. Rev. Lett., 109:147401, Oct 2012.

[30] S. Seidl, M. Kroner, A. Högele, K. Karrai, R.J. Warburton, A. Badolato, and P.M. Petroff. Effect of uniaxial stress on excitons in a self-assembled quantum dot. Applied physics letters, 88(20):203113, 2006.

[31] C.E. Kuklewicz, R.N.E. Malein, P.M. Petroff, and B.D. Gerardot. Electro-elastic tuning of single particles in individual self-assembled quantum dots. Nano Letters, 12(7):3761–3765, 2012.

[32] D.J.P. Ellis, R.M. Stevenson, R.J. Young, A.J. Shields, P. Atkinson, and D.A. Ritchie. Control of fine-structure splitting of individual InAs quantum dots by rapid thermal annealing. Aplied Physics Letters, 90(1), Jan 2007.

[33] M. Bayer, A. Kuther, A. Forchel, A. Gorbunov, V. B. Timofeev, F. Schäfer, J. P. Reithmaier, T. L. Reinecke, and S. N. Walck. Electron and hole g factors and exchange interaction from studies of the exciton fine structure in $in_{0.60}ga_{0.40}As$ quantum dots. Phys. Rev. Lett., 82:1748–1751, Feb 1999.

[34] J.J. Finley, P.W. Fry, A.D. Ashmore, A. Lemaitre, A.I. Tartakovskii, R. Oulton, D.J. Mowbray, M.S. Skolnick, M. Hopkinson, P.D. Buckle, et al. Observation of multicharged excitons and biexcitons in a single ingaas quantum dot. Physical Review B, 63(16):161305, 2001.

[35] A. Högele, S. Seidl, M. Kroner, K. Karrai, R. Warburton, B.D. Gerardot, and P.M. Petroff. Voltage-controlled optics of a quantum dot. Physical review letters, 93(21):217401, 2004.

[36] B.D. Gerardot, S. Seidl, P.A. Dalgarno, R.J. Warburton, D. Granados, J.M. Garcia, K. Kowalik, O. Krebs, K. Karrai, A. Badolato, et al. Manipulating exciton fine structure in quantum dots with a lateral electric field. Applied physics letters, 90(4):041101, 2007.

[37] M.M. Vogel, S.M. Ulrich, R. Hafenbrak, .P Michler, L. Wang, A. Rastelli, and O.G. Schmidt. Influence of lateral electric fields on multiexcitonic transitions and fine structure of single quantum dots. Applied Physics Letters, 91(5):051904, 2007.

[38] J. P. Reithmaier, G. Sek, A. Loffler, C. Hofmann, S. Kuhn, S. Reitzenstein, L. V. Keldysh, V. D. Kulakovskii, T. L. Reinecke, and A. Forchel. Strong coupling in a single quantum dot-semiconductor microcavity system. Nature, 432(7014):197–200, 2004.

[39] B. Urbaszek, E. J. McGhee, M. Krüger, R. J. Warburton, K. Karrai, T. Amand, B. D. Gerardot, P. M. Petroff, and J. M. Garcia. Temperature-dependent linewidth of charged excitons in semiconductor quantum dots: Strongly broadened ground state transitions due to acoustic phonon scattering. Phys. Rev. B, 69:035304, Jan 2004.

[40] K. Kowalik, O. Krebs, A. Lemaître, S. Laurent, P. Senellart, P. Voisin, and J. A. Gaj. Influence of an in-plane electric field on exciton fine structure in inas-gaas self-assembled quantum dots. Applied Physics Letters, 86(4):–, 2005.

[41] S.L. Chuang. Physics of photonic devices, 2nd edition. 2009.

[42] Y. Sun, S. E. Thompson, and T. Nishida. Physics of strain effects in semiconductors and metal-oxide-semiconductor field-effect transistors. Journal of Applied Physics, 101(10):–, 2007.

[43] F. Ding, R. Singh, J. D. Plumhof, T. Zander, V. Křápek, Y. H. Chen, M. Benyoucef, V. Zwiller, K. Dörr, G. Bester, A. Rastelli, and O. G. Schmidt. Tuning the exciton binding energies in single self-assembled InGaAs/GaAs quantum dots by piezoelectric-induced biaxial stress. Phys. Rev. Lett., 104:067405, Feb 2010.

[44] S. Buckley, K. Rivoire, and J. Vučković. Engineered quantum dot single-photon sources. Reports on Progress in Physics, 75(12):126503, 2012.

[45] P. Michler, A. Kiraz, C. Becher, W. V. Schoenfeld, P. M. Petroff, Lidong Zhang, E. Hu, and A. Imamoglu. A quantum dot single-photon turnstile device. Science, 290(5500):2282–2285, 2000.

[46] S. Bounouar, M. Elouneg-Jamroz, M. den Hertog, C. Morchutt, E. Bellet-Amalric, R. André, C. Bougerol, Y. Genuist, J.-Ph. Poizat, S. Tatarenko, and K. Kheng. Ultrafast room temperature single-photon source from nanowire-quantum dots. Nano Letters, 12(6):2977–2981, 2012.

[47] A. Kiraz, M. Atatüre, and A. Imamoğlu. Quantum-dot single-photon sources: Prospects for applications in linear optics quantum-information processing. Phys. Rev. A, 69:032305, Mar 2004.

[48] M. Varnava, D.E. Browne, and T. Rudolph. How good must single photon sources and detectors be for efficient linear optical quantum computation? Phys. Rev. Lett., 100:060502, Feb 2008.

[49] B. Lounis and M. Orrit. Single-photon sources. Reports on Progress in Physics, 68(5):1129, 2005.

[50] V. Giovannetti, S. Lloyd, and L. Maccone. Quantum-enhanced positioning and clock synchronization. Nature, 412(6845):417–419, 2001.

[51] O. Solgaard. Photonic Microsystems. Springer US, 1 edition, 2009.

[52] C. Sylvain, R. Alfredo, T. Quynh, and B. Henri. Gaas photonic crystal nanocavity with ultrahigh-q : toward microwatt nonlinearity at 1550 nm. arXiv preprint arXiv:0804.0378, 2008.

[53] S. Reitzenstein and A. Forchel. Quantum dot micropillars. Journal of Physics D: Applied Physics, 43(3):033001, 2010.

[54] L.C. Andreani, G. Panzarini, and J.M. Gerard. Strong-coupling regime for quantum boxes in pillar microcavities: Theory. Phys. Rev. B, 60:13276–13279, Nov 1999.

[55] G. Khitrova, H. M. Gibbs, M. Kira, S. W. Koch, and A. Scherer. Vacuum rabi splitting in semiconductors. Nat Phys, 2(2):81–90, 2006.

[56] J. M. Gérard, D. Barrier, J. Y. Marzin, R. Kuszelewicz, L. Manin, E. Costard, V. ThierryMieg, and T. Rivera. Quantum boxes as active probes for photonic microstructures: The pillar microcavity case. Applied Physics Letters, 69(4):449–451, 1996.

[57] O. Gazzano, S.M. de Vasconcellos, C. Arnold, A. Nowak, E. Galopin, I. Sagnes, L. Lanco, A. Lemaître, and P. Senellart. Bright solid-state sources of indistinguishable single photons. Nature Communications, 4:1425, 2013.

[58] J.M. Gerard and B. Gayral. Strong purcell effect for inas quantum boxes in three-dimensional solid-state microcavities. Lightwave Technology, Journal of, 17(11):2089–2095, Nov 1999.

[59] S. Strauf, N.G. Stoltz, M.T. Rakher, L.A. Coldren, P.M. Petroff, and D. Bouwmeester. High-frequency single-photon source with polarization control. Nature Photonics, 1(12):704–708, 2007.

[60] E. Moreau, I. Robert, J. M. Gérard, I. Abram, L. Manin, and V. Thierry-Mieg. Single-mode solid-state single photon source based on isolated quantum dots in pillar microcavities. Applied Physics Letters, 79(18), 2001.

[61] Y.R. Nowicki-Bringuier, J. Claudon, C. Böckler, S. Reitzenstein, M. Kamp, A. Morand, A. Forchel, and J.M. Gerard. High q whispering gallery modes in gaas/alas pillar microcavities. Opt. Express, 15(25):17291–17304, Dec 2007.

[62] I. Friedler, C. Sauvan, J.P. Hugonin, P. Lalanne, J. Claudon, and J.M. Gérard. Solid-state single photon sources: the nanowire antenna. Optics express, 17(4):2095–2110, 2009.

[63] T. Rivera, J.-P. Debray, J. M. Gérard, B. Legrand, L. Manin-Ferlazzo, and J. L. Oudar. Optical losses in plasma-etched algaas microresonators using reflection spectroscopy. Applied Physics Letters, 74(7), 1999.

[64] M. Lermer, N. Gregersen, F. Dunzer, S. Reitzenstein, S. Höfling, J. Mørk, L. Worschech, M. Kamp, and A. Forchel. Bloch-wave engineering of quantum dot micropillars for cavity quantum electrodynamics experiments. Phys. Rev. Lett., 108:057402, Jan 2012.

[65] A. Dousse, L. Lanco, J. Suffczyński, E. Semenova, A. Miard, A. Lemaˆ, I. Sagnes, C. Roblin, J. Bloch, and P. Senellart. Controlled light-matter coupling for a single quantum dot embedded in a pillar microcavity using far-field optical lithography. Phys. Rev. Lett., 101:267404, Dec 2008.

[66] T. Farrow, P. See, A.J. Bennett, M.B. Ward, P. Atkinson, K. Cooper, D.J.P. Ellis, D.C. Unitt, D.A. Ritchie, and A.J. Shields. Single-photon emitting diode based on a quantum dot in a micro-pillar. Nanotechnology, 19(34):345401, 2008.

[67] C. Böckler, S. Reitzenstein, C. Kistner, R. Debusmann, A. Löffler, T. Kida, S. Höfling, A. Forchel, L. Grenouillet, J. Claudon, and J. M. Gérard. Electrically driven high-q quantum dot-micropillar cavities. Applied Physics Letters, 92(9):–, 2008.

[68] T. Yoshie, A. Scherer, J. Hendrickson, G. Khitrova, H. M. Gibbs, G. Rupper, C. Ell, O. B. Shchekin, and D. G. Deppe. Vacuum rabi splitting with a single quantum dot in a photonic crystal nanocavity. Nature, 432(7014):200–203, 2004.

[69] K. Hennessy, A. Badolato, M. Winger, D. Gerace, M. Atature, S. Gulde, S. Falt, E. L. Hu, and A. Imamoglu. Quantum nature of a strongly coupled single quantum dot-cavity system. Nature, 445(7130):896–899, 2007.

[70] S. Noda. Recent progresses and future prospects of two- and three-dimensional photonic crystals. J. Lightwave Technol., 24(12):4554–4567, Dec 2006.

[71] A. Imamoglu, H. Schmidt, G. Woods, and M. Deutsch. Strongly interacting photons in a nonlinear cavity. Phys. Rev. Lett., 79:1467–1470, Aug 1997.

[72] L. Sanchis, M. J. Cryan, J. Pozo, I. J. Craddock, and J. G. Rarity. Ultrahigh purcell factor in photonic crystal slab microcavities. Phys. Rev. B, 76:045118, Jul 2007.

[73] Y. Akahane, T. Asano, B.S. Song, and S. Noda. High-q photonic nanocavity in a two-dimensional photonic crystal. Nature, 425(6961):944–947, 2003.

[74] K.H. Madsen, S. Ates, J. Liu, A. Javadi, S.M. Albrecht, I. Yeo, S. Stobbe, and P. Lodahl. Efficient out-coupling of high-purity single photons from a coherent quantum dot in a photonic-crystal cavity. arXiv preprint arXiv:1402.6967, 2014.

[75] Q.N. Wang, S. Stobbe, and P. Lodahl. Mapping the local density of optical states of a photonic crystal with single quantum dots. Phys. Rev. Lett., 107:167404, Oct 2011.

[76] J. Claudon, J. Bleuse, N.S. Malik, M. Bazin, P. Jaffrennou, N. Gregersen, C. Sauvan, P. Lalanne, and J.M. Gérard. A highly efficient single-photon source based on a quantum dot in a photonic nanowire. Nature Photonics, 4(3):174–177, 2010.

[77] Y. Ma, P.E. Kremer, and B.D. Gerardot. Efficient photon extraction from a quantum dot in a broad-band planar cavity antenna. Journal of Applied Physics, 115(2):023106, 2014.

[78] K. G. Lee, X. W. Chen, H. Eghlidi, P. Kukura, R. Lettow, A. Renn, V. Sandoghdar, and S. Götzinger. A planar dielectric antenna for directional single-photon emission and near-unity collection efficiency. Nature Photonics, 5:166–169, 2011.

[79] M. Davano, M.T. Rakher, D. Schuh, A. Badolato, and K. Srinivasan. A circular dielectric grating for vertical extraction of single quantum dot emission. Applied Physics Letters, 99(4):041102, 2011.

[80] N. Gregersen, T.R. Nielsen, J. Claudon, J.M. Gérard, and J. Mørk. Controlling the emission profile of a nanowire with a conical taper. Optics Letters, 33(15):1693–1695, 2008.

[81] J. Claudon, N. Gregersen, P. Lalanne, and J.M. Gérard. Harnessing light with photonic nanowires: fundamentals and applications to quantum optics. ChemPhysChem, 14(11):2393–2402, 2013.

[82] N. Gregersen, T.R. Nielsen, J. Mørk, J. Claudon, and J.M. Gérard. Designs for high-efficiency electrically pumped photonic nanowire single-photon sources. Optics Express, 18(20):21204–21218, 2010.

[83] I. Friedler, P. Lalanne, J. P. Hugonin, J. Claudon, J. M. Gérard, A. Beveratos, and I. Robert-Philip. Efficient photonic mirrors for semiconductor nanowires. Opt. Lett., 33(22):2635–2637, Nov 2008.

[84] J. Bleuse, J. Claudon, M. Creasey, N.S. Malik, J. Gérard, Ivan Maksymov, Jean-Paul Hugonin, and Philippe Lalanne. Inhibition, enhancement, and control of spontaneous emission in photonic nanowires. Phys. Rev. Lett., 106:103601, Mar 2011.

[85] G. Bulgarini, M.E. Reimer, T. Zehender, M. Hocevar, E.PAM Bakkers, L.P. Kouwenhoven, and V. Zwiller. Spontaneous emission control of single quantum dots in bottom-up nanowire waveguides. Applied Physics Letters, 100(12):121106, 2012.

[86] G. Bulgarini, M.E. Reimer, M. Bouwes Bavinck, K.D. Jöns, D. Dalacu, P.J. Poole, E.P.A.M. Bakkers, and V. Zwiller. Nanowire waveguides launching single photons in a gaussian mode for ideal fiber coupling. Nano Letters, 14(7):4102–4106, 2014. PMID: 24926884.

[87] Y.M. He, Y. He, Y.J. Wei, D. Wu, M. Atature, C. Schneider, S. Hofling, M. Kamp, C.. Lu, and J.W. Pan. On-demand semiconductor single-photon source with near-unity indistinguishability. Nat Nano, 8(3):213–217, 2013.

[88] O. Gazzano, M. P. Almeida, A. K. Nowak, S. L. Portalupi, A. Lemaître, I. Sagnes, A. G. White, and P. Senellart. Entangling quantum-logic gate operated with an ultrabright semiconductor single-photon source. Phys. Rev. Lett., 110:250501, Jun 2013.

[89] T. Santana. Unpublished values by ted santana in the quantum photonics group. 2015.

[90] R. Trotta, P. Atkinson, J.D. Plumhof, E. Zallo, R.O. Rezaev, S. Kumar, S. Baunack, J.R. Schroeter, and O.G. Rastelli, A .and Schmidt. Nanomembrane quantum-light-emitting diodes integrated onto piezoelectric actuators. Advanced Materials, 24(20):2668–2672, 2012.

[91] X. Suna, L. Hub, H. Songa, Z. Lia, D. Lia, H.g Jianga, and G. Miaoa. Selective wet etching of al0.7ga0.3as layer in concentrated hcl solution for peeling off gaas microtips. Solid-State Electronics, 53:1032–1035, Sep 2009.

[92] D.M. Tennant, A.R. Bleir, and G. Wiederrecht. Electron Beam Lithography of Nanostructures. Handbook of nanofabrication. Elsevier, 2010.

[93] A. Baca and C.I.H. Ashby. Fabrication of GaAs Devices. MPG Books Ltd, 2005.

[94] J. Hutchings. private communication (Oxford Instruments), 2011.

[95] N.S Malik and PhD Thesis. Les fils photoniques : une géométrie innovante pour la réalisation de sources de lumière quantique brillantes. L'UNIVERSITÉ DE GRENOBLE, 2006.

[96] T. Corle and G. Kino. Confocal Scanning Optical microscopy and Related Systems. Academic Press, 1996.

[97] A. Högele, S. Seidl, M. Kroner, K. Karrai, C. Schulhauser, O.r Sqalli, J. Scrimgeour, and R.J. Warburton. Fiber-based confocal microscope for cryogenic spectroscopy. Review of Scientific Instruments, 79(2):–, 2008.

[98] B.D. Gerardot. Lecture notes,SUPA course : (Experimental Nanophysics), 2010.

[99] R.H. Hadfield. Single-photon detectors for optical quantum information applications. Nat Photon, 3(12):696–705, 2009.

[100] S. Kimura and T. Wilson. Confocal scanning optical microscope using single-mode fiber for signal detection. Appl. Opt., 30(16):2143–2150, Jun 1991.

[101] T. Wilson. Confocal Microscopy. Academic Press, London, 1990.

[102] R. Radebaugh. Pulse tube cryocoolers for cooling infrared sensors. Proceedings of SPIE,Infrared Technology and Applications XXVI, 4130:363–379, 2000.

[103] A.T.A.M. de Waele. Basic operation of cryocoolers and related thermal machines. Journal of Low Temperature Physics, 164(5-6):179–236, 2011.

[104] attocube. attoDRY1000 (V.0.8 User Manual Toploading Pulse Tube System), 2013.

[105] S. Raymond, S. Fafard, P. J. Poole, A. Wojs, P. Hawrylak, S. Charbonneau, D. Leonard, R. Leon, P. M. Petroff, and J. L. Merz. State filling and time-resolved photoluminescence of excited states in $in_xga_{1-x}as$/gaas self-assembled quantum dots. Phys. Rev. B, 54:11548–11554, Oct 1996.

[106] PhD A. Kiraz. Nonclassical light emission from single self-assembled inas quantum dots. University of California, Santa Barbara, 2012.

[107] H. Lipsanen, M. Sopanen, and J. Ahopelto. Luminescence from excited states in strain-induced $in_xga_{1-x}as$ quantum dots. Phys. Rev. B, 51:13868–13871, May 1995.

[108] S. Raymond, S. Fafard, P. J. Poole, A. Wojs, P. Hawrylak, S. Charbonneau, D. Leonard, R. Leon, P. M. Petroff, and J. L. Merz. State filling and time-resolved photoluminescence of excited states in $in_xga_{1-x}as$/gaas self-assembled quantum dots. Phys. Rev. B, 54:11548–11554, Oct 1996.

[109] T. Chakraborty, F. Peeters, and U. Sivan. Nano-Physics Bio-Electronics: A New Odyssey: A New Odyssey. Elsevier, 2002.

[110] D. Brunner. Laser spectroscopy of single quantum dots. Heriot-Watt University , Edinburgh, 2006.

[111] Picoquant. PicoHarp 300 (User's Manual and Technical Data), 2014.

[112] S. Kimura, S. Kumano, M. Endo, I Suemune, T. Yokoi, H. Sasakura, S. Adachi, S. Muto, H. Song, S. Hirose, and T. Usuki. Photon antibunching observed from an inalas single quantum dot. Japanese Journal of Applied Physics, 44(6L):L793, 2005.

[113] P. Michler, A. Imamoglu, M. D. Mason, P. J. Carson, G. F. Strouse, and S. K. Buratto. Quantum correlation among photons from a single quantum dot at room temperature. Nature, 406(6799):968–970, 2000.

[114] X. Liu, H. Kumano, H. Nakajima, S. Odashima, T. Asano, T. Kuroda, and I. Suemune. Two-photon interference and coherent control of single inas quantum dot emissions in an ag-embedded structure. Journal of Applied Physics, 116(4):–, 2014.

[115] J. Curie and P. Curie. Développement par compression de l'électricitè polaire dans les cristaux hémièdres a faces inclinées'. Bull Soc Minér France, 3, page 90–93, 1880.

[116] J. Curie and P. Curie. Contractions et dilatations produites par des tensions électriques dans des cristaux hémièdres à faces inclinées'. CR Acad Sci Paris, 93, page 1137–1140, 1881.

[117] E. Sun and W. Cao. Relaxor-based ferroelectric single crystals: growth, domain engineering, characterization and applications. Progress in materials science, 65:124—210, August 2014.

[118] H. Fu and R.E. Cohen. Polarization rotation mechanism for ultrahigh electromechanical response in single-crystal piezoelectrics. Nature, 403(6767):281–283, 2000.

[119] Ltd APC International. Piezo theory new materials, 2014.

[120] L.E. Cross. Relaxor ferroelectrics. In Piezoelectricity, volume 114 of Springer Series in Materials Science, pages 131–155. Springer Berlin Heidelberg, 2008.

[121] S.E. Park and T.R. Shrout. Ultrahigh strain and piezoelectric behavior in relaxor based ferroelectric single crystals. Journal of Applied Physics, 82(4), 1997.

[122] A. Herklotz, J.D. Plumhof, A. Rastelli, O.G. Schmidt, L. Schultz, and K. Dörr. Electrical characterization of pmn–28thin-film substrates. Journal of Applied Physics, 108(9):–, 2010.

[123] A.B.M.A. Ibrahim, R. Murgan, R.M Kamil Abd, and J Osman.

[124] P.A. Dalgarno, J.M. Smith, J. McFarlane, B.D. Gerardot, K. Karrai, A. Badolato, P. M. Petroff, and R.J. Warburton. Coulomb interactions in single charged self-assembled quantum dots: Radiative lifetime and recombination energy. Phys. Rev. B, 77:245311, 2008.

[125] D. V. Regelman, U. Mizrahi, D. Gershoni, E. Ehrenfreund, W. V. Schoenfeld, and P. M. Petroff. Semiconductor quantum dot: A quantum light source of multicolor photons with tunable statistics. Phys. Rev. Lett., 87:257401, Nov 2001.

[126] M.A.M. Versteegh, M.E. Reimer, K.D. Jöns, D. Dalacu, P.J. Poole, A.o Gulinatti, A. Giudice, and V. Zwiller. Polarization-entangled photon pairs from a nanowire quantum dot. arXiv preprint arXiv:1405.4278, 2014.

[127] A. N. Vamivakas, Y. Zhao, S. Fält, A. Badolato, J. M. Taylor, and M. Atatüre. Nanoscale optical electrometer. Phys. Rev. Lett., 107:166802, Oct 2011.

[128] M. Bouwes Bavinck, M. Zieli?ski, B.J. Witek, T. Zehender, E.K.P. Bakkers, and V. Zwiller. Controlling a nanowire quantum dot band gap using a straining dielectric envelope. Nano letters, 12(12):6206–6211, 2012.

[129] B.D. Gerardot, S. Strauf, M.J.A. de Dood, A.M. Bychkov, A. Badolato, K. Hennessy, E.L. Hu, D. Bouwmeester, and P.M. Petroff. Photon statistics from coupled quantum dots. Phys. Rev. Lett., 95:137403, 2005.

[130] S. Kumar, R. Trotta, E. Zallo, J. D. Plumhof, P. Atkinson, A. Rastelli, and O. G. Schmidt. Strain-induced tuning of the emission wavelength of high quality gaas/algaas quantum dots in the spectral range of the 87rb d2 lines. Applied Physics Letters, 99(16):–, 2011.

[131] J. Houel, A. V. Kuhlmann, L. Greuter, F. Xue, M. Poggio, B. D. Gerardot, P. A. Dalgarno, A. Badolato, P. M. Petroff, A. Ludwig, D. Reuter, A. D. Wieck, and R. J. Warburton. Probing single-charge fluctuations at a GaAs/AlAs interface using laser spectroscopy on a nearby ingaas quantum dot. Phys. Rev. Lett., 108:107401, 2012.

[132] C.F. Wang, A. Badolato, I. Wilson-Rae, P.M. Petroff, E. Hu, J. Urayama, and A. Imamoğlu. Optical properties of single inas quantum dots in close proximity to surfaces. Applied physics letters, 85(16):3423–3425, 2004.

[133] K. D. Jöns, R. Hafenbrak, R. Singh, F. Ding, J. D. Plumhof, A. Rastelli, O. G. Schmidt, G. Bester, and P. Michler. Dependence of the redshifted and blueshifted photoluminescence spectra of single $in_xga_{1-x}As/GaAs$ quantum dots on the applied uniaxial stress. Phys. Rev. Lett., 107:217402, Nov 2011.

[134] M.A.M. Versteegh, M.E. Reimer, K.D. Jöns, D. Dalacu, P.J. Poole, A. Gulinatti, A. Giudice, and V. Zwiller. Observation of strongly entangled photon pairs from a nanowire quantum dot. Nat Commun, 5, 2014.

[135] T. Huber, A. Predojević, M. Khoshnegar, D. Dalacu, P.J. Poole, H. Majedi, and G. Weihs. Polarization entangled photons from quantum dots embedded in nanowires. Nano Letters, 14(12):7107–7114, 2014.

[136] A. Dousse, J. Suffczynski, A. Beveratos, O. Krebs, A.e Lemaitre, I. Sagnes, P. Bloch, J.and Voisin, and P. Senellart. Ultrabright source of entangled photon pairs. Nature, 466(7303):217–220, 2010.